Terms and Conditions of Use of Digitised Theses from Trinity College Library Dublin

Copyright statement

All material supplied by Trinity College Library is protected by copyright (under the Copyright and Related Rights Act, 2000 as amended) and other relevant Intellectual Property Rights. By accessing and using a Digitised Thesis from Trinity College Library you acknowledge that all Intellectual Property Rights in any Works supplied are the sole and exclusive property of the copyright and/or other IPR holder. Specific copyright holders may not be explicitly identified. Use of materials from other sources within a thesis should not be construed as a claim over them.

A non-exclusive, non-transferable licence is hereby granted to those using or reproducing, in whole or in part, the material for valid purposes, providing the copyright owners are acknowledged using the normal conventions. Where specific permission to use material is required, this is identified and such permission must be sought from the copyright holder or agency cited.

Liability statement

By using a Digitised Thesis, I accept that Trinity College Dublin bears no legal responsibility for the accuracy, legality or comprehensiveness of materials contained within the thesis, and that Trinity College Dublin accepts no liability for indirect, consequential, or incidental, damages or losses arising from use of the thesis for whatever reason. Information located in a thesis may be subject to specific use constraints, details of which may not be explicitly described. It is the responsibility of potential and actual users to be aware of such constraints and to abide by them. By making use of material from a digitised thesis, you accept these copyright and disclaimer provisions. Where it is brought to the attention of Trinity College Library that there may be a breach of copyright or other restraint, it is the policy to withdraw or take down access to a thesis while the issue is being resolved.

Access Agreement

By using a Digitised Thesis from Trinity College Library you are bound by the following Terms & Conditions. Please read them carefully.

I have read and I understand the following statement: All material supplied via a Digitised Thesis from Trinity College Library is protected by copyright and other intellectual property rights, and duplication or sale of all or part of any of a thesis is not permitted, except that material may be duplicated by you for your research use or for educational purposes in electronic or print form providing the copyright owners are acknowledged using the normal conventions. You must obtain permission for any other use. Electronic or print copies may not be offered, whether for sale or otherwise to anyone. This copy has been supplied on the understanding that it is copyright material and that no quotation from the thesis may be published without proper acknowledgement.

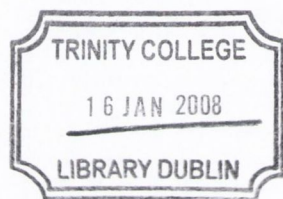# Dispersion and Characterisation of Carbon Nanotube & MoSI Nanowire Composites

By

Denis Mc Carthy

A thesis submitted for the degree of
Doctor of Philosophy
in the
University of Dublin

School of Physics
Trinity College Dublin

2007

Declaration

I declare that the work in this thesis has not been previously submitted as an exercise for a degree to this or any other university.

The work described herein is entirely my own, except for the assistance mentioned in the acknowledgements and the collaborative work mentioned in the list of publications.

I agree that Trinity College Library may lend or copy this thesis on request.

Denis Mc Carthy

March 2007

Summary

Recently, composites of polymers with various one-dimensional nanoparticles, mainly carbon nanotubes, have been investigated to develop robust electrically and thermally conductive materials or for mechanical reinforcement. One of the main obstacles preventing realisation of these goals are difficulties achieving good dispersion of the nanoparticles in the polymer matrix. In this thesis, novel composites prepared and their electrical and mechanical properties are characterised.

Carbon nanotube composites were prepared for this work with a novel polymer, First Contact, which was designed for cleaning high precision optics. Initial measurements found solutions of the polymer retained large amounts of nanotubes in stable dispersions for up to three days. Composites of the material were prepared by drop-casting and their conductivities were measured. Tensile testing was also performed to analyse the mechanical properties. The electrical properties of the composites were remarkable, with an extremely low percolation threshold of $(5.0 \pm 0.5) \times 10^{-6}$ and a maximum conductivity of ~ 1 S m^{-1} being measured. These excellent electrical properties were assigned to interactions between the polymer and the nanotubes causing an attractive force between nanotubes, resulting in an extremely low percolation threshold. The mechanical measurements showed a slight degradation in most properties, relative to the pure polymer, but overall the mechanical properties of the polymer were not significantly affected.

Carbon nanotubes have been studied for over a decade and still many of the problems preventing successful applications have not been overcome. Many alternative one-dimensional nanostructures have been developed for use in similar applications. Recently, the MoSI family of nanowires has been developed which have comparable physical properties to carbon nanotubes, but have some significant advantages, such as dispersability in common solvents, simple synthesis and uniform electronic structure. By monitoring the dispersion of the $Mo_6S_3I_6$ nanowires in a range of solvents and analysis of the results with sedimentation theory, N,N-dimethylformamide (DMF) was determined to be the best solvent for the material. This also allowed the first reported experimental calculation of the solid-fluid interaction parameter, β, to be close to 10^5 Pa.

As well as the nanowires that were stably dispersed in the DMF, two other distinct sedimenting phases were identified. Further analysis of these phases using UV-visible-near IR spectroscopy, x-ray photoelectron spectroscopy and scanning electron microscopy allowed them to be identified as an impurity phase and a phase of insoluble nanowires. Therefore, dispersion in DMF is a simple purification technique for the nanowire material,

as the dispersion can be decanted once all sedimentation is complete, separating the purified nanowires in the solute, from the impurities and insoluble nanowires in the sediment.

Using the results from the sedimentation study on the nanowires, composites were prepared of the MoSI nanowires. As the best solvent for the $Mo_6S_3I_6$ nanowires is DMF and one of the best solvents for the $Mo_6S_{4.5}I_{4.5}$ nanowires is chloroform, PMMA was chosen as the polymer for the composite work. An increase in conductivity of the $Mo_6S_3I_6$ composite relative to the pure PMMA was observed, but the $Mo_6S_{4.5}I_{4.5}$ nanowire composites had been shown to perform better electrically. Further work with the $Mo_6S_{4.5}I_{4.5}$ composites demonstrated the nanowires had no significant effect on the mechanical properties of the PMMA.

The full potential of nano-composites has been slow to be achieved. Alternative strategies and materials must be researched to develop applications and to further our understanding of these systems. This work can lead to the much sought after nano-materials which can are desired for many modern advancements.

"A theory is something nobody believes, except the person who made it. An experiment is something everybody believes, except the person who made it."

- Albert Einstein

"Reports that say that something hasn't happened are always interesting to me, because as we know, there are known knowns; there are things we know we know. We also know there are known unknowns; that is to say we know there are some things we do not know. But there are also unknown unknowns - the ones we don't know we don't know".

- Donald Rumsfeld

"I was thinking of you last night when I was getting into bed…."
- Jonathan N. Coleman, FTCD to me

Acknowledgements

There's a long list of people to thank, but it's sensible to start at the top with the boss. I'm very grateful to Johnny Coleman (FTCD) for hiring me and for the many years of supervision, support and bavaria. It has been a great experience and I hope he's enjoyed it as much as I did. Also to Werner, whose group I started as a part of, and always remained attached to. Thanks also to the PRTLI and the HFSP who provided the all important funding to do this research. Also, thanks to Dr. Robert Barklie for my initial years in research, when I worked in his EPR lab and was greatly assisted by him and his students.

Over the course of my four and a bit years, I've had the opportunity to work with several different people from outside the group. I'd like to thank Prof. Dragan Mihailovic and his group who synthesised the MoSI nanowire material used in my research. I'd also like to thank Prof. Jim Hamilton who provided the First Contact polymer and answered many questions for me. Also, thank you to Dr. Giuseppe Compagnini who did the XPS measurements.

To the members of both groups, Johnny and Werner's, who I worked with over the past few years – it was good knowing and working with ye all. From the various tenants of the tenement that is the pilgrimage office, to the delightful arches and to the various other obscure offices attached to the group, you've all been a great help in your own respective ways and I thank you very much. There are a lot of you though, so forgive me for any omissions. The students in order of seniority (as well as I can remember it), Anna, David (French/German), Eimhín Fiona, Helen, Martin, Shane, Sharon, David (Irish), Ian, Ronan, Yenny, Chris, Umar, Paula, Darren, Niall, Denise Evelyn and the postdocs, Valeria, Donal, Take, Javier, Zhenyu. Thanks to the MI people, Trevor, Jeannette and Chris. And also to the people who used to be here, Emer, Rob, Martin, Seán, Grace, Kev, Nacho, Sandy, Stef, Adam, Margaret & Patrick, Cathal, Manuel, Bernd, Stephen, Caitriona, Rebekah, James, ↻⚱△◢, and Les. Between assistance to my research, company on trips, reading my thesis drafts and eventual submission to requests to visit the pav and general willingness to listen to me, you have all helped. I hope you can each work out your relevant contributions.

Thanks to the technical and administrative staff of the School of Physics, TCD. Very nice and helpful people all of you.

Apparently, for his moral support, listening to me all these years, and helping me make important decisions, I have to thank Aaron. Also because he said "I want my paragraph, Waaaahhhh!"

And John Sheridan – you'll escape soon.

Finally, to the people who aren't paid to put up with me. I'd like to thank my parents who got me here and supported me over all the previous years. I hope you're glad and proud of the success you've helped me achieve. And to the rest of my family who are equally supportive – Patricia, Declan, Brendan and Cian.

Last but not least, except possibly in stature, I have to give thanks to Siobhán who has had the misfortune of putting up with me the most for the previous few months. You're very special to me and I'm looking forward to our postdoctoral life in Berlin.

Table of Contents

List of Figures

List of Tables

CHAPTER 1

Introduction

1.1 Background and Motivation

Polymers have become ubiquitous over the course of the last century, as their properties have been adapted for an increasingly broad range of applications. From bakelite in the 1900s, to nylon in the 1930s, to the high strength polymer Kevlar and conducting polymers in the 1970s (which won the Nobel prize for chemistry in 2000), polymers have continuously been invented or adapted to fill new and old needs.

A simple and effective method of improving polymer properties is the production of composites which combine the desirable properties of the polymer matrix used and the filler materials. Composites have existed since prehistory when wattle and daub was used to build the walls of houses and are mentioned in biblical times, with the production of bricks from wood and straw by the Israelites being described in Exodus. In the last few decades, the performance of composite materials has increased dramatically. Carbon fibre composites and glass composites (fibreglass) are used in applications from aerospace to sports equipment due to their high strength and low weights. Conductive composites are commonly used in antistatic bags for electronics and in car parts to improve paint adhesion.

With the discovery of carbon nanotubes in 1991, a new extremely strong and extremely conductive (both thermally and electrically) material became available with a range of potential applications. They have been suggested as fillers to improve the electrical and thermal conductivities of composites [1], and to improve the mechanical properties [2] also. The high aspect ratio of carbon nanotubes, and other nanowire materials, is predicted to give very low percolation thresholds. This, combined with the high electrical conductivity of the nanotubes themselves, suggests that highly conductive composites could be produced.

The elastomer, First Contact, used in the work with nanotubes here, has already been shown to have an affinity for carbonaceous materials, indicating its compatibility with carbon nanotubes. This should aid the dispersion of the nanotubes in the polymer matrix, which is a major problem currently for the production of nanotube composites. For high conductivities and the predicted low percolation thresholds to be achieved, it is necessary to have well dispersed nanotubes. The low percolation threshold is important, as

1

at high loading levels of nanotubes various difficulties can arise, such as processing becoming more difficult [3] and the formation of aggregates which weaken the composite material [4], amongst other problems. Carbon nanotubes and other nanoparticles also cost significantly more than polymers, making low filler concentrations desirable also from an economic point of view.

Despite much research into carbon nanotube composites, commonplace applications have yet to be produced. They are used in various niche areas, such as car parts to improve paint adhesion [5] and to reduce the weight of sports equipment, but carbon fibre and fibreglass composites are cheaper, and often more effective, making them the standard choice for most situations requiring strong, lightweight materials. The potential for nanotubes is great, but has yet to be achieved.

Many other one-dimensional nanostructures have been made since the discovery of carbon nanotubes, with a wide range of nanowires being grown using a variety of methods [6]. These materials can share many of the properties and advantages of carbon nanotubes as filler materials that have created so much interest and also have other desirable properties. Research into these materials as alternatives to nanotubes for electronics is quite advanced, whereas the research into their use in composites is quite limited, despite their equally high aspect ratios and comparable electrical conductivities. For instance, their appears to be only one paper published yet on nanowire reinforced composites [7], but there are sufficient papers on carbon nanotube reinforcement to warrant multiple review papers [2, 8].

In the work presented here, the dispersion of carbon nanotubes and MoSI nanowires is studied. The results from this work are then used to achieve composites with low percolation thresholds. This work with carbon nanotubes and with other nanowire materials is important for the nanotechnology field as a whole in order to realise suitable applications. Although the physical properties of carbon nanotubes have made them very attractive for research, it is important for the development of the whole nanotechnology field to pursue other possibilities. These may prove to make carbon nanotubes obsolete, or, alternatively, the research into these other materials may allow progress to be made towards achieving the full potential of nanotubes, thus making themselves obsolete.

1.2 Thesis Outline

In this thesis, the electrical and mechanical properties of composites of carbon nanotubes and MoSI nanowires are studied. The dispersion properties of the $Mo_6S_3I_6$ nanowires are also measured.

In Chapter 2, the properties of the nanotubes and nanowires are reviewed. Sedimentation theory is introduced and the relevant theory for the electrical and mechanical properties of composites is discussed.

In Chapter 3, the production methods for the two nanoparticles are described. The preparation procedures for the composites and the sedimentation studies are explained, and finally the various experimental techniques used are outlined.

Chapter 4 discusses the measured electrical and mechanical properties of the MWNT/First Contact composites. The results are compared with previous measurements.

Chapter 5 covers the sedimentation study of the $Mo_6S_3I_6$ nanowire material, the characterisation of the various phases present in the material and the development of a simple purification technique for the raw material.

In Chapter 6, the properties of MoSI nanowire composites are reported. These are compared with similar nanowire and nanotube composites.

The research presented in this thesis is then summarised in the concluding Chapter 7. Application of the composites characterised here are discussed, as well as further work which is required.

1.3 References

[1]   R. H. Baughman, A. A. Zakhidov, and W. A. de Heer, Science 297 (2002) 787.

[2]   J. N. Coleman, U. Khan, W. J. Blau, and Y. K. Gun'ko, Carbon 44 (2006) 1624.

[3]   P. Pötschke, A. R. Bhattacharyya, A. Janke, and H. Goering, Composite Interfaces 10 (2003) 389.

[4]   M. A. L. Manchado, L. Valentini, J. Biagiotti, and J. M. Kenny, Carbon 43 (2005) 1499.

[5]   B. Miller, Plastics World 54 (1996) 73.

[6]   M. Remskar, Advanced Materials 16 (2004) 1497.

[7]   S. R. C. Vivekchand, U. Ramamurty, and C. N. R. Rao, Nanotechnology 17 (2006) S344.

[8]   O. Breuer and U. Sundararaj, Polymer Composites 25 (2004) 630.

CHAPTER 2

Theory & Background

2.1 Introduction

Carbon nanotubes (CNTs) have been suggested for a wide range of applications due to their impressive physical properties, such as a high quantum electrical conductance [1], large thermal conductivity [2] and their impressive mechanical performance [3, 4]. Unfortunately, the difficulties involved with large-scale production, processing, and the range of electronic structures produced have been large obstacles to the realisation of major applications for CNTs. Particularly, the difficulties in dispersing CNTs is a significant problem for most applications, from composites to electronics, as single nanotubes are difficult to achieve and manipulate. Progress has been made towards dispersion of CNTs through various methods [5-7], but an alternative solution being investigated is the use of other one-dimensional inorganic materials [8, 9]. These new materials are advantageous as they have demonstrated similar physical properties to CNTs [10], but they also have other added benefits, such as uniform electronic structures [11], simple syntheses [8, 9, 12] and they can be stably dispersed [13, 14].

Both the CNTs and the more recent nanowire materials are being investigated as their properties indicate they are suitable for use in field emission devices [15, 16], nano-electronic devices [17-19] and in composites [20-23]. In this thesis, the dispersion carbon nanotubes and nanowires, and the preparation and characterisation of composites with them are discussed. For both electrically conductive and reinforced composites, it has been shown that high aspect fillers perform better [24, 25]. Therefore, these one-dimensional nanostructures are ideal for this purpose, due to their high electrical conductivities and excellent mechanical properties. As well as the carbon nanotubes, the inorganic nanowires used are the MoSI nanowires produced by the company Mo6 d.o.o. [10]. Both these materials are introduced in this chapter. Also, the theory used to study the dispersion properties of the nanotubes and nanowires, and to characterise the mechanical and electrical properties of the composites prepared are discussed.

2.2 Carbon Nanotubes

Single walled nanotubes (SWNTs) are hollow cylinders of graphene, capped at each end by half of a fullerene molecule, as shown in figure 2.1, with diameters of approximately 1 nm [26]. MWNTs consist of several coaxial SWNTs with a distance between layers of 0.345 nm, and have a range of diameters from 2 to 30 nm. Nanotubes form because the cylindrical structure is more energetically stable for smaller numbers of atoms as it leaves no dangling bonds at the edge of the graphene sheet. MWNTs were first discovered in 1991 in the soot from an electric arc discharge used to make C_{60}. SWNTs were subsequently observed in 1993, but they always require metal catalysts to be produced. SWNTs were an important discovery, as they are more fundamental than MWNTs, and have a well-understood molecular structure, allowing theoretical modelling of their properties, and prediction of new phenomena.
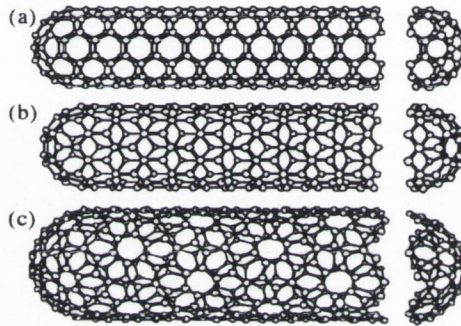
Figure 2.1- Three general structures of nanotubes; (a) armchair, (b) zigzag, (c) chiral [27].

2.2.1 Structure of Carbon Nanotubes

A carbon nanotube can be considered as a hexagonal network of carbon atoms (a honeycomb lattice) in the form of a cylinder. At each end there is a half-fullerene molecule, which contains 6 pentagons, allowing the curvature required to close the ends of the cylinder. The electronic properties of CNTs - whether they are semiconducting or metallic - depends on their structure. The nanotube unit cell, and hence its structure, is defined by the chiral vector, C_h, of the nanotube, which is given in equation 2.1 and shown in figure 2.2.

$$C_h = n\hat{a}_1 + m\hat{a}_2$$ Equation 2.1

where n and m are integers and $\hat{a}_1$ and $\hat{a}_2$ are the unit vectors of the two-dimensional hexagonal lattice. The chiral angle, θ, is the angle between the chiral vector C_h, and the unit vector $\hat{a}_1$.

6
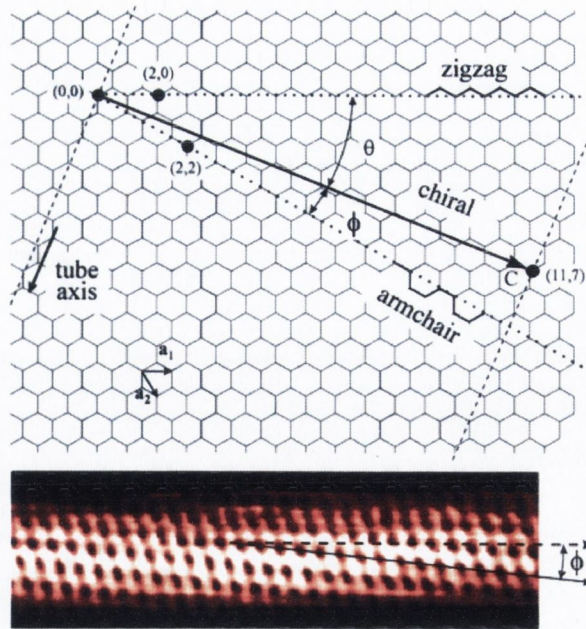
Figure 2.2– Illustration of the relationship of the chiral vector, C_h, to the nanotube structure diagrammatically (above) and on a TEM (below) [28].

The chiral vector forms the circular circumference of the nanotube and the different (n, m) values define different nanotube structures. Three distinct types of structures are possible - zigzag, armchair, and chiral, as shown in figure 2.1. Zigzag nanotubes occur where the chiral angle $\theta = 0$ (when n or m is zero) and armchair nanotubes occur when $\theta = 30°$ (when $n = m$), as illustrated in figure 2.3. Both these structures are achiral as they have mirror planes, but all other nanotubes (for $0° < \theta < 30°$) are chiral nanotubes.
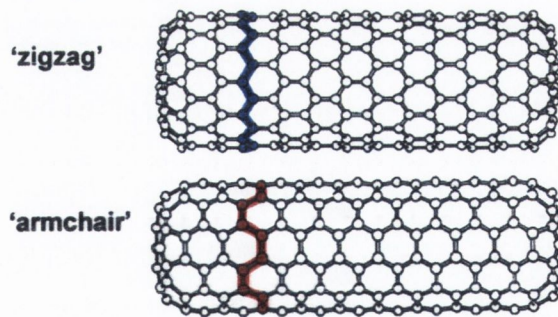
Figure 2.3 – Illustration of Armchair (n, n) and Zigzag $(n, 0)$ nanotubes, showing the reasons for their names [29].

The chirality of nanotubes, and hence electronic structure and other physical properties, is defined by the values of n and m. All nanotubes with $|n - m| = 3q$, where q is an integer, are metallic, and all others are semiconducting. Therefore, one third of all possible nanotubes are metallic. This includes all armchair $(n = m)$ and one third of zigzag $(n, 0)$ nanotubes. From the (n, m) values, the chiral angle, θ, and the diameter, d, of a nanotube can be calculated,

7

$$d = \sqrt{3} \Big/ \pi \; a_{c-c} \sqrt{n^2 + mn + m^2}$$

$$\theta = Tan^{-1} \frac{\sqrt{3}n}{2m+n}$$

where a_{c-c} is the carbon-carbon distance in a graphene sheet (1.42 Å [30]).

SWNTs tend to form large bundles of SWNTs, called ropes, as in figure 2.4, due to van der Waals' forces. These ropes can be 10 – 20 nm in diameter and up to 100 μm in length. The nanotubes in the ropes are aligned along a common axis, as observed by TEM and X-ray diffraction measurements [31]. From these measurements, it was determined that they form a triangular lattice structure, with a lattice constant of approximately 1.7 nm and an intertube distance of 0.34 nm. Unfortunately, it is very difficult to achieve individual SWNTs due to this tendency to form ropes, although it is possible at low concentrations in certain solvents [6]. MWNTs tend not to form similar bundles, due to their larger diameter and greater rigidity, but are still difficult to disperse in solvents alone.
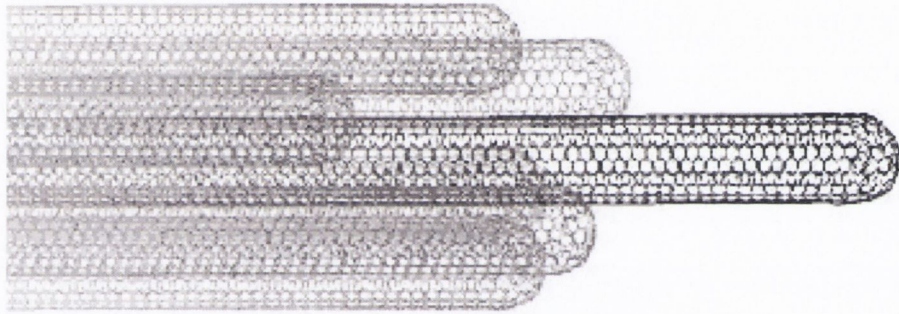
Figure 2.4– Diagrammatic representation of a "rope" of SWNTs [32].

2.2.2 Properties of Carbon Nanotubes

Graphene is a zero-bandgap semiconductor, which makes its electronic structure very sensitive to additional boundary conditions, such as those imposed by the nanotube structure. The rolling of the graphene into a SWNT creates a semiconductor or metallic electronic structure, depending on the diameter and helicity of the nanotube [33]. Due to the small diameter of nanotubes, a standing electron wave can only develop when the circumference is an integer multiple of the electron wavelength, as shown in figure 2.5. Therefore the electronic states are quantised in the circumferential direction, but not in the axial direction. This results in electrons only being able to propagate along the nanotube axis.
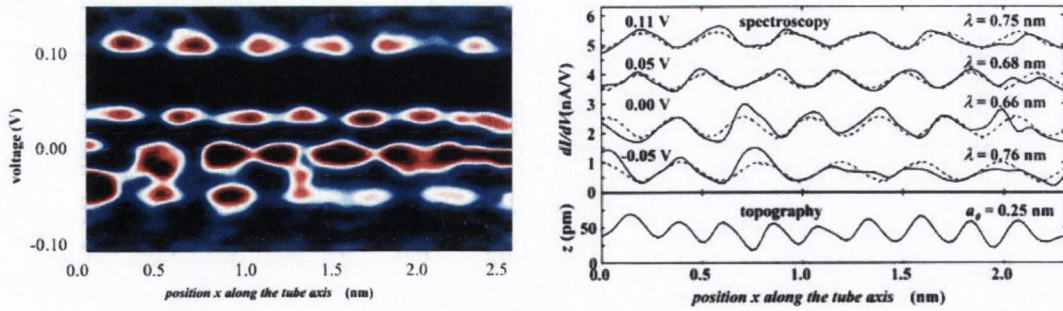
Figure 2.5 - Standing electron waves in a short nanotube observed by electron spectroscopy

Metallic nanotubes can carry very large current densities, with reports of values as high as 10^9 A cm^{-2} [34], without damage due to the stability of the sp^2 bonding,. Above a certain high threshold power, damage has been observed as the rapid oxidation of the outer shell of the MWNTs [35]. For semi-conducting nanotubes, there is a bandgap which is inversely proportional to the nanotube diameter. For diameters above ~14 nm the bandgap is comparable to the thermal energy at room temperature and the nanotubes will behave as metals. Therefore, for the majority of MWNTs, the outer shell, which has been predicted to dominate the electrical transport at low energies [36], will be metallic in nature.

Perfect metallic nanotubes are expected to be ballistic conductors, which have no intrinsic resistance. In a ballistic conductor, there is no backscattering, so every electron entering the nanotube will be emitted at the other end. Therefore, for defect free nanotubes, the mean-free-path of the electrons is greater than the length of most nanotubes. This makes the resistance independent of length. Ballistic conductance of MWNTs has been observed by various groups [1, 37].

The strength of the carbon-carbon bond results in the high tensile strength of nanotubes, as well as the stability under high currents. The Young's moduli of nanotubes is ~1 TPa and tensile strengths as high as 63 GPa have been measured [4]. These excellent mechanical properties combined with the low densities of nanotubes, as low as 1300 kg m^{-3}, gives the potential for the production of strong, lightweight materials. As phonons can also propagate easily along the nanotube, they are excellent thermal conductors, with conductivities greater than 3000 W m^{-1} K^{-1} measured for MWNTs [2]. For SWNT ropes, the thermal conductivity is much lower, at 35 W m^{-1} K^{-1} [38], demonstrating the negative effect of rope formation on the physical properties.

2.2.3 *Production of Nanotubes*

There are three main methods for the production of carbon nanotubes, arc-discharge, laser ablation, and chemical vapour deposition (CVD). Arc-discharge and laser ablation involve the condensation of carbon atoms generated by the vaporisation of a

9

graphite target. These methods produce higher quality nanotubes with less defects, but CVD represents the most likely method for large-scale production.

The arc-discharge technique was initially used to produce C_{60} fullerenes. In the arc-discharge, a plasma of helium gas, at 2500 - 3000 °C is used to vaporise graphite electrodes by passing a high direct current between them [39]. This vaporises the anode, which condenses on the cathode, forming deposits of MWNTs. The arc-discharge method can be used to grow SWNTs by filling the anode with metal catalysts, such as Iron, Cobalt or Nickel. This technique was optimised by Journet and co-workers using a carbon anode containing yttrium, and nickel [26]. As well as the nanotubes, many unwanted products are formed in the arc-discharge, such as fullerenes and amorphous carbon.

In 1996, R. E. Smalley and colleagues developed an efficient technique for the production of SWNTs using laser ablation [40]. A carbon target containing nickel (Ni) and cobalt (Co) is placed in a tube-furnace and heated to 1200 °C in a helium or argon atmosphere. This target is then vaporised by pulses of an Nd-YAG laser and the soot formed, which contains ropes of SWNTs, is deposited in a water-cooled collector. If no catalysts are used, MWNTs are formed. This technique can convert more than 50% of the target to SWNTs in the form of ropes. The apparatus used for this method is shown in figure 7. The yield can be increased to 60 – 80 % by using two lasers with pulses 50 ns apart to maintain growth conditions over a larger volume for a longer time. Impurities such as carbon nanoparticles are also formed by this process.
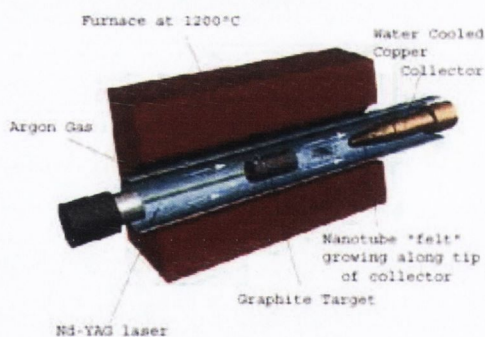
Fig. 7 – Apparatus used for laser ablation production of SWNTs in a quartz tube at 1200 °C [41].

Chemical Vapour Deposition (CVD) involves the catalytic pyrolysis of hydrocarbons, providing carbon atoms for nanotube growth. The hydrocarbon (usually acetylene or methane), and a carrier gas (argon) are heated in a furnace in the presence of catalytic particles patterned on a substrate. As the gas is heated, the hydrocarbon decomposes, catalysed by metal particles, such as cobalt, nickel or iron. The carbon atoms produced precipitate and form nanotubes. Catalysts are required to grow both SWNTs and MWNTs using this technique. Larger quantities of nanotubes can be grown, at lower

temperatures (600 – 1000 °C), using CVD, but they are of an inferior quality to those produced by the other two methods and they all contain metal catalysts as impurities. The nanotubes used in the work presented here were produced by CVD and this is discussed in more detail in chapter 3. Despite the greater number of defects and the presence of catalyst particles, CVD is likely to be the main source of nanotubes, due to the larger quantities that can be produced, compared to the laser ablation and arc-discharge techniques. Also, greater control over nanotube diameter [42], positioning [43] and alignment [44] is possible by controlling the patterning of the catalyst.

An important advance in the production of SWNTs was the HiPCO process [45], which allowed production in bulk quantities. This is, effectively, a CVD process without any substrate. The SWNTs are grown in a flowing gaseous mixture of carbon monoxide (CO) and iron pentacarbonyl, $Fe(CO)_5$. Carbon monoxide (CO) at high pressure is used as the carbon feedstock and this is mixed with a small amount of $FeCO_5$. At 250 °C, the $FeCO_5$ decomposes, and the products react forming iron clusters which act as the metal catalyst for the nanotube growth. Above 500 °C, CO disproportionates by the reaction:

$$CO_{(g)} + CO_{(g)} \rightarrow C_{(s)} + CO_{2(g)}$$
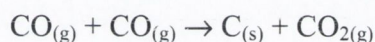
This solid carbon nucleates and grows into SWNTs on the iron clusters. By controlling the pressure of the CO, the size and diameters of the SWNTs produced can be controlled. Unfortunately, as with all the other SWNT production techniques, metal catalyst, and possibly other impurities, are present in the produced material.

2.2.4 *Difficulties with Carbon Nanotubes*

None of the production techniques discussed above have been shown to be able to produce large quantities of impurity and defect-free nanotubes at a reasonable cost yet. This makes the practical uses of nanotubes limited. The purification of raw nanotube powder has not been fully optimised either, with many of the techniques being based on oxidation of nanotube soot [46]. Oxidation removes the impurities, but also oxidises the nanotubes which can destroy them completely, reducing the final yield, or modifies their electronic properties.

The nanotube soot from any of these production techniques contains nanotubes with a wide range of electronic properties due to the lack of control over helicity and diameters. A practical technique for complete separation of the metallic and semi-conducting nanotubes has yet to be found, although some partial separation on a small scale has been demonstrated [47, 48]. Electronic applications of nanotubes, whether it be

11

using them as transistors (requiring semi-conducting nanotubes), or using them for interconnects in microchips (requiring metallic nanotubes), will require a method to completely separate these two different types of nanotubes.

Nanotubes are insoluble in almost all known solvents, but solution based processing requires the dispersion of the nanotubes. At present, this has only been achieved by functionalisation, which strongly affects their electronic properties if many groups are attached, or by using surfactants [49] or polymers [50] to stabilise the nanotube dispersion. Even when single-walled nanotubes (SWNTs) have been dispersed in a solvent using surfactants or polymers, aggregation is still a problem [51]. Furthermore, the use of surfactants and polymers limit the number of potential applications as they are difficult to remove from the nanotubes.

For most applications it is preferable to have isolated SWNTs, but the van der Waals interactions between SWNTs makes this difficult to achieve at any useful concentration. Individual SWNTs have been observed in polymer solutions [51] and in dispersions in NMP [6], but only at very low concentrations. All of these difficulties are obstacles preventing the full potential of carbon nanotubes being achieved in many possible applications. The dispersion problems are particularly important for the preparation of composites. Low aspect ratio fillers are desirable for electrically conductive and mechanically reinforced composites [24, 25], but aggregation reduces the effective aspect ratio of the fillers. Also, the weak inter-nanotube forces cause aggregates that reduce the effective reinforcement, as has been observed at high concentrations [52]. For these reasons, inorganic MoSI nanowires, which are not susceptible to many of the problems of CNTs, are also investigated as an alternative filler material in this thesis.

2.3 MoSI Nanowires

Many different inorganic nanowires [8, 9] have been produced for use in similar applications to CNTs. Unfortunately, many of these suffer from similar problems to CNTs, and some have created new problems, which have yet to be overcome. In 2001, Remskar et al. reported the production of identical "subnanometer diameter single-wall MoS_2 nanotubes" [53] which could be easily dispersed in ethanol using ultrasound. As they are identical, this MoS_2 nanotube material has the advantage of uniform electronic properties (all metallic [54]) and the potential for simple processing due to its dispersability. As well as this, it was shown that these inorganic nanotubes have a Young's modulus comparable to carbon nanotubes (120 GPa [54]) and excellent field emission properties [55].

12

Unfortunately, the synthesis of this material is quite complicated and not easily reproducible.
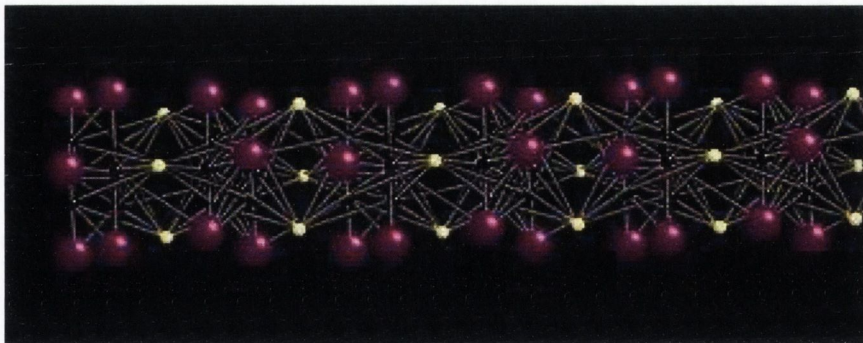
Figure 2.6 – The structure of a single $Mo_6S_3I_6$ nanowire as determined from STEM considerations by Valeria Nicolosi [56]. The backbone of the unit cell is mainly defined by molybdenum arranged in octahedral configuration (black), sulfur atoms (yellow) form trimers in the linking plane, iodine (purple) trimers are bonded to the molybdenum atoms.

From the work of Remskar et al., three further stoichiometries, $Mo_6S_3I_6$, $Mo_6S_{4.5}I_{4.5}$ and $Mo_6S_2I_8$, which have a straight-forward, one-step synthesis were produced [12] using a transport reaction [57]. These nanowires are ~ 1 nm in diameter and the structure of a single $Mo_6S_3I_6$ nanowire is shown in figure 2.6. These nanowires, which are studied in this thesis, are produced by Professor Dragan Mihailovic's group in the Jožef Stefan Institute in Ljubljana, Slovenia. The nanowires have many advantages, but most importantly they have a simple and scalable synthetic process [12], and each stoichiometry is identical [12]. These nanowires are also easily dispersed in solvents [14], which is due to the dimensions of the nanowires, but also could be due to the structure of the nanowires. As there are iodine atoms along the surface of individual nanowires, there could be a local dipole, aiding their dispersion in some solvents. The material is formed in large bundles, but these can easily be broken up and dispersed by sonication. Due to the identical properties of each stoichiometry, the formation of bundles is not as significant a problem as ropes of SWNTs. Local density approximation band structure calculations of the $Mo_6S_3I_6$ nanowire predict it to be semi-metallic [58], and ohmic behaviour of this stoichiometry has been observed [59]. The $Mo_6S_2I_8$ stoichiometry has been reported to be metallic [60], while the $Mo_6S_{4.5}I_{4.5}$ nanowires electronic structure has not been reported. The physical properties of the nanowires [10], suggest they could be used in many of the applications for which CNTs have been proposed. A comparison of the properties of these nanowires and CNTs is shown in table 2.1. Of particular interest is the high Young's modulus and significant electrical conductivity of the $Mo_6S_3I_6$ and $Mo_6S_{4.5}I_{4.5}$ nanowires.

	Comment	MWCNTs	SWCNTs	$MoS_2I_{1/3}$	$Mo_6S_3I_6$	$Mo_6S_{4.5}I_{4.5}$
Young's modulus – longitudinal (GPa)[1]	Ropes	>1000 Chopra et al Nature **377**, 135 (1995)	1200 (Salvetat PRL **82** 944, (1995))	120	430	420
Shear modulus (GPa)	ropes	14.2±8 Chopra et al Nature **377**, 135 (1995)	1-10 (Salvetat PRL **82** 944, (1995))	0.160	0.32	0.8
Electrical conductivity	longitudinal		>1000 Scm⁻¹ (metallic) Ugawa et al PRB **60** R11305 (1999)		0.01-10 S cm⁻¹	0.1-10 S cm⁻¹
Li capacity (Li per Mo)		N/A	N/A	Up to 3 (1.2 reversible)	8.6/f.u.	
Dispersability without surfactant		limited	limited	Polar solvents, water, isopropanol, HCl	Polar solvents, water, isopropanol, HCl	Polar solvents, water, isopropanol, HCl
Thermal stability in air (decomp. Temperature in C)		>600	>600	>350C	>350 C	>350C
Thermal stability in vacuum (decomp. Temperature in C)		>1000	>1000	>800C	>1200 C	>1200C

Table 2.1– Table comparing physical properties of carbon nanotubes and MoSI nanowires [10].

Previous research on $Mo_6S_{4.5}I_{4.5}$ nanowires [14] have shown approximately 12 wt% of the as-produced material to be soluble in isopropanol, with a solubility of up to 0.34 g L^{-1}. This work also showed that the impurities rapidly sediment out of solution in this solvent, giving us a simple purification technique. Therefore, this material is easier to purify, process, and characterise than carbon nanotubes. These dispersion properties, and the simple synthesis and the identical electronic properties, suggest them for many applications. In particular, the electrical conductivity and high Young's modulus, combined with the ease with which they are dispersed, makes them promising as fillers for polymer composites, as investigated in this thesis.

The properties of these MoSI nanowires also show the prospect of many other applications. The simplest yet investigated is their use as an alternative lubricating additive for oil, due to their low shear modulus [10]. MoS_2 is currently used, but lower sulphur contents are desired. The $Mo_6S_{4.5}I_{4.5}$ have been investigated for this purpose and observed to perform well [61]. The production of field emission devices from $Mo_6S_3I_6$ nanowires has been demonstrated to be quite simple and the nanowires have shown excellent performance, with stable field emission currents of over 1 μA observed from an individual bundle [62]. As the electronic properties are identical for each stoichiometry, it is not necessary to achieve single nanowires for many applications. This is a significant advantage for the production of conducting composite materials using these nanowires, where they have been shown to have a very low percolation threshold of 1.3×10^{-5} [20]. These results demonstrate the potential for the MoSI nanowires in a variety of applications.

2.4 Sedimentation Theory

Initial reports suggested that the $Mo_6S_3I_6$ nanowire material is easily dispersed in common solvents [12]. In order to analyse the solubility of the material in a range of solvents, a model describing the local concentration of sedimenting particles as a function of time has been derived by Nicolosi et al. [14]. Using this theory, the sedimentation data could be quantitatively analysed for the sedimentation observed in dispersions of the $Mo_6S_3I_6$ material in various solvents, similar to the analysis previously performed for the $Mo_6S_{4.5}I_{4.5}$ material [63]. The derivation of the sedimentation theory will be described here.

Using the assumptions [64-66] that:

the solid particles are small with respect to the vessel and all have the same density,

the constituents of the solution are incompressible,

there is no mass transfer between the solid and the fluid phases during sedimentation,

a particulate system can be described by field variables that must obey the two Navier-Stokes equations, which express the local conservation equations for mass, equation 2.2, and linear momentum, equation 2.3, [64-66].

$$\frac{\partial C}{\partial t} + \nabla(C v_S) = 0 \qquad \text{Equation 2.2}$$

$$\rho_s \frac{\partial}{\partial t}(C v_s) + \rho_s \nabla(C v_s^2) = -\nabla(C p_f) - C \rho_s g + \beta \nabla C \qquad \text{Equation 2.3}$$

where C is the local concentration of the sedimenting phase under study, ρ_s is the solid component density, v_s is the velocity of the solid component, p_f is the fluid pressure, g is the acceleration due to gravity, and β is related to the solid-fluid interaction force and has the dimensions of pressure.

The fluid pressure only varies in the z-direction, allowing the simplification,

$$-\frac{\partial p_f}{\partial z} = \rho_l g \qquad \text{Equation 2.4}$$

Therefore, equation 2.2 and equation 2.3 can be solved to give,

$$\frac{\partial C}{\partial t} = \frac{-C g (\rho_s - \rho_l) v_s - \rho_s C v_s . \frac{dv_s}{dt_s}}{(\beta - p_f)} \qquad \text{Equation 2.5}$$

The forces acting on any single particle are gravity, buoyancy and the viscous drag force. Therefore, from Newton's second law, we can write:

$$m\frac{dv_s}{dt} = mgb - fv_s$$

Equation 2.6

where m is the mass per sedimentation particle, b is the buoyancy correction factor ($b = 1 - p_l / p_s$), and f is the frictional coefficient as given by Stokes' law. The solutions of this equation for dv_s/dt and v_s are:

$$v_s = \frac{mgb}{f}(1 - e^{-(f/m)t})$$

Equation 2.7

$$\frac{dv_s}{dt} = gbe^{-(f/m)t}$$

Equation 2.8

The mass per sedimentation particle m and the frictional coefficient f can be estimated from the known properties of this system and from this it can be shown that the exponential decays on the order of seconds. This is much shorter than the timescale of the sedimentation, and therefore the exponentials can be neglected. Substituting equation 2.7 and equation 2.8 into equation 2.5, and integrating gives

$$C = C_n \exp\left(-\frac{g^2(\rho_s - \rho_l)mb}{f(\beta - p_f)}t\right) = C_n e^{-t/\tau_n}$$

Equation 2.9

where C_n is a constant, and $\tau_n = \frac{f(\beta - p_f)}{g^2(\rho_s - \rho_l)mb}$

Equation 2.10

We can also modify this model to apply specifically to spherical or cylindrical species. The Stokes' relation for spherical particles is $f = 6\pi\eta a$, where η is the solvent viscosity and a is the particle radius. Also, the mass of the spherical particles is given by, $m = 4\rho_s\pi a^3/3$. Therefore, the time constant, τ, can be rewritten for spherical and cylindrical particles to be:

$$\tau_{spherical} = \frac{9\eta(\beta - p_f)}{2g^2(\rho_s - \rho_l)^2 a^2}$$

Equation 2.11

For cylindrical particles, the Stokes' relation is $f = 6K\pi\eta c$, where $c = \left(\frac{3r^2 l}{4}\right)^{1/3}$ for cylindrical particles. The drag coefficient, K, makes the expression for cylindrical particles more complicated, as it also depends on the dimensions, length, l, and radius, r, of the particles [65]:

$$K = \frac{\left(\dfrac{l}{r}\right)^{2/3}}{\left(\dfrac{3}{2}\right)^{1/3}\left[2Ln\left(\dfrac{l}{r}\right) - 0.11\right]}$$ Equation 2.12
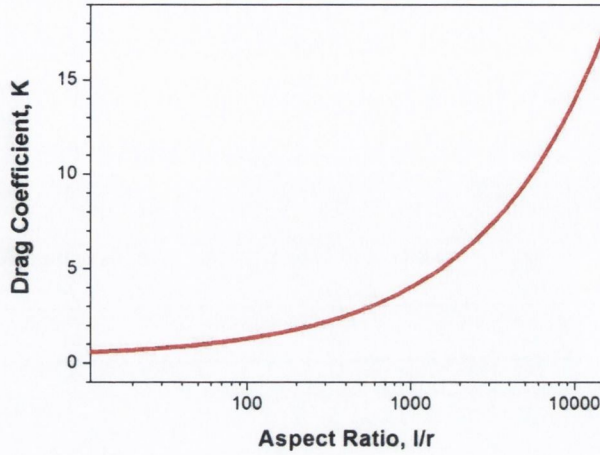
Figure 2.7– Plot of the drag coefficient for cylindrical particles, from the Stokes' relation, as a function of aspect ratio.

The calculated drag coefficient, K, is plotted as a function of aspect ratio, l/r, in figure 2.7. This indicates that the friction increases quite rapidly with increasing aspect ratio, with K approximately increasing as $(l/r)^{2/3}$ for large aspect ratios. As the aspect ratio increases, the surface area per unit volume of a cylinder increases and hence the friction increases, observed as an increase in the drag coefficient, K. Thus, the time constant for cylindrical objects is given by:

$$\tau_{cylindrical} = \frac{6K\eta(\beta - p_f)(3/4)^{1/3}}{g^2(\rho_s - \rho_l)^2(r^2l)^{2/3}}$$ Equation 2.13

As there may be many components in the as-produced nanowire materials, there could be many sedimenting phases. In this situation, the total concentration measured as a function of time will be,

$$C(t) = C_0 + \sum_n C_n e^{-t/\tau_n}$$ Equation 2.14

where C_0 is the concentration of the non-sedimenting phase, C_n and τ_n are the initial concentrations and the time constant of the nth sedimenting phase, respectively. Therefore, the total initial concentration, C_{Total}, from equation 8, is given by,

$$C_{Total} = C_0 + \sum_n C_n$$ Equation 2.15

Therefore, equation 2.9 describes the sedimentation of a non-soluble phase from a dispersion as a function of time and equation 2.14 describes the concentration of a dispersion of n non-soluble components and one soluble component as a function of time.

17

2.5 Electrically Conductive Composites

The addition of filler materials to a polymer matrix can produce electrically conductive composites if the filler materials can from a complete pathway, allowing current to flow through the matrix. This is normally a stochastic process, as the geometry of the filler materials in the matrix is completely random. Percolation theory, which was originally used to describe fluid flowing in a network of channels in the 1950s [67], has since developed to describe the electrical properties of quite complicated composite systems [68-70]. It has since been extensively applied to composites to predict [25, 71, 72] and analyse their electrical properties [20, 22, 73]. In this chapter, percolation theory is introduced and the relevant developments in the theory and experimental practice are described.

2.5.1 Percolation Theory

Percolation theory describes random systems which have a sharp phase transition at which *long-range* connectivity suddenly appears or disappears [70]. The point at which the transition occurs is called the percolation threshold. This theory can be applied to a whole range of physical and chemical phenomena, such as the flow of liquid in a porous medium, the glass transition, polymer gelation and the conductor-to-insulator transition in composites which is the application in this thesis.
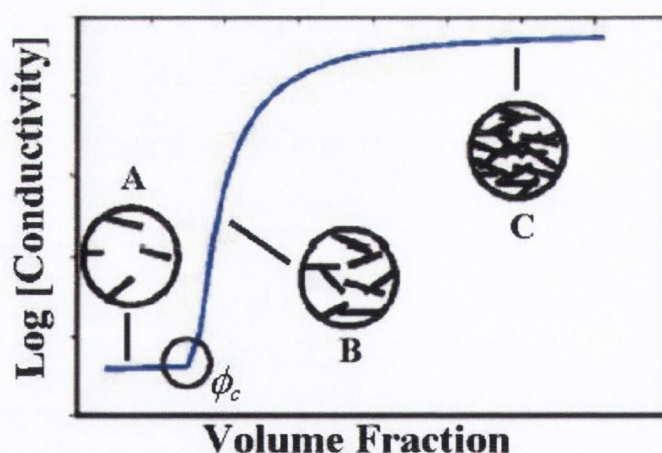
Figure 2.8 – A sample plot of the predicted dependence of conductivity on the concentration of the conductive filler material in an insulating matrix. Below the percolation threshold, ϕ_c, (A) no network exists to allow conduction. Just above ϕ_c, (B) long-range connectivity begins to appear and conduction can occur, and at (C) multiple parallel conductive paths exist and the conductivity only increases slowly with increasing filler content.

For conductive fillers in an insulating polymer matrix, the percolation threshold, ϕ_c, is defined as the filler concentration at which the composite conductivity begins to rise above the conductivity of the polymer. Just above ϕ_c the conductivity starts to rise slowly,

18

but as the concentration of filler material, ϕ, is increased further, the conductivity rises more rapidly as more parallel pathways appear. This is illustrated in figure 2.8. This increase in the conductivity of the system can be described by the percolation law (equation 2.16), but this is only valid in the critical region near the percolation threshold, where $|\phi - \phi_c| \ll 1$.

$$\sigma = \sigma_0 (\phi - \phi_c)^t \qquad \text{Equation 2.16}$$

where t is the critical conductivity exponent, and σ_0 is a proportionality constant, which will be called the conductivity prefactor here. The conductivity prefactor is an extrapolation of the percolation law to 100% filler material. It does not necessarily equal the conductivity of the pure filler material, as the percolation law is not valid that far from the percolation threshold, ϕ_c. Conductance barriers between the filler particles will reduce the conductivity of the system and have been assigned as the cause of low values for the conductivity prefactor [74].

Further work by Scher and Zallen [75], studying geometric percolation on regular lattices found that the percolation threshold was an approximately constant volume fraction for all lattices in a particular dimensionality. This suggested that as with the critical exponent, t, the percolation threshold was also a dimensional invariant. They showed that the critical volume fraction for all two-dimensional lattices was ~0.44, and ~0.15 for three-dimensional lattices. Unfortunately, this work was calculated for randomly placed conducting and insulating spheres on the regular lattices and cannot be applied to more complicated systems, such as composites of one-dimensional nanoparticles. These systems have a larger number of parameters that must be included, the range of filler particle sizes [71], filler aspect ratio [25], effects of the polymer on the filler [73], etc.

2.5.2 *Excluded Volume*

For the more complex systems, Balberg et al. [71, 76] showed that the excluded volume, V_{ex}, of the filler particles could be used to predict the percolation threshold. The excluded volume is defined as the volume around an object into which the centre of a similar object is not allowed to enter if overlapping of the two objects is to be avoided [76]. For spheres, it can be shown that V_{ex} is simply eight times the volume of the sphere. In the case of nanotubes and nanowires, which are can be closely approximated as cylinders, the derivation of the excluded volume is not as simple as there is an angular dependence, as shown in figure 2.9.

19
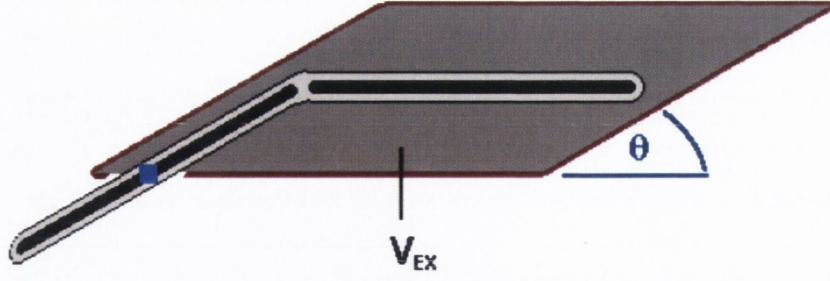
Figure 2.9 – Diagram illustrating the excluded volume, V_{ex}, of two cylindrical objects oriented at an angle θ to each other.

The aspect ratios of nanotubes and nanowires are generally quite large and it has been shown that in this situation, they can be considered as interpenetrating objects in order to simplify the calculations [68]. If the volume fraction of the cylindrical fillers is V, and therefore the volume fraction of the polymer is $(1 - V)$, the probability of any position in the composite being polymer is $(1 - V)$. We can consider this system at the percolation threshold, where the volume fraction of the fillers is ϕ_c by definition, and the critical number of fillers, N_c, is present in the system. For interpenetrating fillers, the probability that any position in the composite is the polymer matrix is now given by,

$$1 - \phi_c = (1 - V)^{N_c}$$

Equation 2.17

$$\Rightarrow \phi_c = 1 - (1 - V)^{N_c} = 1 - \left[1 - \frac{N_c V_{ex} V}{V_{ex}} \cdot \frac{1}{N_c} \right]$$

Equation 2.18

Balberg et al. showed that in the limit of an infinite system, where $V \to 0$, and $N_c \to \infty$, the ratio V/V_{ex} and the total excluded volume $V_{exTOT} = N_c V_{ex}$ become constants.

Expanding and simplifying equation 2.18, it becomes,

$$\phi_c = 1 - \exp\left(1 - \frac{N_c V_{ex} V}{V_{ex}} \right)$$

$$= 1 - \exp\left(1 - \frac{V_{exTOT} V}{V_{ex}} \right)$$

Equation 2.19

$$= 1 - \exp(-N_c V)$$

Therefore the percolation threshold can be calculated for the system, if the critical number, N_c, is known or, normally, from the ratio V_{exTOT}/V_{ex}.

In a system of randomly oriented objects, the excluded volume is depends on the relative orientation of the fillers and therefore the average excluded volume, $<V_{ex}>$, and average total excluded volume, $<V_{exTOT}>$, must be used in equation 2.19. The calculation of the average excluded volume for capped cylinders has been previously calculated [76] and will be derived here.

The excluded volume of two capped cylinders of length, L, and diameter, d, and with an angle γ between there long axes is given by,

$$V_{ex} = \frac{4\pi d^3}{3} + 2\pi d^2 L + 2dL^2 \sin\gamma$$

$$= 8V + 2dL^2 \sin\gamma$$

Equation 2.20

where V is the volume of one capped cylinder.

To find the average excluded volume, $<V_{ex}>$, it is necessary to average $\sin\gamma$ over all possible solid angles of stick i and stick j. This has been calculated for θ_i and θ_j confined to an angle of $2\theta_\mu$ around the z-axis. For aligned cylinders, where $\theta_\mu = 0$, the average value of $\sin\gamma$, $<\sin\gamma>_\mu$, is 0 [76] and the average excluded volume is simply eight times the volume of one cylinder, which is analogous to the case of spheres.

$$\langle V_{ex} \rangle = \frac{4\pi d^3}{3} + 2\pi d^2 L$$

Equation 2.21

For an isotropic system of cylinders, where $\theta_\mu = \pi/2$, $<\sin\gamma>_\mu$ has been calculated to be $\pi/4$ [76]. Therefore, the average excluded volume for an isotropic system of capped cylinders is,

$$V_{ex} = \frac{4\pi d^3}{3} + 2\pi d^2 L + \frac{\pi dL^2}{2}$$

$$= 8V + \frac{\pi dL^2}{2}$$

Equation 2.22

Using this equation, the volume of the cylinder, V, and the value for the constant value of 1.4 for the total excluded volume also calculated by Balberg [71], equation 2.19 can be used to calculate a percolation threshold for this system of isotropic capped cylinders.

$$\phi_c = 1 - \exp\left[\frac{-1.4\left(\frac{4\pi d^3}{3} + 2\pi d^2 L \right)}{\frac{4\pi d^3}{3} + 2\pi d^2 L + \frac{\pi dL^2}{2}} \right]$$

Equation 2.23

For high aspect ratio cylinders, where $L/d \gg 1$, this expression can be simplified to,

$$\phi_c = 1 - \exp\left(-0.7 \frac{d}{L} \right) \sim 0.7 \frac{d}{L}$$

Equation 2.24

This is very similar to the limits found by Garboczi et al. [25] for high aspect ratio prolate ellipsoids,

21

$$\phi_c \sim 0.6 \frac{d}{L}$$ <div style="text-align:right">Equation 2.25</div>

From Monte Carlo simulations for a range of aspect ratios, they also determined that the percolation threshold scaled inversely with aspect ratio for aspect ratios above 10. In this limit, a prolate ellipsoid would approximate a capped cylinder, and hence a nanotube or nanowire, very well. Other studies have also indicated that the percolation threshold should decrease as the aspect ratio increases, although other parameters were included, so a direct expression was not derived [69]. These predictions suggest that one-dimensional nanostructures are ideal fillers for conductive composites, due to their high aspect ratios. It should also be noted that for systems with a distribution of cylindrical filler sizes, the aspect ratio has been predicted to decrease as the distribution broadens [71, 74].

2.5.3 *Critical Exponent*

Initially, the critical exponent was thought to only depend on the dimensionality of the percolating system, with t predicted to be 1.1 for two-dimensional systems and 1.65 for three-dimensional systems by Zallen [70]. More recent work has restated these values as 1.3 for two dimensions and 2 for three dimensions [72], although they were still believed to be dimensional invariants.. As with the predictions for the percolation threshold described previously, further work has shown the critical exponent only has these "universal" values in the limit of low aspect ratio fillers and when there are no tunnelling barriers in the system.

For other systems, the critical exponent can vary greatly. Balberg et al. [77] used a random void model to explain deviations in the critical exponent to values as high as 6. There, it was demonstrated that t should be increased in systems where the conductive filler particles are separated by resistive connections with a distribution of resistivity values. This would correspond to a situation where the filler particles are separated by tunnelling barriers. This result was experimentally tested by measuring the piezoelectric response of a glass doped with conducting RuO_2 filler particles [78]. They prepared a range of volume fraction samples with different filler particle sizes and which were fired at different temperatures and measured their percolation parameters. All the percolation parameters varied over the range of sizes and firing temperatures, with the critical exponent rising from $t = 2.15$ up to $t = 3.84$. The piezoelectric response, change of resistivity under applied strain, was then measured for all the samples. For the sample where the critical exponent without strain applied was, $t \sim 2$, and thus no tunnelling barriers are expected to be present, the piezoelectric response did not change much with

the volume fraction of the RuO$_2$ fillers. For the samples with higher critical exponents, which suggests tunnelling barriers are present, the piezoelectric response diverged logarithmically at the percolation threshold. This effect was assigned to these higher critical exponents being strain dependent causing the conductivity, and hence the piezoelectric response, to vary with volume fraction. This would be caused by the distance between filler particles being increased as the strain was increased, thus increasing the mean tunnelling distance, which agrees with the predictions of Balberg [77]. For the samples with $t \sim 2$, no tunnelling barriers are expected to be present and therefore the increase in strain has little effect on the resistivity.

As well as being predicted to increase under certain conditions, the critical exponent has also been predicted to decrease with increasing aspect ratio of filler particles [68]. The excluded volume model developed by Balberg [76], was used for these calculations and the results are shown in figure 2.10. This shows the critical exponent is very sensitive to the aspect ratio of fillers, such as nanotubes and nanowires. The increasing aspect ratio will counteract the effect of the tunnelling barriers described above, which are normally observed in composites, leading to a wide variation in the possible values of t, from as low as ~ 1.2 to as high as 6 [79].
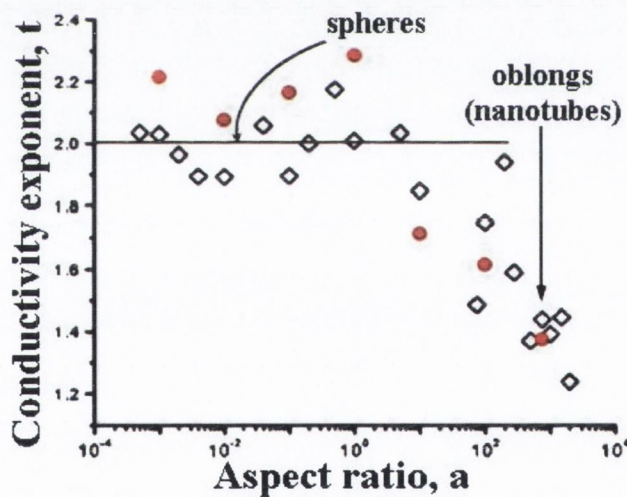
Figure 2.10 – Prediction of the variation of the critical exponent, t, as a function of aspect ratio calculated by Monte Carlo simulation, taken from Foygel et al. [68].

2.5.4 *Attractive Forces*

An important aspect in the process of achieving composites with good electrical properties is the preparation of the composites. The effect of sample preparation is becoming recognised as important for composites [80]. The interactions of the system components are not accounted for by percolation theory, but recent results suggest they do effect percolation. From computational work using a model of SWNTs in a polymer

matrix, Grucjicic et al. showed that van der Waals' interactions between the nanotubes which encourage alignment will increase in the percolation threshold, although this was accompanied by an increase in the maximum conductivity of the composites. This has been contradicted by other groups [74, 81], who suggested that small attractive forces between SWNTs, which could hold neighbouring SWNTs in contact, will significantly lower the percolation threshold.

The solution to this disagreement is provided by the work of Vigolo et al. on "sticky nanotubes" [73]. They performed a study on HiPCO SWNTs dispersed in water using the surfactant sodium dodecyl sulphate (SDS). By varying the relative concentration of SDS to SWNTs, the degree of attraction between the SWNTs and hence the size of SWNT clusters can be controlled. The origin of this attractive force is the depletion attraction. The SDS forms micelles around individual nanotubes. If the distance between the nanotubes is smaller than the size of the SDS molecules, the SDS is unable to enter the area between them. This results in an osmotic pressure of the micelles on the nanotubes, which is observed as an attraction between the nanotubes. The strength of the attraction is directly proportional to the osmotic pressure of the micelles, which is itself proportional to the micelle concentration.

For a fixed SWNT concentration, the onset of percolation will occur above a definite SDS concentration and this was measured. This procedure was only repeated for two other SWNT concentrations, as the range of possible concentrations is limited by the ability to detect the onset of percolation at low SWNT concentrations and the preparation of homogeneous SWNT dispersions at high concentrations. In the region where the measurements were performed an increase in the attractive potential of $0.006kT$ was observed to decrease the percolation threshold by a factor of three.

2.6 Mechanical Reinforcement of Composites

By far, the majority of research of reinforcement of composites with one-dimensional structures has been focussed on carbon nanotubes as the filler material [52, 82], but inorganic nanowires have also been investigated [23]. To understand the mechanism of mechanical reinforcement of composites, many different models have been created [83]. Here, the "rule of mixtures" [84] and the Halpin-Tsai theories [85] are described, as they are used in this work, and commonly used in nanotube composite work [52, 86, 87], to understand the mechanical properties of the composites prepared.

24

2.6.1 Rule of mixtures

In the rule of mixtures, the reinforcing fibres are assumed to be aligned and to span the full length of the composite and that there is perfect stress transfer between the matrix and the fibres. Hence, equal strain occurs for both the fibre and the matrix. In this situation, the Young's moduli of the composite parallel, $Y_{C\parallel}$ and perpendicular, $Y_{C\perp}$, to the fibre direction are:

$$Y_{C\parallel} = \phi_f Y_f + (1 - \phi_f)Y_m \quad \text{and} \quad Y_{C\perp} = \frac{Y_f Y_m}{\phi_f Y_m + (1 - \phi_f)Y_f} \qquad \text{Equation 2.26}$$

where Y_f and Y_m are the moduli of the fibre and matrix respectively, and ϕ_f is the volume fraction of the fibre.

2.6.2 Cox shear lag theory

As the "rule of mixtures" only applies when the fibres at least as long as the composites, it cannot be applied to nanostructure reinforced composites as their lengths, ~ 1 µm, are substantially less than any composite films prepared. When shorter fibres are used in composites, the stresses applied to the composite are transferred from the matrix to the filler via interfacial shear stresses. Nanoparticles are ideal for reinforcement because of their high surface area to volume ratio, which maximises the area available for interfacial stress transfer from the polymer matrix, thus allowing greater stress transfer. It is also important to ensure there is a strong interaction between the nanotube and the polymer matrix to achieve good reinforcement, which can be achieved by functionalisation of the nanotubes [88], in-situ polymerisation of the polymer with the nanotubes [89], or for semi-crystalline polymer by crystallisation around the nanotubes [21].

For systems where short fibres are used for reinforcement, Cox derived his shear lag theory [90]. This states that for aligned fibres in a composite, the Young's modulus of the composite, Y_C is:

$$Y_C = \eta_l \phi_f Y_f + (1 - \phi_f)Y_m \qquad \text{Equation 2.27}$$

where,

$$\eta_l = 1 - \frac{Tanh(a\,{}^l/_d)}{a\,{}^l/_d} \qquad \text{Equation 2.28}$$

The η_l term is the length efficiency factor which describes the reduced effective modulus of the reinforcement fibres due to their shorter length, l. The other terms are d, the diameter, and a which is given by, $a = \sqrt{\dfrac{-3Y_m}{2Y_f Ln\phi_f}}$.

This can be further modified for randomly oriented fibres in the matrix by introducing the Krenchel orientation efficiency factor [83], η_0, becoming,

$$Y_C = \eta_0 \eta_l \phi_f Y_f + (1 - \phi_f) Y_m$$

<div align="right">Equation 2.29</div>

The orientation efficiency factor is given by the equation,

$$\eta_0 = \frac{\sum_n a_{fn} \cos^4 \alpha_n}{\sum_n a_{fn}}, \quad \text{where } \sum_n a_{fn} = 1$$

where a_{fn} is the ratio between the cross-sectional area presented by a group of fibres orientated at an angle α_{fn} to the applied load direction and the total area of all the fibres at a given cross-section of the composite. The number of groups are designated by $n = 1, 2, 3,$ ...., n.

For aligned fibres, η_0, becomes 1, and equation 2.29 simplifies to equation 2.27. For fibres aligned in a plane, η_0 is 0.375 and for randomly orientated fibres it has a value of 0.2 [52].

2.6.3 *Halpin-Tsai Theory*

The Halpin-Tsai theory [85] was developed in the 1960s for continuous fibre composites. It involves a further refinement, and complication, of equation 2.29 and describes systems with a distribution of fibre lengths and orientations well. However, it should be noted that this theory is known to underestimate the increase in modulus at high volume fractions [52].

For randomly oriented fibres in a composite, the Halpin-Tsai equation is,

$$Y_C = \frac{3}{8} \left(\frac{1 + \zeta \eta_L \phi_f}{1 - \eta_L \phi_f} \right) Y_m + \frac{5}{8} \left(\frac{1 + 2\eta_T \phi_f}{1 - \eta_T \phi_f} \right) Y_m$$

<div align="right">Equation 2.30</div>

In this equation, $\zeta = 2 \frac{l}{d}$, twice the fibre aspect ratio and the η_L and η_T parameters are given by:

$$\eta_L = \frac{Y_f/Y_m - 1}{Y_f/Y_m + \zeta} \qquad \text{and} \qquad \eta_T = \frac{Y_f/Y_m - 1}{Y_f/Y_m + 2}$$

2.6.4 *Summary*

These models have all been used to analyse carbon nanotube composites [52, 83] and inorganic nanowire composites [23] successfully. There have been instances where the experimental results did not agree with these models [91], but the disagreement was assigned to due to reinforcement by crystallisation of the polymer. In general, the theory

described here works well for carbon nanotube composites. Only one report of nanowire reinforcement was found in the literature, making it difficult to be sure the theory is accurate for nanowires also.

These models predict the increase of composite Young's modulus, Y_C, with increasing filler volume fraction, ϕ, and with increasing aspect ratio, l/d. Therefore, a convenient parameter for comparing mechanical reinforcement of different systems would be the rate of increase of the Young's modulus of the composite as a function of volume fraction, $dY_c/d\phi$, at low volume fractions. This allows a comparison of not only the increase in the Young's modulus attained, but also the filler content required to achieve the increase.

2.7 References

[1]   S. Frank, P. Poncharal, Z. L. Wang, and W. A. de Heer, Science 280 (1998) 1744.

[2]   P. Kim, L. Shi, A. Majumdar, and P. L. McEuen, Physical Review Letters 87 (2001) 215502.

[3]   M. M. J. Treacy, T. W. Ebbesen, and J. M. Gibson, Nature 381 (1996) 678.

[4]   M.-F. Yu, O. Lourie, M. J. Dyer, K. Moloni, T. F. Kelly, and R. S. Ruoff, Science 287 (2000) 637.

[5]   C. A. Furtado, U. J. Kim, H. R. Gutierrez, L. Pan, E. C. Dickey, and P. C. Eklund, Journal of the American Chemical Society 126 (2004) 6095.

[6]   S. Giordani, S. D. Bergin, V. Nicolosi, S. Lebedkin, M. M. Kappes, W. J. Blau, and J. N. Coleman, Journal of Physical Chemistry B 110 (2006) 15708.

[7]   S. E. Moulton, A. I. Minett, R. Murphy, K. P. Ryan, D. McCarthy, J. N. Coleman, W. J. Blau, and G. G. Wallace, Carbon 43 (2005) 1879.

[8]   Y. Xia, P. Yang, Y. Sun, Y. Wu, B. Mayers, B. Gates, Y. Yin, F. Kim, and H. Yan, Advanced Materials 15 (2003) 353.

[9]   M. Remskar, Advanced Materials 16 (2004) 1497.

[10]   Mo6 d.o.o., http://www.mo6.com (2007)

[11]   A. Meden, A. Kodre, J. Padeznik Gomilsek, I. Arcon, I. Vilfan, D. Vrbanic, A. Mrzel, and D. Mihailovic, Nanotechnology 16 (2005) 1578.

[12]   D. Vrbanic, M. Remskar, A. Jesih, A. Mrzel, P. Umek, M. Ponikvar, B. Jancar, A. Meden, B. Novosel, S. Pejovnik, P. Venturini, J. C. Coleman, and D. Mihailovic, Nanotechnology 15 (2004) 635.

[13]   D. N. McCarthy, V. Nicolosi, D. Vengust, D. Mihailovic, G. Compagnini, W. J. Blau, and J. N. Coleman, Journal of Applied Physics 101 (2007) 014317.

[14]   V. Nicolosi, D. Vrbanic, A. Mrzel, J. McCauley, S. O'Flaherty, C. McGuinness, G. Compagnini, D. Mihailovic, W. J. Blau, and J. N. Coleman, Journal of Physical Chemistry B 109 (2005) 7124.

[15]   W. A. de Heer, A. Châtelain, and D. Ugarte, Science 270 (1995) 1179.

[16]   M. Zumer, B. Zajec, N. Vincenc, Z. Bojan, M. Remskar, M. Ploscaru, D. Vengust, A. Mrzel, and D. Mihailovic, Nanotechnology 16 (2005) 1619.

[17]   F. Kreupl, A. P. Graham, G. S. Duesberg, W. Steinhogl, M. Liebau, E. Unger, and W. Honlein, Microelectronic Engineering 64 (2002) 399.

[18]   Y. Cui, Z. Zhong, D. Wang, W. U. Wang, and C. M. Lieber, Nano Letters 3 (2003) 149.

[19]   A. Javey, J. Guo, Q. Wang, M. Lundstrom, and H. Dai, Nature 424 (2003) 654.

[20]   R. Murphy, V. Nicolosi, Y. Hernandez, D. McCarthy, D. Rickard, D. Vrbanic, A. Mrzel, D. Mihailovic, W. J. Blau, and J. N. Coleman, Scripta Materialia 54 (2006) 417.

[21]   K. P. Ryan, M. Cadek, V. Nicolosi, S. Walker, M. Ruether, A. Fonseca, J. B. Nagy, W. J. Blau, and J. N. Coleman, Synthetic Metals 156 (2006) 332.

[22]   J. K. W. Sandler, J. E. Kirk, I. A. Kinloch, M. S. P. Shaffer, and A. H. Windle, Polymer 44 (2003) 5893.

[23]   S. R. C. Vivekchand, U. Ramamurty, and C. N. R. Rao, Nanotechnology 17 (2006) S344.

[24]   M. Cadek, J. N. Coleman, K. P. Ryan, V. Nicolosi, G. Bister, A. Fonseca, J. B. Nagy, K. Szostak, F. Beguin, and W. J. Blau, Nano Letters 4 (2004) 353.

[25]   E. J. Garboczi, K. A. Snyder, J. F. Douglas, and M. F. Thorpe, Physical Review E 52 (1995) 819.

[26]   C. Journet, W. K. Maser, P. Bernier, A. Loiseau, M. L. de la Chapelle, S. Lefrant, P. Deniard, R. Lee, and J. E. Fischer, Nature 388 (1997) 756.

[27]   From http://www.ipc.uni-karlsruhe.de/mik/english/195.php (2007)

[28]   From http://www.applied-nanotech.com/cntproperties.htm (2007)

[29]   From http://www.weizmann.ac.il/condmat/imry/images/nano26b.gif (2007)

[30]   J. P. Lu, Physical Review Letters 79 (1997) 1297.

[31]   A. Thess, R. Lee, P. Nikolaev, H. Dai, P. Petit, J. Robert, C. Xu, Y. H. Lee, S. G. Kim, A. G. Rinzler, D. T. Colbert, G. E. Scuseria, D. Tomanek, J. E. Fischer, and R. E. Smalley, Science 273 (1996) 483.

[32]   P. Harris, Carbon Nanotubes and Related Structures, Cambridge University Press, Cambridge, 2001.

[33]   J. W. Mintmire, B. I. Dunlap, and C. T. White, Physical Review Letters 68 (1992) 631.

[34]   B. Q. Wei, R. Vajtai, and P. M. Ajayan, Applied Physics Letters 79 (2001) 1172.

[35]   P. G. Collins, M. Hersam, M. Arnold, R. Martel, and P. Avouris, Physical Review Letters 86 (2001) 3128.

[36]   C. Schönenberger, A. Bachtold, C. Strunk, J. P. Salvetat, and L. Forró, Applied Physics A: Materials Science & Processing 69 (1999) 283.

[37]   P. Poncharal, C. Berger, Y. Yi, Z. L. Wang, and W. A. de Heer, Journal of Physical Chemistry B 106 (2002) 12104.

[38]   J. Hone, M. Whitney, C. Piskoti, and A. Zettl, Physical Review B 59 (1999) R2514.

[39] M. Cadek, R. Murphy, B. McCarthy, A. Drury, B. Lahr, R. C. Barklie, M. in het Panhuis, J. N. Coleman, and W. J. Blau, Carbon 40 (2002) 923.

[40] T. Guo, P. Nikolaev, A. Thess, D. T. Colbert, and R. E. Smalley, Chemical Physics Letters 243 (1995) 49.

[41] B. I. Yakobson and R. E. Smalley, American Scientist 85 (1997) 324.

[42] I. Willems, Z. Konya, J. F. Colomer, G. Van Tendeloo, N. Nagaraju, A. Fonseca, and J. B. Nagy, Chemical Physics Letters 317 (2000) 71.

[43] Z. F. Ren, Z. P. Huang, D. Z. Wang, J. G. Wen, J. W. Xu, J. H. Wang, L. E. Calvet, J. Chen, J. F. Klemic, and M. A. Reed, Applied Physics Letters 75 (1999) 1086.

[44] B. Q. Wei, R. Vajtai, Y. Jung, J. Ward, R. Zhang, G. Ramanath, and P. M. Ajayan, Nature 416 (2002) 495.

[45] P. Nikolaev, M. J. Bronikowski, R. K. Bradley, F. Rohmund, D. T. Colbert, K. A. Smith, and R. E. Smalley, Chemical Physics Letters 313 (1999) 91.

[46] C. N. R. Rao and A. Govindaraj, Nanotubes and Nanowires, The Royal Society of Chemistry, Cambridge, 2005.

[47] Z. Chen, X. Du, M. H. Du, C. D. Rancken, H. P. Cheng, and A. G. Rinzler, Nano Letters 3 (2003) 1245.

[48] R. Krupke, F. Hennrich, H. v. Lohneysen, and M. M. Kappes, Science 301 (2003) 344.

[49] M. J. O'Connell, S. M. Bachilo, C. B. Huffman, V. C. Moore, M. S. Strano, E. H. Haroz, K. L. Rialon, P. J. Boul, W. H. Noon, C. Kittrell, J. Ma, R. H. Hauge, R. B. Weisman, and R. E. Smalley, Science 297 (2002) 593.

[50] R. Murphy, J. N. Coleman, M. Cadek, B. McCarthy, M. Bent, A. Drury, R. C. Barklie, and W. J. Blau, Journal of Physical Chemistry B 106 (2002) 3087.

[51] J. N. Coleman, A. Fleming, S. Maier, S. O'Flaherty, A. I. Minett, M. S. Ferreira, S. Hutzler, and W. J. Blau, Journal of Physical Chemistry B 108 (2004) 3446.

[52] J. N. Coleman, U. Khan, W. J. Blau, and Y. K. Gun'ko, Carbon 44 (2006) 1624.

[53] M. Remskar, A. Mrzel, Z. Skraba, A. Jesih, M. Ceh, J. Demsar, P. Stadelmann, F. Levy, and D. Mihailovic, Science 292 (2001) 479.

[54] A. Kis, D. Mihailovic, M. Remskar, A. Mrzel, A. Jesih, I. Piwonski, A. J. Kulik, W. Benoît, and L. Forró, Advanced Materials 15 (2003) 733.

[55] V. Nemanic, M. Zumer, B. Zajec, J. Pahor, M. Remskar, A. Mrzel, P. Panjan, and D. Mihailovic, Applied Physics Letters 82 (2003) 4573.

[56] V. Nicolosi Ph.D. Thesis, in the School of Physics, Trinity College Dublin, Ireland, 2006.

[57]   R. Nitsche, Journal of Physics and Chemistry of Solids 17 (1960) 163.

[58]   A. Meden, A. Kodre, J. Padeznik Gomilsek, I. Arcon, I. Vilfan, D. Vrbanic, A. Mrzel, and D. Mihailovic, Nanotechnology 16 (2005) 1578.

[59]   B. Bercic, U. Pirnat, P. Kusar, D. Dvorsek, D. Mihailovic, D. Vengust, and B. Podobnik, Applied Physics Letters 88 (2006) 173103.

[60]   A. Hassanien, M. Tokumoto, A. Mrzel, D. Mihailovic, and H. Kataura, Physica E: Low-dimensional Systems and Nanostructures 29 (2005) 684.

[61]   L. Joly-Pottuz, F. Dassenoy, J. M. Martin, D. Vrbanic, A. Mrzel, D. Mihailovic, W. Vogel, and G. Montagnac, Tribology Letters 18 (2005) 385.

[62]   M. Zumer, B. Zajec, N. Vincenc, Z. Bojan, R. Maja, P. Mihaela, V. Damjan, M. Ales, and M. Dragan, Nanotechnology 16 (2005) 1619.

[63]   V. Nicolosi, D. Vrbanic, A. Mrzel, J. McCauley, S. O'Flaherty, D. Mihailovic, W. J. Blau, and J. N. Coleman, Chemical Physics Letters 401 (2005) 13.

[64]   P. Garrido, F. Concha, and R. Burger, International Journal of Mineral Processing 72 (2003) 57.

[65]   P. W. Atkins, Physical Chemistry, 4th edition, Oxford University Press, 1992.

[66]   R. Burger, S. Evje, K. Hvistendahl Karlsen, and K. A. Lie, Chemical Engineering Journal 80 (2000) 91.

[67]   J. M. Hammersley, Annals of Mathematical Statistics 28 (1957) 790.

[68]   M. Foygel, R. D. Morris, D. Anez, S. French, and V. L. Sobolev, Physical Review B 71 (2005) 104201.

[69]   S. H. Munson-McGee, Physical Review B 43 (1991) 3331.

[70]   R. Zallen, The Physics of Amorphous Solids, Wiley, 1983.

[71]   I. Balberg, Physical Review B 31 (1985) 4053.

[72]   D. Stauffer and A. Aharony, Introduction to Percolation Theory, Taylor & Francis, 1991.

[73]   B. Vigolo, C. Coulon, M. Maugey, C. Zakri, and P. Poulin, Science 309 (2005) 920.

[74]   D. S. McLachlan, C. Chiteme, C. Park, K. E. Wise, S. E. Lowther, P. T. Lillehei, E. J. Siochi, and J. S. Harrison, Journal of Polymer Science Part B: Polymer Physics 43 (2005) 3273.

[75]   H. Scher and R. Zallen, The Journal of Chemical Physics 53 (1970) 3759.

[76]   I. Balberg, C. H. Anderson, S. Alexander, and N. Wagner, Physical Review B 30 (1984) 3933.

[77]   I. Balberg, Physical Review B 57 (1998) 13351.

[78] S. Vionnet-Menot, C. Grimaldi, T. Maeder, S. Strassler, and P. Ryser, Physical Review B 71 (2005) 064201.

[79] J. Wu and D. S. McLachlan, Physical Review B 56 (1997) 1236.

[80] M. E. Mackay, A. Tuteja, P. M. Duxbury, C. J. Hawker, B. Van Horn, Z. Guan, G. Chen, and R. S. Krishnan, Science 311 (2006) 1740.

[81] X. Wang and A. P. Chatterjee, The Journal of Chemical Physics 118 (2003) 10787.

[82] O. Breuer and U. Sundararaj, Polymer Composites 25 (2004) 630.

[83] M. D. F. O'Regan, Akay, and B. Meenan, Composites Science and Technology 59 (1999) 419.

[84] W. D. Callister, Materials Science and Engineering, an introduction, Wiley, New York, 2003.

[85] J. C. Halpin and J. L. Kardos, Polymer Engineering & Science 16 (1976) 344.

[86] M. S. P. Shaffer and A. H. Windle, Advanced Materials 11 (1999) 937.

[87] J. K. W. Sandler, S. Pegel, M. Cadek, F. Gojny, M. van Es, J. Lohmar, W. J. Blau, K. Schulte, A. H. Windle, and M. S. P. Shaffer, Polymer 45 (2004) 2001.

[88] R. Blake, Y. K. Gun'ko, J. Coleman, M. Cadek, A. Fonseca, J. B. Nagy, and W. J. Blau, Journal of the American Chemical Society 126 (2004) 10226.

[89] D. Blond, V. Barron, M. Ruether, K. P. Ryan, V. Nicolosi, W. J. Blau, and J. N. Coleman, Advanced Functional Materials 16 (2006) 1608.

[90] H. L. Cox, British Journal of Applied Physics 3 (1952) 72.

[91] M. Cadek, J. N. Coleman, V. Barron, K. Hedicke, and W. J. Blau, Applied Physics Letters 81 (2002) 5123.

CHAPTER 3

Materials & Experimental Techniques

3.1 Introduction

In this chapter, the production of the various materials used is described briefly. These were all purchased commercially or produced by collaborators. The different methods of sample preparation and the techniques used to analyse the samples are then described, with the main emphasis on the electrical and mechanical characterisation.

3.2 Production of Raw Materials

3.2.1 *Production of Carbon Nanotubes*

Carbon nanotubes (NTs) can be produced using several different techniques, such as arc-discharge [1], laser ablation [2] and chemical vapour deposition (CVD) [3]. The NT composites prepared here used thin multi-wall NTs produced using the CVD technique by Nanocyl S.A., Belgium [4]. The basic CVD method involves the catalytic pyrolysis of hydrocarbon feedstock gas. A schematic of the apparatus is shown below in figure 3.1. A transition metal catalyst is used, and it also nucleates the growth of the carbon NTs. Many different variants of this process exist, as it is possible to alter almost all of the parameters, including the feedstock gas, substrates [5, 6], catalyst [6] and the form of the catalyst [5, 7].
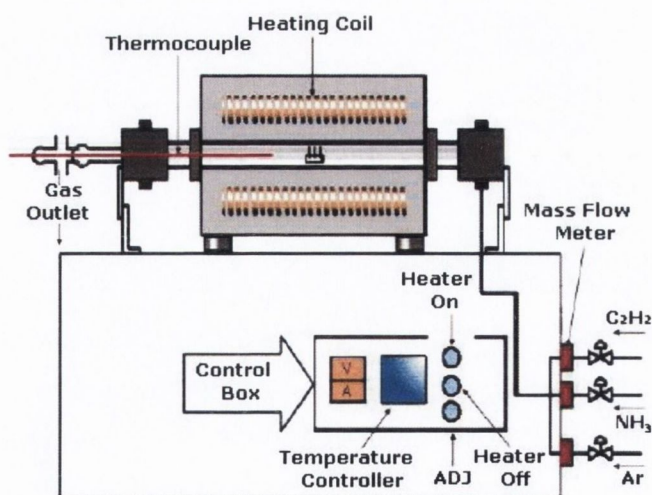
Figure 3.1 - Schematic of a Chemical Vapour Deposition Apparatus [8].

The growth of NTs using different CVD techniques and with different parameters has been investigated [9], allowing a high degree of control over the dimensions of CVD

grown NTs. By patterning the catalyst particles the alignment and positioning of the NTs can also be controlled. The percolation threshold for NT/polymer composites is predicted to be inversely proportional to the aspect ratio of the nanotubes [10, 11]. Also, it has previously been shown that small diameter multi-wall NTs are best for reinforcement of NT/polymer composites [12]. Therefore, the optimal NTs for use as a filler material in composites are small diameter multi-wall NTs. These are produced by the research group of Prof. J. B. Nagy at the University of Namur, Belgium [6], who are associated with Nanocyl S.A. The NTs received are listed as having been purified to greater than 95% carbon, and as having an average diameter of 10 nm. The average diameter of the received nanotubes was measured by SEM to be 14 ± 6 nm [13], agreeing with the quoted value.

3.2.2 *Synthesis of $Mo_6S_{9-x}I_x$ Nanowires*

In general, several nanowire stoichiometries with the general formula $Mo_6S_{9-x}I_x$ can be produced using the same synthetic procedure [14], but by varying the initial amounts of the elemental material. $Mo_6S_3I_6$ and $Mo_6S_{4.5}I_{4.5}$ nanowire material were used in this research. The raw elemental material - molybdenum platelets (0.1 mm thick foil), sulphur powder and iodine – were sealed in an evacuated glass ampoule of 19 mm diameter and 140 mm long, with a remaining gas pressure below 10^{-2} Pa. This was heated in a furnace to 1070 °C at a rate of 8 K h^{-1}. Following 72 hours at this temperature, the ampoule was cooled at 1.5 K min^{-1}. The material produced by this process is in the form of needles of approximately 100 nm to 1000 nm in diameter, containing bundles of nanowires, with each nanowire having a diameter of 0.96 nm [15].
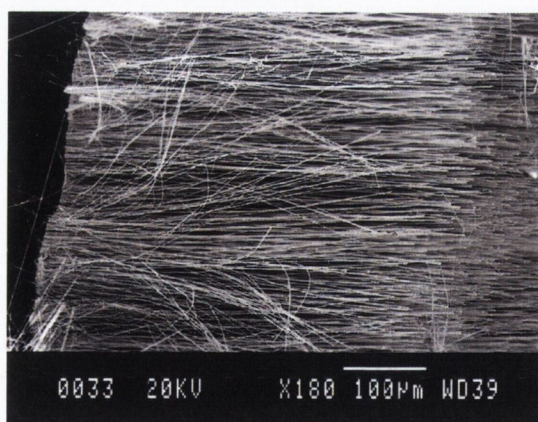
Figure 3.2 - Scanning Electron Micrograph of the as-produced $Mo_6S_3I_6$ nanowire material [14].

34

3.3 Preparation of Mo$_6$S$_3$I$_6$ Dispersions & Sedimentation Apparatus

3.3.1 *Washing of the as-produced Mo$_6$S$_3$I$_6$ material*

The as-produced Mo$_6$S$_3$I$_6$ material was found to contain large quantities of unreacted iodine when it was dispersed in various solvents. Even at the low concentrations used in the initial work (0.1 g L^{-1}), the solutions were observed to turn a clear yellow colour over the course of a week. This is due to the excess iodine which has been reported as one of the impurities present from the synthesis[14], and was also observed with the raw Mo$_6$S$_{4.5}$I$_{4.5}$ material.

The excess iodine was removed from the raw Mo$_6$S$_3$I$_6$ material by washing in acetone, as acetone is known to react with iodine, according to the following reaction:

$$CH_3\text{-}CO\text{-}CH_3 + I_2 \rightarrow CH_3\text{-}CO\text{-}CH_2I + I^-$$

The as-produced powder was mixed with acetone and sonicated in a low power ultrasonic bath. This mixture was then centrifuged at 1000 rpm for 120 minutes, and then decanted to separate the Mo$_6$S$_3$I$_6$ powder from the acetone. This was repeated, and each time a UV-vis spectrum was taken of the acetone removed from the Mo$_6$S$_3$I$_6$, as shown in figure 3.3 for the first batch of as-produced Mo$_6$S$_3$I$_6$ powder washed. Two peaks are observed in the visible region of the spectrum at ~ 450 nm and ~700 nm, allowing the amount of iodine extracted into the acetone to be monitored.
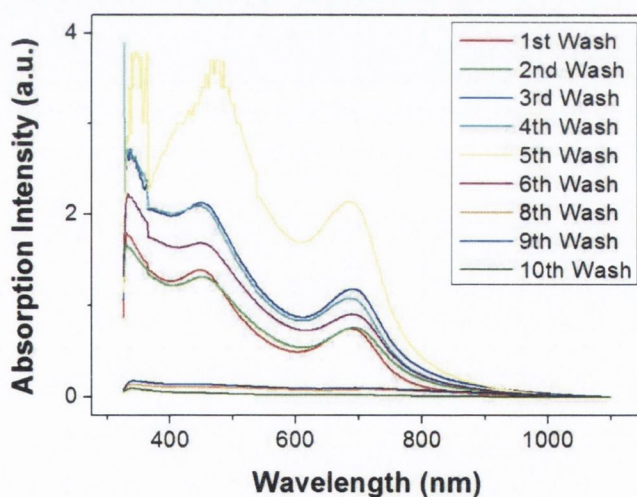
Figure 3.3 - UV-vis absorption spectra of the acetone removed after each washing of the first batch of raw Mo$_6$S$_3$I$_6$ powder

To clearly demonstrate the effect of the repeated washing, the intensity of the absorption peak at approximately 450 nm is plotted against the number of washes for the first and second batches washed in figure 3.4. The washing was continued until the intensity of the iodine peaks had dropped significantly, after 8 washes for the first batch and 10 washes for the second batch. The difference between the two curves is due to the

sonication time. For the first batch the sonication time was steadily increased to increase the amount of iodine extracted by each wash, which reaches a peak at the 5th wash cycle. For the second batch, the sonication time was kept approximately constant, and the maximum amount of iodine was extracted during the 2nd wash.
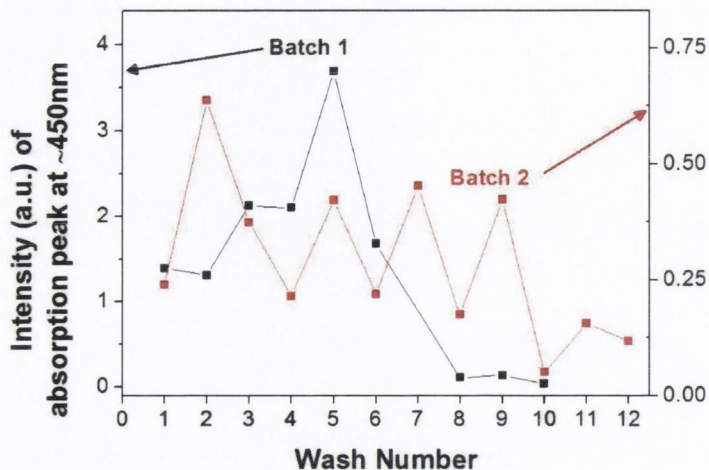
Figure 3.4 - Absorption intensity of the peak at ~ 450 nm plotted against the number of washes for the first and second batches of $Mo_6S_3I_6$ powder washed.

The $Mo_6S_3I_6$ powder was weighed before washing was begun and after the washing was completed. For the first batch, the mass of powder before washing was 103.7 mg, and after washing was 74.8 mg. For the second batch the masses were 111.1 mg and 98.6 mg respectively. These correspond to 27.9% and 11.2% iodine by mass for the first and second batches. For the $Mo_6S_{4.5}I_{4.5}$, a similar procedure was used and the iodine content was found to be between 36% and 53.6% of the starting mass, showing a similarly large variation between batches.

3.3.2 *Sedimentation of $Mo_6S_3I_6$ Dispersions*

For the sedimentation studies of the $Mo_6S_3I_6$ material, the washed powder was used to prepare the nanowire dispersions to ensure the iodine would not affect the results. These dispersions were prepared by adding $Mo_6S_3I_6$ washed material to a range of solvents at a concentration of 0.1 g L^{-1}. These mixtures were then sonicated with a high power ultrasonic tip (120W, 60 kHz) for 16 minutes to break up the larger particles and disperse the material. Following this, the dispersions were placed in a low power ultrasonic bath (50W) for 2 hours to homogenise the dispersion.

Immediately after sonication, a TEM grid of each of the dispersions was prepared by drop-casting. The dispersions were then transferred to a 1 cm quartz cuvette and this was placed in the sedimentation apparatus, as shown in figure 3.5.
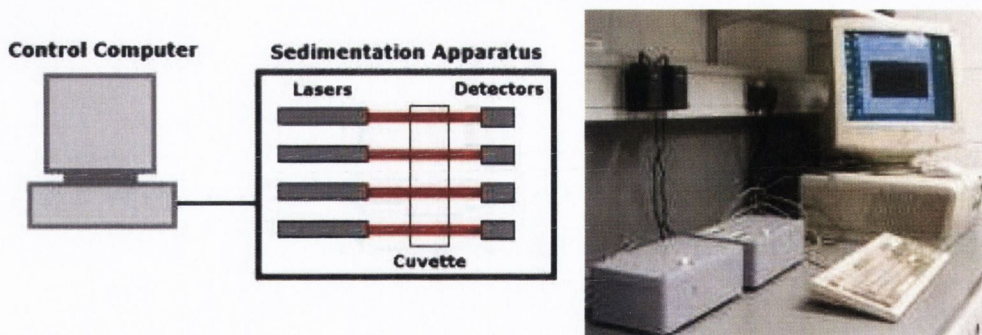
Figure 3.5 – A diagram of the sedimentation apparatus (left), where the cuvette would contain the dispersion being monitored, and a photo of these devices (right). The sedimentation apparatuses are the grey boxes to the left of the photo.

This apparatus consists of four lasers stacked vertically across from four detectors, with the cuvette placed between them. The transmission of the lasers ($\lambda = 650$ nm, pulse duration = 10 ms) through the cuvette could then be measured as a function of time. The transmission of the four lasers through the cuvette was averaged and this was then converted to absorbance, A, using the Beer-Lambert law,

$$A = \ln(I_0/I) = \alpha_{Eff} C_{Eff} l \qquad \text{Equation 3.1}$$

where I/I_0 is the transmittance of the dispersion, α_{Eff} is the effective absorption coefficient, C_{Eff} is the effective concentration and l is the path length. Here the subscript, "effective" is used, as the absorbance of all the species in the sample are probed, without knowing the actual absorption coefficient of any phase. As the absorbance is directly proportional to the effective concentration, C_{Eff}, it can be scaled to represent C_{Eff} by normalising to the initial concentration (0.1 g L^{-1}). Therefore, using the sedimentation apparatus, it is possible to monitor the rate of change of the effective concentration of the dispersions as a function of time.

As illustrated by equation 3.1, this technique probes the sample absorbance as a function of time. This absorbance is the sum of the absorbances for all the species in the sample, some of which may be stable and some of which may be sedimenting.

In analogy with equation 2.14 from the sedimentation theory, the absorbance as a function of time, $A(t)$, is then

$$A(t) = A_0 + \sum_n A_n e^{-t/\tau_n} \qquad \text{Equation 3.2}$$

where A_0 is the absorbance due to all the soluble phases:

$$A_0 = \sum_{sol} \alpha_{sol} C_{sol} l \qquad\qquad \text{Equation 3.3}$$

where "sol" represents the summation over all soluble phases, α represents the absorption co-efficient of each soluble phase, C represents the concentration of each soluble phase and l is the thickness of the cuvette. Similarly, A_n is the absorbance due to the nth insoluble phase with $A_n = \alpha_n C_n l$.

This means that unless the absorption coefficients of each phase are known we cannot extract the absolute concentrations of each phase. Thus we work in terms of effective concentration as described above. In the limit where the absorption coefficients of all phases are equal, the effective concentration equals the real concentration.

3.3.3 *Removal of Iodine from $Mo_6S_3I_6$ by Annealing*

As an alternative to washing the as-produced $Mo_6S_3I_6$ material, Prof. Mihailovic's group at the Jozef Stefan Institute, Slovenia have used annealing under vacuum to remove the excess iodine. The $Mo_6S_3I_6$ nanowires are known to be stable under vacuum up to 1200 °C [16], whereas iodine sublimes easily and boils at 185 °C at S.T.P [17], allowing the iodine to evaporate well below the decomposition temperature of the $Mo_6S_3I_6$ nanowires. Here, the as-produced $Mo_6S_3I_6$ material was annealed at 800 °C.

Previously, annealing at a range of temperatures, up to 900 °C, in a sealed quartz ampoule at a pressure of 10^{-7} bar for 12 hours has been reported [18]. No structural change in the $Mo_6S_3I_6$ nanowires was detected after annealing, indicating the iodine removed was not from the nanowires themselves. At annealing temperatures above 700 °C, a deposit, which was identified as iodine by UV-vis spectroscopy, was observed. As an added advantage to this method, the electrical conductivity of the material was observed to increase from 0.04 S m^{-1} before annealing to 0.2 S m^{-1} after annealing.

3.4 Preparation of Composite Films

Much work has been done using carbon nanotubes as filler materials in polymer composites for mechanical reinforcement, and also for increased conductivity [19-21]. The MoSI nanowires are a promising alternative to NTs, as they are easier to disperse in solvents and do not have the same bundling problems as SWNTs. Here, composites using both thin multi-walled NTs (MWNTs) and MoSI nanowires were produced using similar procedures in order to examine their mechanical and electrical properties.

3.4.1 Preparation of Thin MWNT/First Contact composites

First Contact [22] (previously called Opticlean) is a commercially available product for cleaning optical components. It is a solution of an elastomeric polymer which can be painted on and then, once dry, peeled off removing any surface contamination [23]. The effectiveness of the First Contact product is demonstrated in figure 3.6. A polished silicon wafer had an X diamond scribed into it, and a SEM of this is shown on the left in figure 3.6. On the right, a SEM of the same silicon wafer is shown after the First Contact polymer solution was painted on, allowed to dry, and the film was then peeled off. No dirt or silicon fragments are observed on the wafer after cleaning with the First Contact solution. From sedimentation measurements performed, it is clear that solutions of this polymer are able to stably disperse a large fraction of carbon nanotubes; up to an effective concentration, c_{eff}, of 85% after 3 days (see figure 3.7).
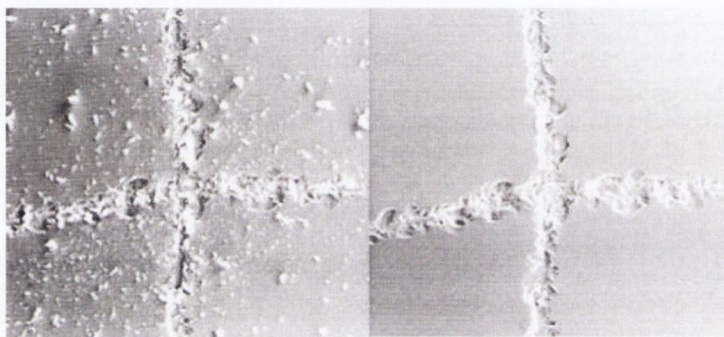
Figure 3.6 – SEM images of a polished silicon wafer with grooves cut in it by a diamond scribe before, and after cleaning with First Contact [22].

Composites of thin MWNTs with this polymer were prepared to examine their mechanical and electrical properties. The First Contact solution was diluted to 29 g L^{-1}, as it is quite concentrated as received. 9 ml of this solution was added to 22.5 mg of the thin MWNTs and this was sonicated with the high power ultrasonic tip for 8 minutes to disperse the MWNTs, and then placed in the ultrasonic bath for 4 hours to homogenise the mixture. After this, the composite solution was allowed to stand, during which any larger or unstable lumps sedimented. After 3 days the transmission had stabilised indicating the majority of sedimentation had completed and the sample was decanted. Before being left to stand, 0.1 ml of the solution was placed in a separate sample bottle, and after decantation and a further sonication with ultrasonic tip another 0.1 ml was removed. The relative transmission of the two solutions was measured using a UV-vis spectrometer. From the decrease in transmission after decantation, the concentration of MWNTs in the solution after decantation could be calculated.
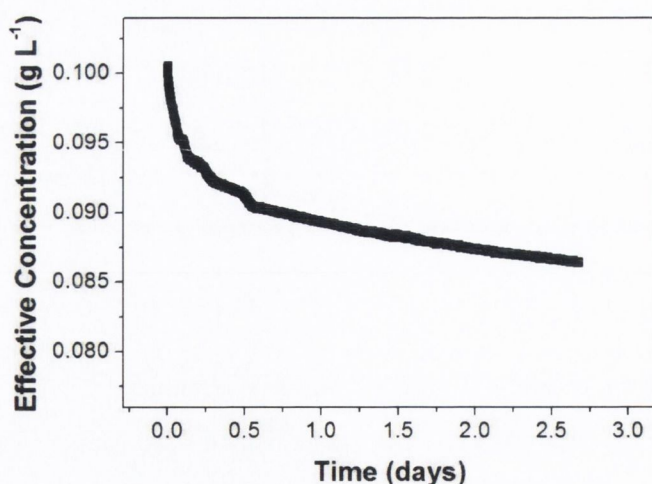
Figure 3.7 - Sedimentation of thin MWNTs against time as measured using the sedimentation apparatus.

A range of volume fractions was then produced by diluting in a series of steps, sonicating each dilution with the ultrasonic tip between dilutions. These composite solutions were then sonicated again with the ultrasonic tip, and films of the solutions were made by drop-casting them in glass petri dishes in an oven at 30°C. Once all the films had been drop-cast, including a pure First Contact solution with no NTs added, they were dried under vacuum with no heating applied. After several hours the films were quite dry, and they were peeled from the petri dishes and then left to dry for several days under vacuum. From these films, samples were cut for electrical and mechanical measurements. It was observed in the electrical measurements, that the nanotube concentration was far above the percolation threshold, so a second batch of films was prepared using the same preparation procedures, but with lower MWNT concentrations. Only electrical measurements were performed on this second batch of samples.

3.4.2 *Preparation of MoSI Nanowire Composites*

For the MoSI nanowires, composites with Poly(methyl methacrylate) (PMMA) were produced using commercially available PMMA. Chloroform has previously been shown to be a good solvent for the $Mo_6S_{4.5}I_{4.5}$ nanowires [15] and DMF for $Mo_6S_3I_6$ nanowires [24], and PMMA was chosen as it dissolves easily in both these solvents.

A dispersion of $Mo_6S_{4.5}I_{4.5}$ nanowires was prepared by adding 9 ml of chloroform to 44.8 mg of the unwashed, as-produced nanowire powder and sonicating this mixture with the high power ultrasonic tip for 8 minutes. Previously, this sonication time was determined to be optimal for the nanowire material to be well dispersed and to have only small bundles of nanowires remain [25]. 270 mg of PMMA powder was added to this dispersion, and it was sonicated with the ultrasonic tip again for 8 minutes to thoroughly

40

mix the polymer and nanowires. This composite solution was then sonicated in a low power ultrasonic bath for 2 hours to ensure it was homogeneous. Upon removal from the ultrasonic bath, some sediment was visible at the bottom of the sample bottle. To remove this, the composite solution was decanted. This sediment was left to dry in an oven at 60°C and was found to weigh 31.5 mg, indicating that 13.3 mg remained dispersed with the PMMA.

A stock solution of PMMA in chloroform was prepared at a concentration of 30 g L^{-1} and placed in the ultrasonic bath. This solution was blended with the original composite solution, after decantation, to produce a range of volume fractions, ϕ, from the original 0.012 to 3.6×10^{-4}. Films of these composite solutions were made by sonicating the composite solutions again with the ultrasonic tip to ensure good dispersion, and then immediately drop-casting the solutions into teflon dishes in a vacuum oven at 40 °C. A film of the PMMA stock solution was also prepared. Before the films had completely dried, they were peeled from the teflon dishes and then further dried overnight under vacuum to completely evaporate the solvent. This is necessary as the films quite strongly adhere to the teflon dishes when completely dry. From these films, samples were cut for mechanical analysis.

A film of $Mo_6S_3I_6$ in PMMA was prepared with DMF as the solvent using similar methods to those described above, to test its electrical properties. The volume fraction of the $Mo_6S_3I_6$/PMMA composite solution was 0.023. The film was dropcast on a glass slide and allowed to dry in the vacuum oven, as the boiling point of DMF is quite high, at 153 °C.

3.5 Electrical Characterisation

3.5.1 *Electrical Characterisation of Raw Materials*

Before measuring the electrical properties of the polymer composites, the electrical conductivities of the raw materials, thin MWNTs and MoSI nanowires, were measured. This was done using the apparatus shown in figure 3.8. A small, weighed amount of the raw material, m_s, (carbon nanotubes or MoSI nanowires) was placed in the cavity at the centre of the Teflon disc, and a metal rod, with a diameter slightly less than the cavity is inserted on top of the sample. This allows electrical contact to be made across the sample, between the copper base plate and the metal rod. If necessary, pressure can be applied to the metal rod to improve the contact with the sample by placing light masses on top of the rod. The height of the sample, h_s, inside the cavity can be measured from the difference in height of the metal rod in the empty cavity, and in the filled cavity. Using this data, the

41

density of the sample in the cavity can be calculated (as the diameter of the cavity and hence its area, A, is already known), and the conductance of the sample, G_s, can also be measured. The conductivity of the material, σ_m, can be calculated using the formula,

$$\sigma_m = \frac{G_s h_s}{A} \cdot \frac{V_{Total}}{V_{NT}} = \frac{G_s h_s}{A} \cdot A h_s \cdot \frac{m_s}{\rho_m} = \rho_m \frac{G_s h_s^2}{m_s} \qquad \text{Equation 3.4}$$
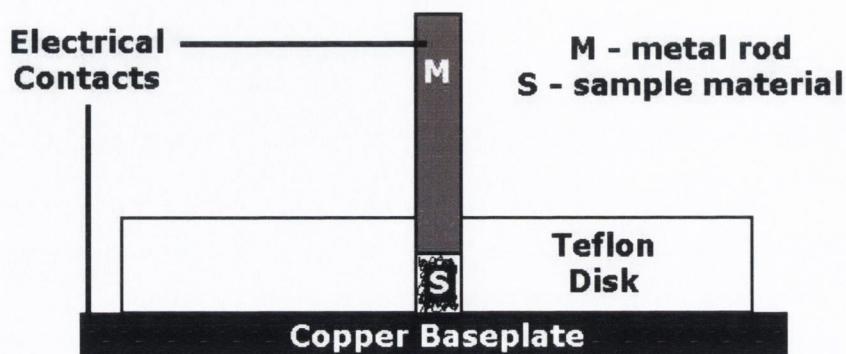
Figure 3.8 – Diagram of the apparatus used to measure the conductivities of carbon nanotube and MoSI nanowire material.

This assumes that the amount of material is sufficient to create a three dimensional network. Also, at high volume fractions the conductivity will saturate, as the number of electrical pathways will be very large and any increase in the amount of pathways will have little effect on the conductance of the system. This is similar to the situation described by the percolation law, where the conductivity also saturates.

A second method used to measure the conductivity of the raw materials was to prepare buckypaper films of the material by vacuum filtration of dispersions. Strips of the films were then cut and the resistance was low enough to be measured directly with an ohmmeter. The conductivity of the strips could then be calculated from the measured dimensions.

3.5.2 *Preparation of Electrical Devices*

The procedure for preparing the electrical devices is quite similar for both the MWNT/First Contact and the annealed $Mo_6S_3I_6$ composite. A 12 mm × 12 mm square was cut from each of the MWNT/First Contact films and their thicknesses and masses were measured using a digital micrometer screw and a balance, respectively. To make electrical contact to the device, gold electrodes were thermally evaporated onto both sides of these films. For the $Mo_6S_3I_6$/PMMA, the back stripe gold electrode had been evaporated onto the glass slide supporting the film prior to drop casting of the film. Then the six front

electrodes were evaporated on top of the deposited film once it was dried. The geometry of the contacts is shown in figure 3.9, where both sets of contacts are visible through the NT/First Contact composite film. After evaporating the gold electrodes, conductive silver paint was applied to the electrodes near the edges of the films to allow easier contact. In these regions, there is no overlap between the electrodes, ensuring the silver paint cannot short circuit the device.
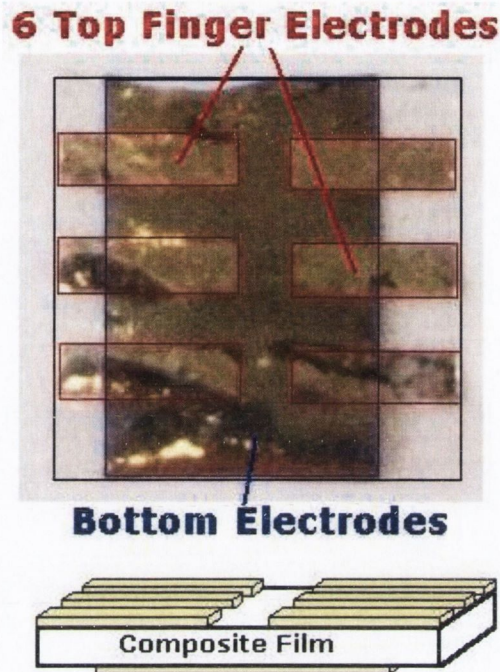
Figure 3.9 – A photograph of a 7.2×10^{-5} volume fraction NT/First Contact composite film with gold electrodes. The 6 top finger electrodes are highlighted in red, and the bottom stripe electrode is highlighted in blue. The film is quite transparent due to the low nanotube loading. Below the image is a schematic.

3.5.3 *Impedance Spectroscopy of Composite Films*

Impedance spectroscopy is a powerful technique which can measure a range of electrical properties for various systems, including dielectrics, semi-conducting and composite materials [26]. This technique allows us to investigate the dynamics of bound and mobile charge in the bulk or interfacial regions of solids or liquids. The impedance is measured by applying a small amplitude, monochromatic voltage, $v(t)=V_0 cos(\omega t)$, and measuring the resulting current response, $i(t)=I_0 cos(\omega t+\phi)$, where ϕ is the phase difference between the voltage and the current.

Using the Euler formula, these equations can be rewritten as:

$$v(t) = V_0 \operatorname{Re}[e^{i\omega t}],$$ Equation 3.5

$$i(t) = I_0 \operatorname{Re}[e^{i\omega t} e^{-i\phi}]$$ Equation 3.6

where *Re[]* indicates the real part of a complex number. Therefore, similar to ohmic resistance, R, the impedance, Z^*, can be defined as the ratio, *v(t)/i(t)*. Due to the phase difference, the impedance is a complex function, which is written as:

$$Z^* = Z' - iZ''$$
$$= R - iX(\omega)$$ Equation 3.7

where Z' is the real part of the impedance, equal to the resistance, R, and the Z'' is the imaginary part, equal to the reactance, $X(\omega)$. In the composite films measured in this work there is no inductance, so the reactance is only due to a capacitive component. Therefore, the $X(\omega) = [\omega.C(\omega)]^{-1}$, and the reactance is negative. Thus, the minus sign in the definition of Z^* allows Z'' to be defined as positive. For $\phi = 0$, the impedance is real, frequency independent and solely an ohmic resistance, whereas for $\phi = 90°$, the impedance is imaginary, frequency dependent and only due to the capacitive component. The impedance can also be written in polar from:

$$Z^* = |Z^*| e^{i\phi}$$ Equation 3.8

where $|Z^*| = \sqrt{(Z')^2 + (Z'')^2}$ is the magnitude and $\phi = tan^{-1}\left(\frac{Z'}{Z''}\right)$ is the phase difference. In impedance spectroscopy, a term comparable to the conductance, G, can also be defined, known as the admittance, Y:

$$Y = \frac{1}{Z^*} = Y' + iY'' = G + iB(\omega)$$ Equation 3.9

where $B(\omega)$, the imaginary component, is the susceptance. The magnitude of the admittance, $|Y^*|$, which can be calculated from the above equations, is a measure of the charge transport, similar to the ohmic conductance.

Using a Zahner IM6e impedance spectrometer, the real and imaginary components of the impedance were measured in the frequency range from 1 Hz to 1 MHz, with 20 mV amplitude. This frequency range was constrained by the upper limit of the spectrometer, and the lower limit for efficiency. The lowest frequency the spectrometer can measure is 0.1 mHz, but this does not greatly increase the amount of information derived, while it does increase the scan-time by approximately twenty times. The impedance, Z^*, could then be converted to the *electric modulus* $|\sigma^*|$, which is a quantity similar to the conductivity, using the formula,

$$|\sigma^*(\omega)| = \frac{1}{\sqrt{(Z')^2 + (Z'')^2}} \frac{L}{A}$$

Equation 3.10

where L is the thickness of the film, and A is the overlap area between the top and bottom electrodes. For purely dielectric material, the imaginary term, Z'', will dominate the real term, Z', causing the electric modulus to be frequency dependent over the full frequency range. For other materials, Z' will dominate at lower frequencies, which is observed as the electric modulus being frequency independent.

3.5.4 D.C. Electrical Characterisation of Composite Films

After impedance spectroscopy, all composite films had D.C. current-voltage (I-V) characteristics measured in order to calculate the electrical conductivity. A Keithley Model 2400 sourcemeter controlled by a Visual Basic program was used for the measurements. The I-Vs were measured for a range of voltages in both forward and reverse bias, starting at 1 V and up to a maximum of 10 V. The conductances, G, of each these was calculated from the slopes of the linear I-Vs around 0 V. The conductance for each sample was then calculated from the average of the conductances as measured from the I-Vs for each of the six electrodes. This was converted to D.C. conductivity, σ_{DC}, using the formula,

$$\sigma_{DC} = \left(\frac{I}{V}\right)\left(\frac{L}{A}\right)$$

Equation 3.11

where L and A are the same thickness and area as in the impedance analysis above.

3.6 Mechanical Characterisation

The various volume fraction MoSI/PMMA and MWNT/First Contact films were prepared for mechanical characterisation by cutting them into strips 2.25 mm wide using a press die-cutter machine with fixed blades. These strips were used for the tensile testing. The width and thickness of each of the strips was measured using a digital vernier callipers and a digital micrometer screw before each measurement.

3.6.1 Tensile Testing

Tensile testing is a relatively simple and direct method of measuring the mechanical properties of a material, where the force applied is measured as a function of the elongation of the sample. It is also possible to perform the measurements by measuring the strain as a function of the stress. From this analysis, several parameters are derived. In the elastic limit of the material, the stress (force per unit area) is proportional to the strain

(relative elongation) and the slope of this initial linear region is the Young's modulus, Y. Above the elastic limit, this linearity is no longer true, and plastic behaviour is observed where the material becomes permanently deformed. In this region, strain hardening is observed until the maximum stress applied to the sample before it breaks, the ultimate tensile strength, σ_t, is reached. Above this point, rapid failure is observed until the stress at which the sample does break is the "strength to failure". These are shown on a sample stress-strain curve in figure 3.10. The area under the stress-strain curve up to the failure point is equivalent to the energy absorbed per unit volume at fracture and is called the toughness, T. The measurements were performed on a Zwick/Roell Z 2.5 tensile tester.
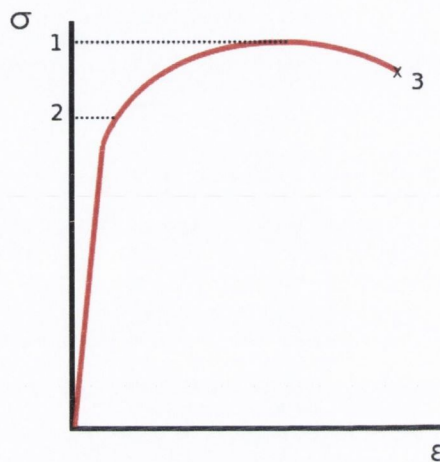
Figure 3.10 – A typical stress-strain curve for aluminium to illustrate the various parameters measured by tensile testing. The ultimate tensile strength (1), yield point (2) and the failure point (3) are marked on the curve. The area under the full curve is the toughness.

3.7 Other Characterisation

The main properties of interest in this work were the mechanical and electrical properties of the nano-materials and their composites. The measurements performed to analyse these have been discussed above, but several further techniques were used to analyse the materials.

3.7.1 *Thermogravimetric Analysis*

Thermogravimetric analysis (TGA) is the measurement of the mass of a substance as a function of temperature. TGA can be performed in a variety of different gas atmospheres to obtain different information. TGA can be used to determine the decomposition temperature of a material, and its decomposition process if several steps are involved. For samples containing multiple components (e.g. nanotubes, polymer and solvent), the mass of each of the components can be calculated using TGA, as long as the

components decompose, or evaporate, at sufficiently different temperatures. This can be used to confirm the composition of the composite films prepared, although for low volume fractions the nanotube/nanowire content may be too small to be measured accurately. A Perkin Elmer Pyris 1 TGA was used for these measurements.

3.7.2 *Dynamic Scanning Calorimetry*

Dynamic scanning calorimetry (DSC) is a technique which measures the heat flow into, or out of, a sample as a function of temperature relative to a reference. The reference allows greater sensitivity as external factors will affect both the sample and the reference equally. DSCs operate by either the power compensation or the heat flux method. Power compensation DSC maintains the sample and reference at the same temperature and the difference in the heat supplied required to achieve this is measured. For heat flux DSC, the temperature of the samples is measured for an equal heat flux to both samples, which is possible as both samples are in the same furnace but with individual thermocouples. For the work presented in this thesis a power compensation Perkin Elmer Diamond DSC was used.

The heat flow through the sample as a function of temperature will vary as any changes in morphology occur, allowing many different parameters to be determined including melting points (T_m) and the glass transition (T_g). At the melting point, T_m, the increase of heat flow due to the latent heat of the transition is observed as an endothermic peak in the heat flow versus temperature plot. At the glass transition, sufficient thermal energy has been supplied for the molecules in an amorphous solid to become mobile. For polymers, this is the temperature at which the kinetic energy of the polymer chains overcomes the non-covalent bonding between polymer chains which is observed as a transition from a hard, stiff material to a softer, rubbery material. The glass transition is observed as a shift in the baseline in DSC and is important due to the dramatic change in material properties that occurs.

3.7.3 *Absorption Spectroscopy*

In absorption spectroscopy, the change in intensity of light as it passes through a sample is measured. This allows the absorbance, A, to be calculated, which is defined by equation 3.12.

$$A = \log_{10}\left(\frac{I_0}{I}\right)$$ Equation 3.12

where I_0 is the incident light intensity, I is the transmitted intensity.

47

This change in intensity is related to the path length, L, and the concentration, c, by the Beer-Lambert law,

$$\frac{I}{I_0} = e^{-\varepsilon cL}$$

Equation 3.13

where ε is the extinction coefficient. In practice, I_0 is the intensity transmitted through a reference cuvette, and I is the intensity transmitted by the sample. The extinction coefficient is a measure of the light absorbed and/or scattered by the material and is frequency dependent.

UV-vis-near IR absorption spectroscopy was used to characterise the $Mo_6S_3I_6$ material and its separated components. A Perkin-Elmer Lambda 9000 spectrometer was used to obtain the spectra using 1 cm cuvettes. Dispersions of each of the components were prepared by sonicating them with the ultrasonic tip in isopropanol. Spectra were taken in the range from 200 nm to 2.3 µm.

For the MWNT/First Contact composite solutions, UV-vis absorption spectroscopy was performed using a Shimadzu UV-2401 PC spectrometer to calculate the amount of nanotubes that had sedimented out before decantation. Spectra were measured from 200 nm to 800 nm for the diluted 0.1 ml samples of the composite solutions taken immediately after sonication, and directly after decantation, using a solution of First Contact as the reference. It was necessary to dilute both solutions, and to use 1 mm cuvettes, to increase the transmission. As the absorbance is proportional to the concentration, the concentration after sedimentation could be calculated from the change in absorbance, relative to the initial concentration. As all the solutions for each batch are made by diluting this solution, the other concentrations can also be calculated.

3.7.4 X-ray Photoelectron Spectroscopy

X-ray Photoelectron Spectroscopy (XPS) uses x-ray photons to ionise core electrons from individual atoms. The kinetic energy of the emitted electrons is measured using an electron energy analyser, and from this the binding energy of the atom that emitted the electron can be calculated.

$$E_{binding} = h\nu - K.E._{electron}$$

Equation 3.14

Dispersions of the $Mo_6S_3I_6$ material, and its separated components, were drop-cast on silicon dioxide substrates and analysed using a Kratos Axis HS and a monochromatic Mg K_α X-ray source (E = 1253.6 eV) were used to measure their X-ray photoelectron spectra. From the analysis of the measured spectra, the ratio of each element present could

be calculated, and hence their stoichiometries determined. These measurements were done by Giuseppe Compagnini in the University of Catania, Italy.

3.7.5 *Transmission Electron Microscopy*

Transmission Electron Microscopy (TEM) is, in principle, similar to optical microscopy. Electrons are produced by thermionic or field emission, which are focused onto a sample using electromagnetic lenses, and the transmitted electrons are focused again onto a CCD to produce the image. Areas that scatter electrons appear dark and areas that transmit appear bright. Very thin samples are required to allow the electrons to penetrate. The wavelength of the electrons (~ 10 pm at 100 keV accelerating voltage) is much lower than that of visible light (~ 500 nm), allowing much higher resolution, but it is still limited by other factors, such as the resolution of the detector and lens aberrations.

For each of the solvents used in the sedimentation studies of the $Mo_6S_3I_6$ washed powder, three TEM samples were prepared on holey carbon TEM grids. Before sedimentation measurements were begun, directly after sonication, a TEM grid of the dispersion in each solvent was prepared by drop-casting a small amount of solution. After the sedimentation measurements were complete, the samples were decanted to separate the sediment from the stable dispersion. A TEM grid of each of these was then prepared. TEM was performed using a Hitachi H-7000.

3.7.6 *Scanning Electron Microscopy*

Scanning Electron Microscopy (SEM) consists of an electron source focused to a fine spot size onto the surface of the sample, and is rastered across the sample using two electromagnetic scanning coils. The intensity of the secondary electrons scattered from the surface is measured by a detector as a function of position, allowing an image of the whole sample to be built up.

Field emission scanning electron microscopy was done using a Hitachi S-4300 on uncoated $Mo_6S_3I_6$ powder samples and on the various composite films. The conductivity of the $Mo_6S_3I_6$ powders was sufficiently high to avoid charging, so gold-coating of the samples was not necessary.

3.8 References

[1]   M. Cadek, R. Murphy, B. McCarthy, A. Drury, B. Lahr, R. C. Barklie, M. in het Panhuis, J. N. Coleman, and W. J. Blau, Carbon 40 (2002) 923.

[2]   A. A. Puretzky, D. B. Geohegan, X. Fan, and S. J. Pennycook, Applied Physics Letters 76 (2000) 182.

[3]   K. Hernadi, A. Fonseca, J. B. Nagy, D. Bernaerts, A. Fudala, and A. A. Lucas, Zeolites 17 (1996) 416.

[4]   Nanocyl S. A. - http://www.nanocyl.com (2007)

[5]   E. Lahiff, R. Leahy, J. N. Coleman, and W. J. Blau, Carbon 44 (2006) 1525.

[6]   I. Willems, Z. Konya, J. F. Colomer, G. Van Tendeloo, N. Nagaraju, A. Fonseca, and J. B. Nagy, Chemical Physics Letters 317 (2000) 71.

[7]   P. Nikolaev, M. J. Bronikowski, R. K. Bradley, F. Rohmund, D. T. Colbert, K. A. Smith, and R. E. Smalley, Chemical Physics Letters 313 (1999) 91.

[8]   Image of CVD apparatus from http://students.chem.tue.nl/ifp03/synthesis.html

[9]   M. L. Terranova, V. Sessa, and M. Rossi, Chemical Vapor Deposition 12 (2006) 315.

[10]   M. Foygel, R. D. Morris, D. Anez, S. French, and V. L. Sobolev, Physical Review B 71 (2005) 104201.

[11]   E. J. Garboczi, K. A. Snyder, J. F. Douglas, and M. F. Thorpe, Physical Review E 52 (1995) 819.

[12]   M. Cadek, J. N. Coleman, K. P. Ryan, V. Nicolosi, G. Bister, A. Fonseca, J. B. Nagy, K. Szostak, F. Beguin, and W. J. Blau, Nano Letters 4 (2004) 353.

[13]   Y. R. Hernandez, A. Gryson, F. M. Blighe, M. Cadek, V. Nicolosi, W. J. Blau, Y. K. Gun'ko, and J. N. Coleman, Submitted to Applied Physics Letters (2006)

[14]   D. Vrbanic, M. Remskar, A. Jesih, A. Mrzel, P. Umek, M. Ponikvar, B. Jancar, A. Meden, B. Novosel, S. Pejovnik, P. Venturini, J. C. Coleman, and D. Mihailovic, Nanotechnology 15 (2004) 635.

[15]   V. Nicolosi, D. Vrbanic, A. Mrzel, J. McCauley, S. O'Flaherty, C. McGuinness, G. Compagnini, D. Mihailovic, W. J. Blau, and J. N. Coleman, Journal of Physical Chemistry B 109 (2005) 7124.

[16]   Mo6 d.o.o., http://www.mo6.com (2007)

[17]   P. W. Atkins and L. L. Jones, Chemistry: molecules, matter and change, W. H. Freeman, 1997.

[18]   B. Bercic, U. Pirnat, P. Kusar, D. Dvorsek, D. Mihailovic, D. Vengust, and B. Podobnik, Applied Physics Letters 88 (2006) 173103.

[19] R. H. Baughman, A. A. Zakhidov, and W. A. de Heer, Science 297 (2002) 787.

[20] J. N. Coleman, U. Khan, W. J. Blau, and Y. K. Gun'ko, Carbon 44 (2006) 1624.

[21] J. K. W. Sandler, J. E. Kirk, I. A. Kinloch, M. S. P. Shaffer, and A. H. Windle, Polymer 44 (2003) 5893.

[22] Photonic Cleaning Technologies - http://www.photoniccleaning.com (2007)

[23] J. M. Bennett and D. Ronnow, Applied Optics 39 (2000) 2737.

[24] D. N. McCarthy, V. Nicolosi, D. Vengust, D. Mihailovic, G. Compagnini, W. J. Blau, and J. N. Coleman, Journal of Applied Physics 101 (2007) 014317.

[25] V. Nicolosi Ph.D. Thesis, in the School of Physics, Trinity College Dublin, Ireland, 2006.

[26] J. R. Macdonald and E. Barsoukov, Impedance Spectroscopy: Theory, Experiment, and Applications. , Wiley, 2005.

CHAPTER 4

Characterisation of MWNT/First Contact Composites

4.1 Introduction

In this chapter the mechanical and electrical properties of a nanotube/polymer composite material are discussed. The polymer material is a novel elastomer designed for cleaning high precision optics [1] which has been used to clean the 10m Keck telescope mirror in Hawaii as well as the Hope diamond in the Smithsonian Institution in Washington D.C., shown in figure 4.1. The interaction of the polymer with nanotubes has been investigated and shown it to disperse nanotubes well, thus overcoming one of the common problems associated with nanotubes and nanotube composites. Therefore, well-dispersed, high aspect ratio nanotubes could be achieved in this polymer, leading to low percolation thresholds and conductive composites with minimal effect on the polymer properties.

The polymer itself has many useful properties as it is non-toxic and inert and also acts as a barrier to oxygen, sulphur and water vapour making it suitable for packaging, as well as its original cleaning application. Here, the mechanical properties of the nanotube composites, as well as the polymer itself, are measured by tensile testing. The electrical properties of the composites are also measured for a range of volume fractions in order to determine the conductivities and thus the percolation threshold.
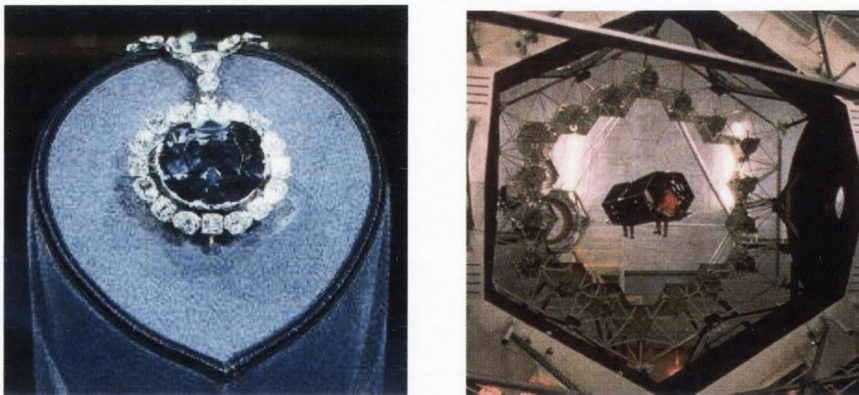
Figure 4.1 – Pictures of the Hope diamond in the Smithsonian Institute, Washington D.C. [2] and of the Keck telescope 10 m main mirror, Hawaii [3].

4.2 Calculation of MWNT Content of Composites

The First Contact polymer is received as a solution from the manufacturer [1], in the same form as it is sold and used commercially. The original concentration of the solution and the solvents is proprietary information, but the solution is diluted for this work to a concentration of 29 g L^{-1} (the polymer mass in solvent volume). This diluted solution is added to a measured mass of carbon nanotubes (MWNTs) to make composite solutions of a known initial concentration. The nanotube content of this solution changes after sedimentation. Also, drying effects during the solvent evaporation to form the films is observed to cause an inhomogeneous distribution of nanotubes in the films. In this section, the methods used to calculate the concentrations of the films after these steps are described.

4.2.1 *UV-vis Spectroscopy*

The concentration of the composite solution used for the dilutions is not known, due to the removal of the MWNTs that had sedimented over the three days settling time by decantation. The sediment was dried, but when removed it was clear that the sediment contained a significant amount of the First Contact polymer as it had formed a solid film. The amount of sediment was negligible compared to the polymer mass in the solution (~260 mg), but as the initial amount of MWNTs was 22.6 mg, it does affect the MWNT content of the composite.
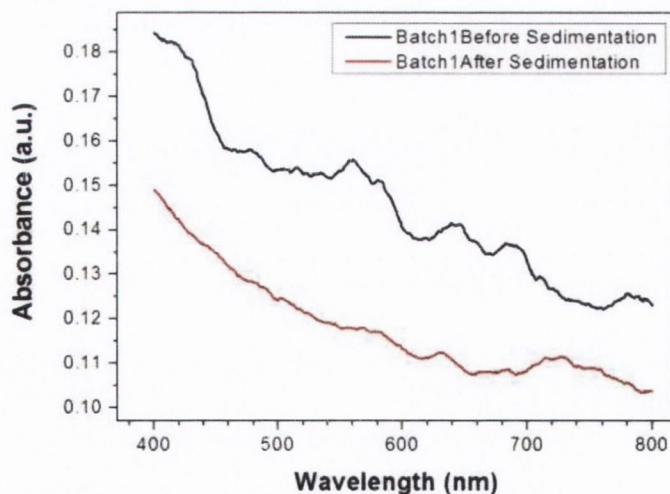
Figure 4.2 – UV-vis spectra of diluted solutions of the first batch of MWNT and First Contact composite before sedimentation (red) and after sedimentation (black).

UV-vis spectroscopy was used to monitor the change in MWNT concentration before and after sedimentation. As the First Contact polymer solution is transparent in the visible region, the main contribution to any decrease in the transmission is assumed to be

due to the nanotubes. A pure First Contact polymer solution was used as the reference ensuring any decrease due to the polymer contribution is taken into account. The spectra measured for the solutions before and after sedimentation are shown in figure 4.2. In the absorption spectra it can be seen that the absorption approximately decreases with increasing wavelength for both the spectrum before sedimentation and after sedimentation. Before sedimentation some distinct peaks are visible in the spectrum, but these appear to be quenched in the spectrum after sedimentation. It is possible that these peaks are due to the van Hove singularities of the various nanotubes present in the dispersion. After standing for three days, some reaggregation may have occurred which would lead to the quenching observed. From the change in absorbance at several wavelengths the average decrease in concentration of MWNTs in the solution, c_{NT}, was calculated to be from 2.51 g L^{-1} before sedimentation, to 2.05 g L^{-1} after sedimentation. Assuming a negligible sedimentation of the polymer, its concentration, $c_{polymer}$, will remain at 29 g L^{-1}. Therefore, the volume fraction of MWNTs in polymer was calculated to be 0.027 using equation 4.1, and the known densities of the polymer and nanotubes. From this value, the volume fractions of all of the subsequent dilutions prepared from this composite solution could also be calculated.

$$\phi = \frac{c_{NT}/\rho_{NT}}{c_{NT}/\rho_{NT} + c_{polymer}/\rho_{polymer}}$$

Equation 4.1
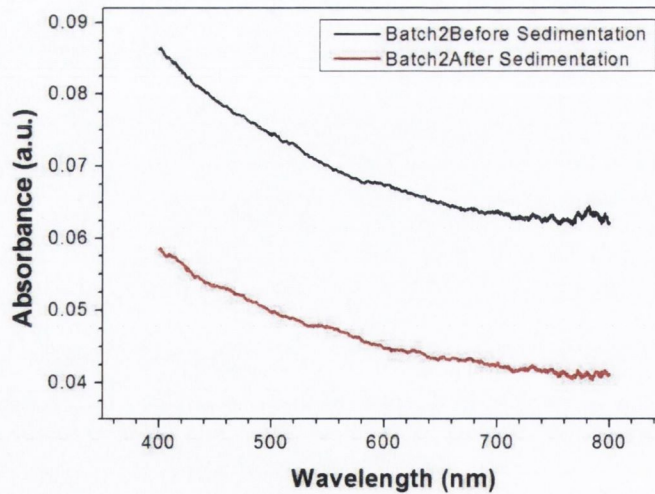
Figure 4.3– UV-vis spectra of diluted solutions of the second batch of diluted solutions of MWNT and First Contact composite before sedimentation (red) and after sedimentation (black).

As discussed later in section 4.3, when the conductivities of the Batch 1 samples were measured and plotted against volume fraction, ϕ, it was observed that even the lowest volume fraction composite sample, 8.5×10^{-4}, was well above the percolation threshold. At

this nanotube volume fraction, the conductivity has saturates and this a percolation fit is not possible. A second batch of MWNT/First Contact was prepared with an initial volume fraction of 7.7 ×10^{-3}. As for the first batch, UV-vis spectra were measured before and after decantation, allowing the volume fraction after to be calculated. These spectra are shown in figure 4.3, and the absorbance observed is considerably less than for the previous composite solutions. From these spectra, the volume fraction of the composite solution after decantation was calculated as $\phi = 5.2 \times 10^{-3}$, and thus the volume fractions of the other diluted composite solutions could be calculated.

4.2.2 Thermogravimetric Measurement

From the range of diluted solutions, films were drop-cast in glass petri dishes. Upon drying it was observed that some of the MWNTs in the higher concentration films had formed aggregates, and also a region with a higher concentration of MWNTs had formed at the edges. This "coffee stain" drying effect has been reported before [4, 5], where it was observed to be due to a pinned contact line, meaning the edge of the droplet cannot retreat as it evaporates. This results in a capillary flow of fluid from the centre to the edge as evaporation continues, causing in an increase in the concentration of nanotubes at the edge, as is visible in figure 4.4. In order to ensure the samples measured were relatively homogeneous, they were only cut from the central region, avoiding the outer ~5 mm annulus. Also visible in the high volume fraction films are large aggregates of nanotubes. Aggregation of the nanotubes could be caused by the depletion interaction, which would lead to a positive attraction between nanotubes and hence encourage aggregation. These aggregates are not visible at lower volume fractions, but they may be present as smaller aggregates not visible by eye.

Figure 4.4 – Photograph of MWNT/First Contact films dried in petri dishes. The darker regions at the edges are due to drying effects, which cause a higher MWNT concentration at the edges. The films shown are ~49 mm in diameter.

55

The uneven distribution of the MWNTs in the dried films reintroduces uncertainty into the composition of the films. Thermogravimetric analysis (TGA) of the polymer and MWNTs individually, and the composite films were performed in order to calculate the masses of the individual components. As can be seen in figure 4.5, the majority of the First Contact polymer had decomposed before the MWNTs began to decompose. This suggests that it should be possible to distinguish the nanotube component from the polymer component, and calculate the mass of each present. Thus, the volume fraction of the MWNTs in the centre of composite films can be calculated for comparison with the previous UV-vis spectroscopy results.
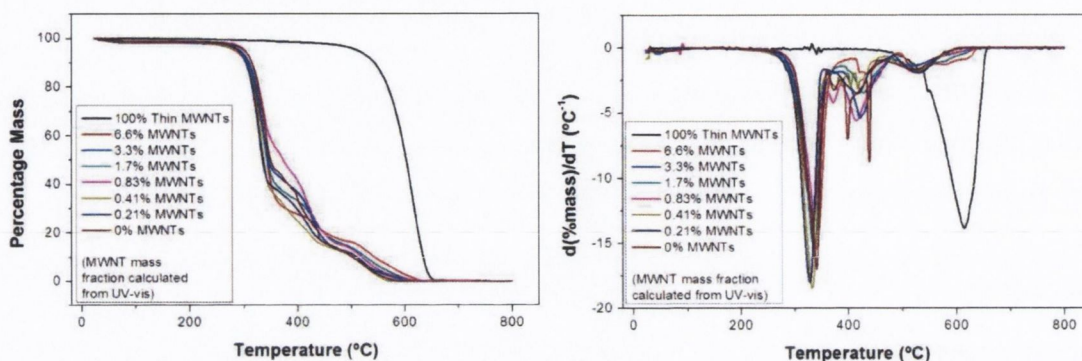
Figure 4.5 – TGAs of the raw materials, Thin MWNT powder and First Contact polymer film, and of the various composite films prepared are shown on the left. The derivatives of these curves are shown on the right. The mass fractions, m_f, are calculated from the UV-vis spectroscopy previously described.

From the derivative of the TGA curves, shown on the right above, it is clear the First Contact polymer overlaps with the beginning of the MWNT decomposition peak. In the composite derivative curves, especially the 6.6% and 1.7%, the MWNT component is visible as an extension of the final polymer peak at approximately 530 °C. This overlap makes the calculation of the MWNT mass more difficult, as the positions of the peaks vary between TGAs and therefore the direct subtraction of the 100% polymer sample from the composites is not possible.
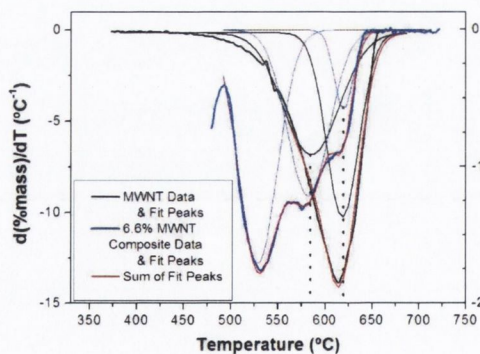
Figure 4.6 – Example of deconvolution used to calculate the MWNT peak areas from the TGAs. The MWNT peak can be deconvoluted to two peaks at approximately 585 °C and 620 °C. The final peak in the 6.6% composite TGA can be deconvoluted to three peaks, at approximately 530 °C, 580 °C and 620 °C. The positions of the two MWNT peaks and the corresponding peaks in the composite are marked by the vertical dotted black lines.

56

As stated above, the polymer itself was observed to have its final decomposition peak at approximately 530 °C. It was found that the MWNT peak could be deconvoluted into two peaks, at 585 °C and 620 °C respectively, as shown by the black peaks in figure 4.6. For the composites, the final decomposition peak of the polymer merges with the MWNT peaks, but it was found that these three peaks could be deconvoluted for the high mass fraction samples. However, below 0.83%, the MWNT content is so small that the difference between the polymer curve and the composites becomes negligible. The total First Contact polymer and MWNT area was measured by integrating from 100 °C to 800 °C. From TGA, there is almost no solvent observed in the films, with a decrease of less than 2% by mass within the first 100 °C. Only the area after this region was integrated to avoid measuring the solvent contribution. The deconvoluted individual peak areas and this total area are shown in table 4.1 below. For each sample, the sum of the area of the two peaks at ~585 °C and 620°C, divided by the total area is the mass fraction, m_f, of nanotubes, and this is also listed in table 4.1.

m_f (UV-vis)	Areas of Deconvoluted Peaks at:			Total Area (100 – 800 °C)	m_f (TGA)
	~530 °C	~585 °C	~620 °C		
MWNTs	-	49.6%	43.8%	98.5%	94.8%
6.6%	8.8%	6.7%	1.5%	100.8%	8.1%
3.3%	10.9%	3.2%	0.3%	100.2%	3.5%
1.7%	14.8%	1.0%	1.7%	100.4%	2.7%
0.83%	11.4%	3.9%	-	99.6%	3.9%

Table 4.1 – Results from deconvolution of TGAs, the total area of the whole curve from integration, and the mass fraction, m_f, of MWNTs calculated from the results. Also listed are the mass fractions, m_f, of the composite solutions as calculated from the UV-vis previously.

For the MWNTs, there were only two peaks as the peak at ~530 °C is due to the First Contact polymer. For the 0.83% sample, the peak at ~620 °C was negligible and only two peaks could be fitted to the data. Thus, this data can only give an estimate of the nanotube content as the data is quite noisy. The area of the ~530 °C peak is relatively consistent, except for the 1.7% sample, indicating very little change in the amount of polymer between different mass fractions, as would be expected. The values calculated are quite similar to the mass fractions as calculated from the UV-vis spectroscopy, demonstrating that the drying effects have caused only a minimal change in the MWNT concentration in the centre of the film. Therefore, the spectroscopy values are shown to be consistent and reliable, and these were used for all further analyses for both the Batch 1 and Batch 2 composite samples.

4.3 Electrical results – DC & AC

4.3.1 _Batch 1 of First Contact/MWNT composites_

For each volume fraction film prepared, the six finger electrodes allowed six different regions to be tested. Several current-voltage (I-V) measurements over different voltage ranges were performed for each of the electrodes for every composite volume fraction, ϕ, prepared and for the polymer alone. Examples of the I-V characteristics measured are shown in figure 4.7.
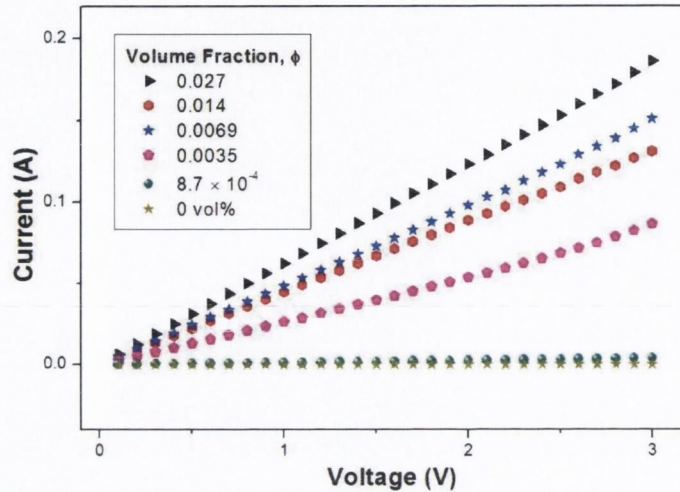
Figure 4.7 – Example I-V curves from the various Batch 1 volume fractions.

For the majority of measurements ohmic I-V relationships was observed, with some saturating when they reached currents greater than the set tolerance of the sourcemeter. For some of the I-Vs, a sudden change in slope (conductance), normally an increase, was observed when a larger voltage range was used. In the high volume fraction films, only a slight increase (less than an order of magnitude) in the I-V characteristic slope was seen as the applied voltage increased, but for the lower volume fraction films the increase was slightly larger (up to 2 orders of magnitude). These variations represent some undetermined conduction mechanism, but they are relatively small compared to the overall increase in conductance with volume fraction, from a minimum of $\sim 10^{-10}$ S to a maximum of $\sim 10^{-1}$ S, and are comparable to the variation between different electrodes for the same volume fraction. For the two lowest composite volume fractions, $\phi = 3.5 \times 10^{-3}$ and 8.7×10^{-4}, the I-V curves for the majority of the electrodes are linear, but some non-linear curves with a conductance significantly lower (approximately 3 - 4 orders of magnitude) than the other electrodes were observed. For each volume fraction, an average conductance value was measured, from which the conductivities were calculated and these are listed in table 4.1.

58

MWNT Volume Fraction, ϕ	D.C. Conductivity, σ_{DC} (S m^{-1})
0.027	0.57 ± 0.51
0.014	0.61 ± 0.43
0.0069	0.52 ± 0.31
0.0035	0.24 ± 0.31
8.7×10^{-4}	0.36 ± 0.36
0	$(1.8 \pm 0.1) \times 10^{-9}$

Table 4.2 – List of the calculated D.C. conductivities for the Batch 1 films. Within error, the conductivity of the composites does not vary.

The calculated D.C. conductivities are plotted in figure 4.8. In the range of volume fractions prepared, the conductivity varies little, indicating these samples are well above the percolation threshold, ϕ_c, at a point where the conductivity has begun to saturate as a function of volume fraction. This would suggest that the maximum conductivity that can be achieved with these composites is ~1 S m^{-1}. Far from the percolation threshold, where $|\phi - \phi_c| \sim 1$, the percolation law, $\sigma = \sigma_0(\phi - \phi_c)^t$, does not hold and the percolation threshold cannot be determined. This was unexpected as previous measurements of the percolation threshold with these thin MWNT yielded a percolation threshold of 4×10^{-3} [6], almost an order of magnitude above the lowest volume fraction prepared here. Also, from the theory of Garboczi et al. [7] the percolation threshold for high aspect ratio prolate ellipsoids is predicted to be $\phi_c = 8 \times 10^{-3}$, calculated from the average aspect ratio of the nanotubes, which has been measured as ~80 [6]. At high aspect ratios prolate ellipsoids will closely approximate cylinders. To determine the percolation threshold, it was therefore necessary to prepare a range of composites with lower volume fractions. From the tensile testing data of the first range of volume fractions, described in section 4.4.1, it was clear that mechanical measurements of these lower volume fractions would yield little information, so only electrical testing was performed, as is described in the following section 4.3.2.
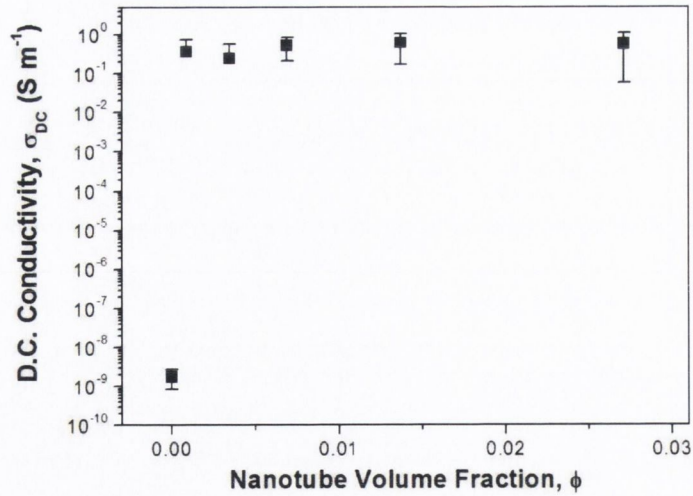
Figure 4.8 – The measured D.C. conductivities of Batch 1 of the First Contact/MWNT composites plotted as a function of nanotube volume fraction, ϕ.

4.3.2 Batch 2 of First Contact/MWNT composites

From Batch 1 of the First Contact/MWNT composites, it was ascertained that the percolation threshold is below a volume fraction of 8.7×10^{-4}. For this second batch of composites, the range of volume fractions prepared was from 5.2×10^{-3} to 5.4×10^{-6}, which was three orders of magnitude below the theoretical and experimental percolation thresholds mentioned.
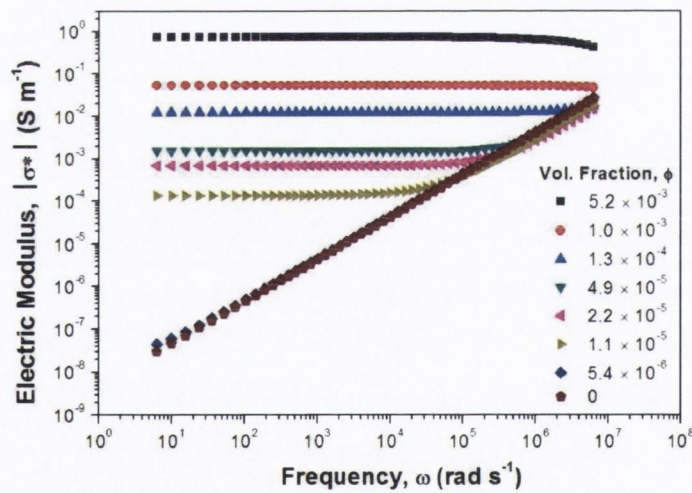
Figure 4.9 - The electric modulus, $|\sigma*|$, plotted as a function of angular frequency, ω, for composites of the First Contact polymer with thin MWNTs for a range of volume fractions, ϕ.

The impedance, $Z^*=Z' - iZ''$, of each of the volume fractions, ϕ, was measured for each of the electrodes over a frequency range from 1 MHz to 1 Hz. The measurements from the electrodes were averaged and converted to the electric modulus, $|\sigma^*(\omega)|$, a similar quantity to the D.C. conductivity and these are plotted in figure 4.9. For the polymer itself, the electric modulus is frequency dependent across the full frequency range, indicating

60

dielectric behaviour. The lowest volume fraction composite, $\phi = 5.4 \times 10^{-6}$, also exhibits dielectric behaviour, indicating that it is below the percolation threshold. For a pure dielectric, the slope of this curve should be 1, as is observed here for both of these volume fractions. From these graphs the transition from completely dielectric (σ^* is frequency dependent over the entire frequency range) to partially conductive (σ^* becomes frequency independent at lower frequencies) can be observed between $\phi = 5.4 \times 10^{-6}$ and 1.1×10^{-5}. This transition indicates the approximate region where the percolation threshold, ϕ_c, is expected to be found. In the limit as frequency goes to zero, $\omega \to 0$, the electric modulus, σ^*, should become equivalent to the D.C. conductivity, σ_{DC}. Here, the lowest frequency measured is 1 Hz and the electric modulus at this frequency is taken as the A.C. conductivity, $\sigma_{AC(\omega \to 0)}$, which are listed below in table 4.3. Above $\phi = 5.4 \times 10^{-6}$, $\sigma_{AC(\omega \to 0)}$ of the composites increases rapidly and reaches a maximum of $\sigma_{AC(\omega \to 0)} \sim 0.7$ S m^{-1} at $\phi = 5.2 \times 10^{-3}$.

After the impedance spectroscopy measurements, similar D.C. I-V curves were measured as for Batch 1. For the three highest ($\phi \geq 1.3 \times 10^{-4}$) and two lowest ($\phi \leq 5.4 \times 10^{-6}$) volume fractions, the I-V curves are linear about 0 V, although some became slightly non-linear at higher voltages (above ~1 V). For the next highest volume fraction, $\phi = 4.9 \times 10^{-5}$, the non-linearity at high voltages was more pronounced, but all of these curves were symmetrical about 0 V. For the two lowest volume fractions that are expected to be above percolation (as indicated by the impedance spectroscopy), $\phi = 2.2 \times 10^{-5}$ and 1.1×10^{-5}, the I-V curves were generally noisy and inconsistent making the measurement of a reliable conductance value difficult. Two more squares were cut from the same film for each of these volume fractions and the electrical measurements were repeated. The results from each of the three samples were then compared to arrive at a more consistent and reliable conductance value for each of these volume fractions.

As with the high volume fractions of Batch 1, some variation in the I-V slopes was observed for all of the Batch 2 samples over the several measurements performed. The conductivities reported are calculated from the averages of all of these conductances. At voltages above 3 V a sudden decrease in the slope of the I-V, and hence the conductance of the composite, was often observed. This appears to be due to the percolating network becoming damaged from high currents. Similar results were observed by Murphy [8] for MWNT/PVP composites, and the decrease there was attributed to the electrical breakdown of metallic MWNTs which has previously been performed deliberately [9]. It is possible that similar damage is occurring within the percolation network in the First Contact

composite films. The effect is more common at the lower volume fractions, closer to the percolation threshold, where fewer current pathways should exist and thus will carry the majority of the current. The resultant higher current densities would be more likely to cause damage to this backbone of nanotubes in the network. For sudden, large decreases in conductance ($> 10^3$ S), the values after the decrease were assumed to be from a damaged network and were neglected from the overall conductance calculation. The calculated D.C. conductivities, σ_{DC}, are listed below with the electric moduli, $\sigma_{AC(\omega \to 0)}$, in table 4.3

MWNT Volume Fraction, ϕ	Zero field D.C. Conductivity, σ_{DC} (S m^{-1})	Zero frequency limit A.C. Conductivity, $\sigma_{AC(\omega \to 0)}$(S m^{-1})
5.2×10^{-3}	0.86 ± 0.23	$0.74 \pm 2 \times 10^{-4}$
1.0×10^{-3}	0.17 ± 0.13	$0.05 \pm 3 \times 10^{-5}$
1.3×10^{-4}	0.20 ± 0.20	$0.01 \pm 4 \times 10^{-6}$
4.9×10^{-4}	0.07 ± 0.17	$(1.53 \pm 0.002) \times 10^{-3}$
2.2×10^{-5}	$(8.6 \pm 15.1) \times 10^{-4}$	$(6.70 \pm 0.006) \times 10^{-4}$
1.0×10^{-5}	$(0.01 \pm 1.6) \times 10^{-3}$	$(1.35 \pm 0.003) \times 10^{-4}$
5.4×10^{-6}	$(1.41 \pm 0.5) \times 10^{-8}$	-
0	$(3.32 \pm 1.1) \times 10^{-9}$	-

Table 4.3 – Calculated D.C. and A.C. conductivities for the Batch 2 films. Below $\phi = 10^{-5}$, no $\sigma_{AC(\omega \to 0)}$ values are stated as the electric modulus is always frequency dependent.

The D.C. conductivity of the composites is observed to reach a value 10^8 times greater than the polymer conductivity at the very low volume fraction of 1.3×10^{-4}. The lowest volume fraction composite, $\phi = 5.4 \times 10^{-6}$, also shows a slight increase in conductivity, indicating that it is quite close to the percolation threshold. As seen here, and was clear from the Batch 1 results, by $\phi = 5.2 \times 10^{-3}$ the conductivity reaches a maximum value of ~1 S m^{-1}. This is still extremely large for the low volume fraction of nanotubes present in the film. The linear fits to the percolation law, $\sigma = \sigma_0(\phi - \phi_c)^t$, for D.C. conductivities, σ_{DC}, of this system were calculated for a range of values of ϕ_c in the region where ϕ_c was expected to be found, from 5×10^{-7} to 2.0×10^{-7}. The best fit was found to be for $\phi_c = (5.0 \pm 0.5) \times 10^{-6}$ and this is shown plotted in figure 4.10. In figure 4.11 all of the conductivities measured, for Batch 1 and 2, are shown with the percolation fit.
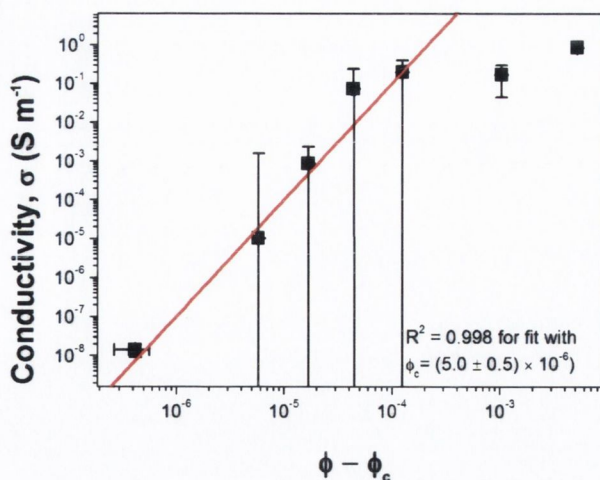
Figure 4.10 – Plot of the D.C. conductivities of Batch 2 against (ϕ - ϕ_c). The red line is the calculated fit to the percolation law, $\sigma = \sigma_0(\phi - \phi_c)^t$.

Although high aspect ratio filler materials are expected to reduce the percolation threshold, the value calculated here is significantly lower than values previously measured for these nanotubes or predicted from theory, both $\sim 10^{-3}$, as mentioned above in section 4.3.1. The reason for this is not completely clear, although Vigolo et al. demonstrated that an attractive potential between nanotubes can reduce the percolation threshold of the system [10]. In their work, they showed that larger clusters of nanotubes formed as the attractive potential increased, allowing a percolation network to form. A decrease in the percolation threshold by a factor of 3 was measured for an increase in the nanotube adhesion energy of $0.006kT$. They used a surfactant dispersion of nanotubes for their study which limited the range of volume fractions they were able to measure. For the MWNT/First Contact system it is possible that a greater attractive force was induced by the polymer, leading to a larger decrease in the percolation threshold, but it is unlikely that this would be solely responsible for a decrease by 10^3. McLachlan et al. [11] have suggested various reasons for the deviations between experimental and theoretical percolation thresholds, including simplified bundle structures and the inflexible sticks used in the models.
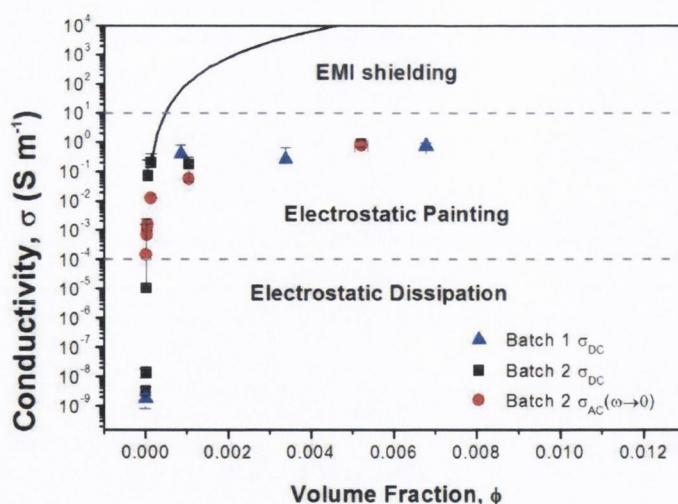
Figure 4.11 – Plot of the conductivities measured for the MWNT/First Contact composites against volume fraction. The D.C. conductivities of Batch 1 and 2, the zero frequency limit A.C. conductivities measured for Batch 2, and the percolation fit (black line) are shown. Dashed lines represent the approximate conductivity lower bound required for some electrical applications [12].

Compared to previously reported percolation thresholds, the result here is the lowest yet measured. Prior to this, the lowest values were 1.3×10^{-5} for $Mo_6S_{4.5}I_{4.5}$ in poly(methyl methacrylate) [13] and 2.5×10^{-5} mass fraction ($\sim 10^{-5}$ volume fraction) for aligned CVD-MWNTs in an epoxy [14], which are both extremely low as most percolation thresholds are higher than 10^{-4}. For the composites in those studies, the maximum conductivity measured was $\sim 2 \times 10^{-3}$ S m^{-1} at volume fractions of 0.027 for the $Mo_6S_{4.5}I_{4.5}$ nanowires and ~ 1 S m^{-1} at 1 wt% for aligned CVD-MWNTs. Here, for the MWNT/First Contact composites, the maximum measured conductivity was 0.8 S m^{-1}, far above the nanowires and equivalent to the nanotubes, but at the much lower volume fraction of 5.2×10^{-3}. To put it in context, this conductivity is significantly higher than silicon, $\sigma \sim 10^{-4}$ S m^{-1} and almost equivalent to germanium, $\sigma \sim 1$ S m^{-1} [15]. At concentrations low enough for the MWNT/First Contact films to be transparent, $\phi = 1.3 \times 10^{-4}$, conductivities as high as 0.20 S m^{-1} were achieved, far above the conductivity required for electrostatic dissipation, above the value required for electrostatic painting, 10^{-4} S m^{-1}, and close to the level required for EMI shielding, 1 S m^{-1} [12]. Nanotube composite films have been prepared with much higher conductivities, between 100 and 2000 S m^{-1}, but only with significantly higher nanotube contents, 10 wt% or greater [16-18]. Although, here the conductivities attained are 100 times lower than these, they are achieved at a volume fraction $\sim 10^6$ times lower.

Percolation threshold, ϕ_c	Conductivity prefactor, σ_0 (S m^{-1})	Critical exponent, t
$(5.0 \pm 0.5) \times 10^{-6}$	$(1.3 \pm 22) \times 10^{11}$	2.97 ± 0.27

Table 4.4 – Table of the parameters calculated from the percolation fit for the Batch 2 D.C. conductivity data.

The conductivity prefactor, $\sigma_0 = (1.3 \pm 22) \times 10^{11}$ S m^{-1} and the critical exponent, $t = 2.97 \pm 0.27$ can also be extracted from the percolation fit. The σ_0 parameter is an extrapolation of the percolation law to 100% filler material, but is not equivalent to the intrinsic conductivity of the filler material which was previously measured to be ~2 S m^{-1} for the powder and ~500 S m^{-1} for buckypaper films of the nanotubes [6]. Here, the σ_0 value is extremely high compared to previous reports and significantly higher than the conductivity measured for the nanotubes themselves. Kilbride et al. calculated a σ_0 of ~10^{-3} S m^{-1} [19] and their low value was attributed to crystallisation of the polymer around the nanotubes, causing an increase in the inter-nanotube distance, hence reducing the overall conductivity of the system as the tunnelling barriers are increased. An attractive potential between the nanotubes, as suggested above, can lead to much smaller inter-nanotube distances. The good dispersion of the nanotubes in this polymer could also lead to the nanotubes being in closer proximity to each other, reducing the tunnelling barriers and increasing the number of current pathways and hence increasing the bulk conductivity of the MWNT/First Contact composite system. The difference between σ_0 and the conductivity of the nanotubes alone, stated above, is quite large, but the percolation law is only valid in the range $|\phi - \phi_c| \ll 1$ and the σ_0 value is actually an overestimate. The large value does indicate the minimal effect of the polymer on the conductivity of the nanotube network.

The critical exponent, t, was measured to be 2.97 ± 0.27. The universal value for a three dimensional system has been stated as 1.65 [20] or more recently it is commonly stated as 2.0 [11, 21, 22]. The critical exponent is only truly universal for low aspect ratio fillers when there are no tunnelling barriers. The "universal" value of the critical exponent has been predicted to vary, with values both less than 2.0 [23] and greater than 2.0 predicted [11, 22, 24]. Foygel et al. predict that the critical exponent will decrease as the aspect ratio of the filler particles increases, as shown in figure 2.10. Independent of this effect, the critical exponent is predicted to increase above 2.0 as the distribution of tunnelling barriers in the system increases. The tunnelling barriers are effectively dependent on the polymer coating thickness around the nanotubes and hence the variation

65

in this thickness in the system will lead to a higher critical exponent, with t of 6 and higher having been observed [11, 22, 24].
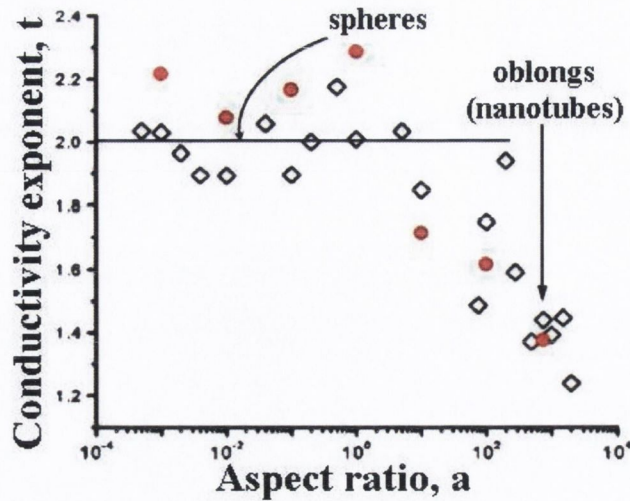
Figure 4.12 – Prediction of the variation of the critical exponent, t, as a function of aspect ratio taken from Foygel et al. [23].

Here, the t value measured is above the "universal" value of 2.0. The average aspect ratio of the nanotubes is approximately 80, which, from Foygel et al., would predict a critical exponent of approximately 1.8. The effect of the range of thicknesses of polymer coatings is expected to increase the critical exponent. In the study by McLachlan et al. [11], the average aspect ratio of the HiPCO nanotubes used was 2500 (Foygel predicts a t of ~ 1.2), but the calculated critical exponent was ~2.2, higher than the universal value. Their low exponent was attributed to uniform dispersion and good wetting of the polymer onto the nanotubes, leading to uniform polymer coating thicknesses. The lower average aspect ratio of the nanotubes used in the study presented here would imply that the First Contact coating is also very uniform and thin, as the combination of the effect of the coatings and the aspect ratio do not cause the exponent to vary greatly from the "universal" value. The high σ_0 calculated for the system would suggest that the inter-nanotube barriers are very small, as the conductivity of the bulk composite is quite high relative to the conductivity measured for the nanotubes themselves.

The various parameters measured from the percolation fit, the extremely low percolation threshold, ϕ_c, and the critical exponent very close to the "universal" value of 2.0, all indicate that the First Contact polymer is dispersing the nanotubes well, as bundles would increase the inhomogeneity and the percolation threshold by decreasing the effective aspect ratio of the nanotubes. It also indicates the polymer is having little effect on the inter-nanotube conductivity as there appears to be almost negligible conduction

barriers between the nanotubes. This is also confirmed by the high conductivity values, ~1 S m^{-1}, measured for the composites at very low volume fractions of nanotubes.

4.4 Mechanical Measurements

4.4.1 *Tensile Testing*

Three strips were analysed by tensile testing for each volume fraction with, on average, a width of 2.25 mm and thicknesses ranging from approximately 30 μm, for low mass fractions, up to 80 μm for the highest mass fractions. For the $\phi = 0.027$ and 0.014 samples it was not possible to analyse all three curves due to flaws or voids in the films causing almost immediate failure of the films. As the First Contact polymer is an elastomer, it can attain high strain before breaking, and for this reason, a high extension rate of 4 mm/min was chosen for the measurements. This did result in an increase in noise in the curves, which are shown in figure 4.13.
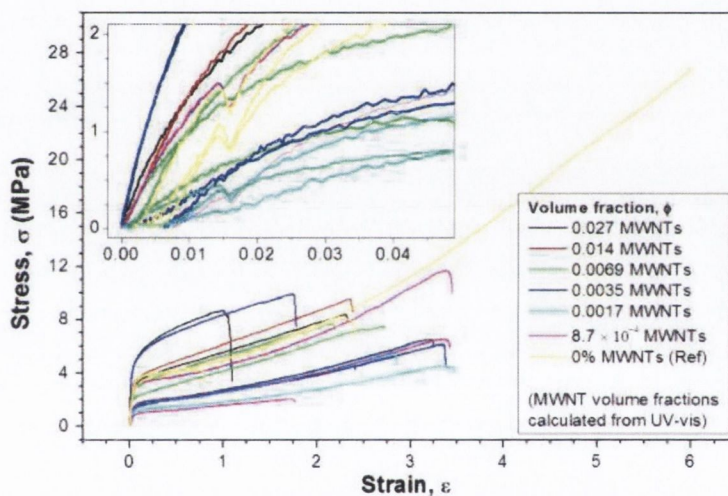
Figure 4.13 – Stress-Strain curves for the various MWNT/First Contact mass fractions. The inset shows the initial elastic regions of the curves, which were used to calculate the Young's moduli. The noise in these curves is due to the high extension rate used.

For all samples, except one reference sample, the strain at break, ε_B, achieved were between approximately 100% and 400%. The exception was a strain at break of almost 600% before failure. For all samples, an initial linear elastic behaviour was observed (shown in the inset of figure 4.13) followed by a plastic deformation above strains of approximately 3%. The Young's modulus of each sample was calculated by measuring the slope in the elastic region, generally below a strain of 2%. In the inset, a discontinuity can be seen in the stress-strain curves of the $\phi = 0$, 8.7×10^{-4} and one of the 1.7×10^{-2} samples at a strain of approximately 1.6%. The cause of this is not clear, nor is the reason why it is only observed in the low mass fraction samples. The maximum stress reached (ultimate tensile strength), σ_T, and the stress at the point of failure (strength-to-failure), σ_B, were

67

measured from these curves. The total area under the curves, the toughness, was also calculated which is a measure of the energy required to break the samples. From the stress-strain curves it is clearly observed that the addition of a small amount of nanotubes, below $\phi = 6.9 \times 10^{-3}$, actually reduces the mechanical properties of the polymer. At $\phi = 6.9 \times 10^{-3}$ the properties have become comparable to the polymer again, and above this concentration they can be seen to increase. The changes in the mechanical properties with nanotube content are more clearly shown in figure 4.14, and later in figure 4.15.
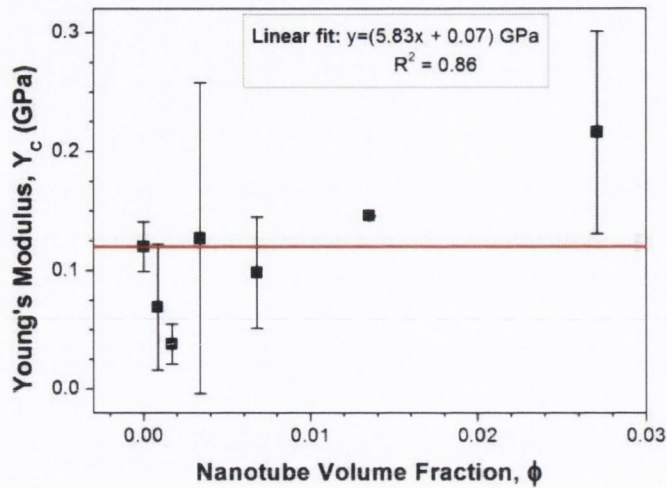
Figure 4.14 – Plot of calculated Young's modulus against volume fraction of MWNTs. Mean and Standard deviation of the Young's modulus for all of the samples of each volume fraction are represented by the data points and error bars, respectively.

In figure 4.14 the average measured Young's modulus, Y, of the composites is plotted with the standard deviation as the corresponding error. From this plot, it can be seen that the polymer has a Young's modulus of approximately 120 ± 20 MPa. The addition of the thin MWNTs, as was observed in the stress-strain curves, causes a gradual decrease in the average Young's modulus to ~40 MPa for a volume fraction of 0.0069. Above this volume fraction, the average Young's modulus returns to the polymer value and then slowly increases, reaching a maximum of 210 ± 85 MPa for the $\phi = 0.014$ sample. Although the average Young's modulus increases, after the initial decrease, with increasing volume fraction, overall the error is too large to be able to state this definitively. Within error, it can be determined that the Young's modulus does not change significantly, demonstrating that the presence of the nanotubes has no negative effects on the mechanical properties of the polymer system.

The other mechanical parameters measured, tensile strength, toughness, breaking strength and strain at break, are shown in figure 4.15. The addition of the nanotubes to this elastomer has somewhat reduced these other properties. The toughness and breaking strength, ε_B, are reduced by the presence of nanotubes by factors of approximately 3 and 2,

respectively. At low volume fractions, the strain-at-break, ε_B, does not change greatly, but above $\phi = 0.0069$ it declines more rapidly. The opposite is true for the tensile strength, which decreases by half for the lowest volume fraction of nanotubes, but then slowly increases, to approximately 75% of the polymer value, with increasing nanotube content.
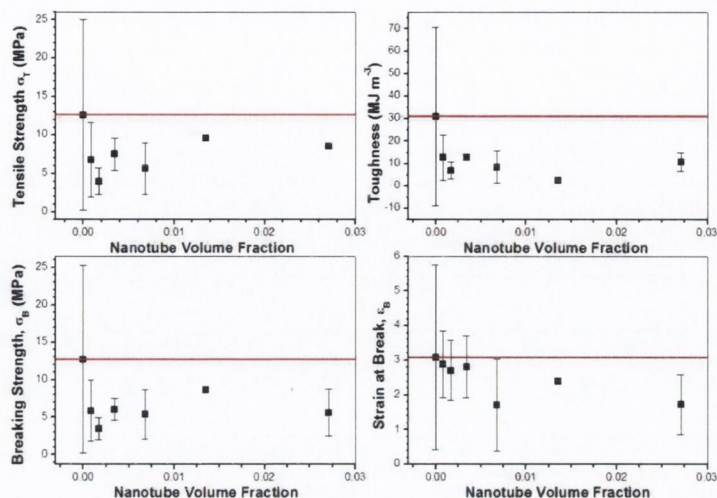
Figure 4.15 – Plots of measured tensile strength, σ_T, toughness, breaking strength, σ_B, and strain at break, ε_B, against volume fraction of MWNTs. All of these values were measured from the stress-strain curves shown in figure 4.13. The red lines indicate the measured value for the polymer.

Most of the work previously reported on nanotube reinforcement has focused on hard thermoplastics rather than elastomers, as an increase in stiffness is generally not a desired improvement in the properties of an elastomer. Several groups have published work on reinforcing polyurethane with MWNTs [17, 25, 26] and one group has reported conduction and reinforcement of a latex [27]. For the polyurethane work, the Young's moduli of the elastomers themselves was approximately 10 MPa, and the maximum modulus of a composite reported was approximately 165 MPa [17]. For the latex, an increase in Young's modulus from 0.52 MPa for the polymer, to 3.54 MPa for a 15 wt% composite was observed. For at least two of the polyurethanes and the latex, the glass transition temperature, T_g, of the polymers was below room temperature. Above T_g the polymer's stiffness is greatly reduced, as the polymer chains have sufficient thermal energy to become independently mobile and the polymer becomes soft and rubbery. Therefore direct comparison of the composites is not possible, but they have demonstrated that reinforcement is possible. In contrast, even the lower values reported for the Young's moduli of hard plastics are ten times higher than the values for the elastomer measured in this work [28].

For all of these examples of elastomer reinforcement, some of the elastomer properties were affected by the presence of the nanotubes. Similar to the First Contact polymer, Koerner et al. [17] observed an initial decrease in the tensile strength, σ_T, and

strain-to-break, ε_B, for low nanotube content, which was reversed at higher nanotube content. Xiong et al. [26] observed a slight increase in σ_T of approximately 10%, but accompanied by a decrease in ε_B of approximately 10%. Chen and colleagues [25] observed an increase in σ_T, ε_B and toughness up to 9.3 wt%, but above this the σ_T and ε_B decreased quite dramatically to below the polymer only values. They attribute the improvements in their composites to strong interfacial bonding between the polymer and functional groups introduced onto the nanotubes by oxidisation, as well as some soft-segment crystallisation of the polymer induced by the nanotubes. In the latex work, the tensile strength and toughness were reduced by the addition of MWNTs. Up to 3 wt% of nanotubes were added without any reduction in the strain-to-break, one of the desirable properties of elastomers, but above this mass fraction it decreased by approximately 25%. Overall, the mechanical properties of the First Contact elastomer are not significantly changed by the introduction of the nanotubes.

4.4.2 Dynamic Scanning Calorimetry

Crystallinity induced by carbon fillers has been observed in other composites films [29, 30] and has been identified as the source of reinforcement. To investigate the effect of the MWNTs on the morphology of the polymer and composites dynamic scanning calorimetry (DSC) was performed.
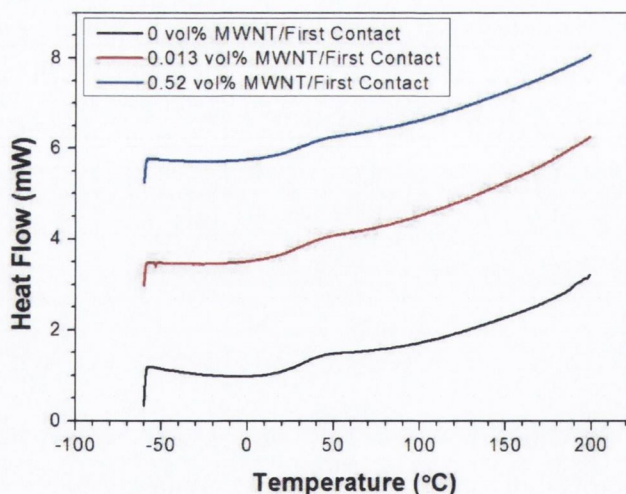
Figure 4.16 – DSC of three of the films from the second Batch of MWNT/First Contact composites prepared. The three films shown are the highest volume fraction of Batch 2, 0.0052, the highest transparent volume fraction, 1.3×10^{-4} and the pure polymer.

The second heat DSC curves in the range from -50 to 200°C for three of the films are shown above in figure 4.16. As can clearly be seen, there are no melting peaks in any of the films, indicating the polymer is amorphous. This lack of crystallisation agrees with the high σ_0 value ($\sim 10^4$ S m^{-1}) calculated from the percolation fit, as described in section

4.3.2. Previously, a low σ_0 value of 1×10^{-3} S m^{-1} was measured for arc-discharge MWNTs in the semi-crystalline polymers polyvinyl alcohol (PVA) and poly(m-phenylenevinylene-co-2,5-dioctyloxyp-phenylenevinylene) (PmPV) [19]. Both of these polymers have been shown to have crystalline coatings due to the presence of the nanotubes [31, 32]. Using the same nanotubes and an amorphous polymer polyvinylpyrrolidone (PVP), a much higher σ_0 of 21 S m^{-1} was subsequently measured [33]. This large difference (~10^4 larger) was assigned to the increased inter-nanotube distance due to the crystalline coatings formed around the nanotubes, which could not form in the amorphous PVP or in the First Contact polymer.

In all three samples, the glass transition temperature, T_g, was observed at approximately 25 °C. This parameter has not previously been measured for this polymer and shows that the polymer is just below the glass transition at room temperature. This transition temperature is important for mechanical measurements, as the properties of the polymer will vary greatly from below the T_g to above it.

4.4.3 *Scanning Electron Microscopy*

Scanning electron microscopy (SEM) was performed on one of the highest volume fraction, $\phi = 0.027$, films which had been fractured by tensile testing and on one of the polymer only films. The surface of the films and the fracture surface were examined for comparison between the composite and the polymer.
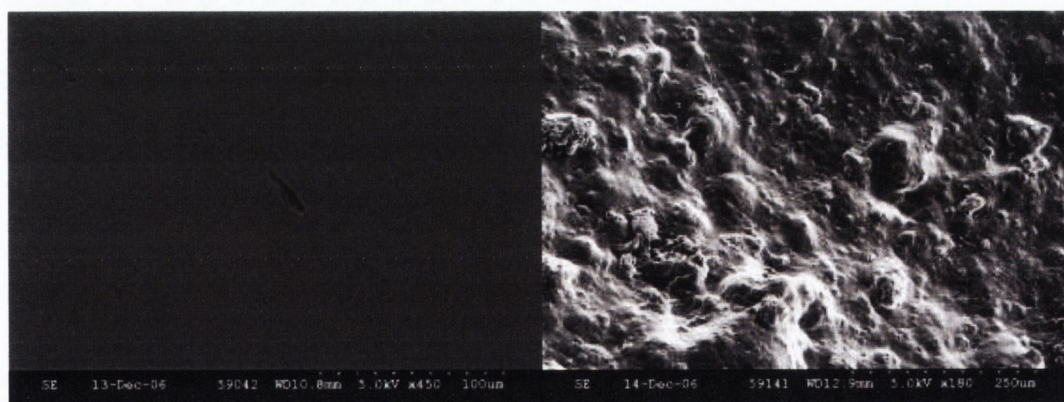
Figure 4.17 – SEMs of the surface of a First Contact polymer film (left) and the 0.027 volume fraction MWNT/First Contact composite.

The pure polymer surface is shown at a significantly higher magnification than the composite surface in order to make the difference between the surfaces more evident. The First Contact polymer is almost completely smooth at the level of tens of microns. The composite surface is extremely rough and this roughness is visible at magnifications as low as ×50. Some particles on the surface of the composite film do not seem to have a polymer

71

coating, but these are in the minority as most of the surface does appear to have a polymer coating. At lower volume fractions, the surface roughness would be expected to be reduced, as the content of nanotubes is reduced, but the surface wetting of the nanotubes should be similar.
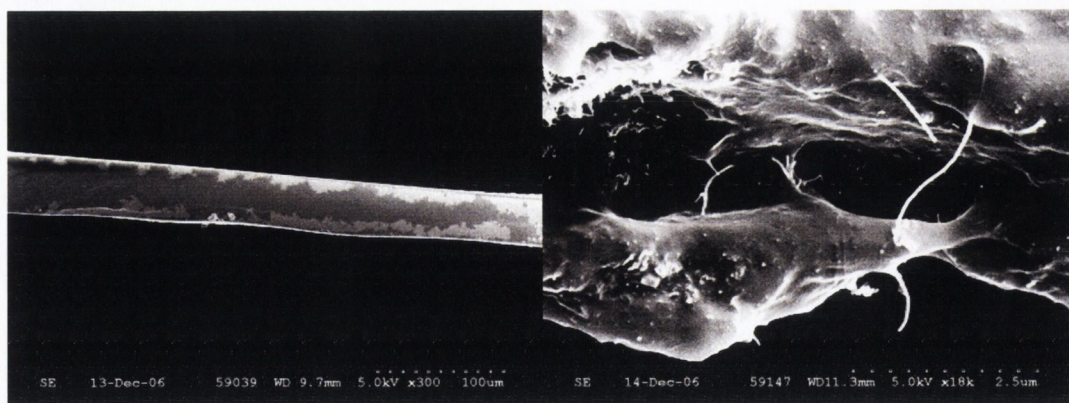
Figure 4.18 – SEMs of the fracture surface of the First Contact film (left) and the 0.027 volume fraction composite film (right).

When examining the fracture surface of the First Contact polymer, it was found to be quite smooth and uniform. In contrast, the composite fracture surface was quite rough and jagged with nanotubes visible protruding from the film. Nanotubes have been observed in fracture surfaces previously [32, 34] and this is a failure mechanism of the composites. If the polymer-nanotube interface is weak, a stress sufficient to break the nanotubes cannot be transferred from the polymer matrix and the matrix fails first. The average diameter of the nanotubes protruding was 47 ± 11 nm, which is far above the average diameter of the raw nanotubes, 14 ± 6 nm, previously measured from SEMs [6]. For these SEMs, there was a metal layer deposited of approximately 10 nm to prevent charging of the sample. Considering this, the SEMs indicate there is a thin layer, ~ 7 nm, of polymer around the nanotubes that did not fail, which demonstrates the strength of the interaction between this polymer and the nanotubes. Previously, Coleman et al. have observed coatings of approximately 20 nm and Ding et al. has observed coatings as thick as 48 nm. They were both using semi-crystalline polymers and Coleman et al. demonstrated that the polymer coating was crystalline. Here, the lack of crystallinity would mean the nanotubes were surrounded by weaker polymer and a thinner layer would be likely to remain on pull-out. This shows there is good wetting of the polymer to the nanotubes and there is a strong interaction up to ~ 10 nm around the nanotube. This relatively thin layer of polymer would support the results from the electrical measurements where high conductivities were achieved and a high conductivity prefactor, σ_0, was determined indicating close proximity of nanotubes in the composite and hence thin tunnelling barriers between the nanotubes.

72

4.5 Conclusions

The mechanical and electrical properties of MWNTs and a novel polymer, First Contact, were investigated. The mechanical measurements showed the Young's modulus of the polymer was unaffected by the presence of the nanotubes. The other mechanical properties are somewhat degraded, but overall the performance of the elastomer has not been significantly changed. Further study of the fracture surface showed good wetting of the polymer to the nanotubes and thin polymer coatings on the nanotubes pulled out at failure. The polymer coatings on the nanotubes demonstrate there is an interaction, which is in accordance with the excellent ability of the polymer to disperse nanotubes.

By measuring the conductivities for a range of volume fractions the percolation threshold, ϕ_c, for the MWNT/First Contact system was calculated to be $(5.0 \pm 0.5) \times 10^{-6}$. Therefore, only small amounts of the MWNTs are required to increase the conductivity of the composite. Above the percolation threshold, the conductivity rapidly increases, until it reaches a maximum of ~1 S m^{-1} at volume fractions above ~10^{-4}. At volume fractions low enough for the composites to be transparent, a conductivity of 0.20 S m^{-1} were achieved. The parameters from the percolation fit suggest that the low percolation threshold and high conductivities are due to thin tunnelling barriers between nanotubes in the composites which is due to the polymer used.

The conductivities of the composites are sufficient for use in electrostatic dissipation or electrostatic painting. However, the maximum conductivity measured, 0.86 S m^{-1}, is just short of the limit for electromagnetic interference shielding. It could be possible to increase this by using nanotubes with less defects than the CVD-MWNTs used in this study, and hence would be more conductive. The polymer itself has many desirable properties, as it is a barrier to sulphur, oxygen and water vapour. It can also be removed leaving no residue, which has led to it being suggested for use as a packaging for precision optics components or other sensitive objects. By introducing nanotubes, the mechanical properties of the polymer have not been significantly degraded, but the electrical properties have been altered substantially. The composite material could be used as electrostatic dissipation packaging to prevent damage to electronics, as well as protecting against chemical damage or damage due to handling. Conductive elastomers have also been suggested for use as seals between pipes used for transferring flammable gases, for electrostatic automotive painting [17] and MWNT/elastomer composites have been demonstrated as photomechanical actuators [35], which are all possible applications for these MWNT/First Contact composites.

4.6 References

[1]   Photonic Cleaning Technologies - http://www.photoniccleaning.com (2007)

[2]   Smithsonian Institution website - http://www.si.edu (2007)

[3]   From: http://www.astro.virginia.edu (2007)

[4]   R. D. Deegan, O. Bakajin, T. F. Dupont, G. Huber, S. R. Nagel, and T. A. Witten, Nature 389 (1997) 827.

[5]   W. R. Small, C. D. Walton, J. Loos, and M. inhet Panhuis, Journal of Physical Chemistry B 110 (2006) 13029.

[6]   Y. R. Hernandez, A. Gryson, F. M. Blighe, M. Cadek, V. Nicolosi, W. J. Blau, Y. K. Gun'ko, and J. N. Coleman, Submitted to Applied Physics Letters (2006)

[7]   E. J. Garboczi, K. A. Snyder, J. F. Douglas, and M. F. Thorpe, Physical Review E 52 (1995) 819.

[8]   R. Murphy Ph.D. Thesis, in the School of Physics, Trinity College Dublin, Ireland, 2006.

[9]   P. G. Collins, M. S. Arnold, and P. Avouris, Science 292 (2001) 706.

[10]   B. Vigolo, C. Coulon, M. Maugey, C. Zakri, and P. Poulin, Science 309 (2005) 920.

[11]   D. S. McLachlan, C. Chiteme, C. Park, K. E. Wise, S. E. Lowther, P. T. Lillehei, E. J. Siochi, and J. S. Harrison, Journal of Polymer Science Part B: Polymer Physics 43 (2005) 3273.

[12]   R. Ramasubramaniam, J. Chen, and H. Liu, Applied Physics Letters 83 (2003) 2928.

[13]   R. Murphy, V. Nicolosi, Y. Hernandez, D. McCarthy, D. Rickard, D. Vrbanic, A. Mrzel, D. Mihailovic, W. J. Blau, and J. N. Coleman, Scripta Materialia 54 (2006) 417.

[14]   J. K. W. Sandler, J. E. Kirk, I. A. Kinloch, M. S. P. Shaffer, and A. H. Windle, Polymer 44 (2003) 5893.

[15]   H. D. Young, University Physics, Addison-Wesley, 1992.

[16]   M. S. P. Shaffer and A. H. Windle, Advanced Materials 11 (1999) 937.

[17]   H. Koerner, W. Liu, M. Alexander, P. Mirau, H. Dowty, and R. A. Vaia, Polymer 46 (2005) 4405.

[18]   V. Skákalová, U. Dettlaff-Weglikowska, and S. Roth, Synthetic Metals 152 (2005) 349.

[19]   B. E. Kilbride, J. N. Coleman, J. Fraysse, P. Fournet, M. Cadek, A. Drury, S. Hutzler, S. Roth, and W. J. Blau, Journal of Applied Physics 92 (2002) 4024.

[20]   R. Zallen, The Physics of Amorphous Solids, Wiley, 1983.

[21]   D. Stauffer and A. Aharony, Introduction to Percolation Theory, Taylor & Francis, 1991.

[22]   I. Balberg, Physical Review B 57 (1998) 13351.

[23]   M. Foygel, R. D. Morris, D. Anez, S. French, and V. L. Sobolev, Physical Review B 71 (2005) 104201.

[24]   S. Vionnet-Menot, C. Grimaldi, T. Maeder, S. Strassler, and P. Ryser, Physical Review B 71 (2005) 064201.

[25]   W. Chen, X. Tao, and Y. Liu, Composites Science and Technology 66 (2006) 3029.

[26]   J. Xiong, Z. Zheng, X. Qin, M. Li, H. Li, and X. Wang, Carbon 44 (2006) 2701.

[27]   A. Dufresne, M. Paillet, J. L. Putaux, R. Canet, F. Carmona, P. Delhaes, and S. Cui, Journal of Materials Science 37 (2002) 3915.

[28]   J. N. Coleman, U. Khan, W. J. Blau, and Y. K. Gun'ko, Carbon 44 (2006) 1624.

[29]   M. Cadek, J. N. Coleman, V. Barron, K. Hedicke, and W. J. Blau, Applied Physics Letters 81 (2002) 5123.

[30]   C.-M. Wu, M. Chen, and J. Karger-Kocsis, Polymer 42 (2001) 129.

[31]   K. P. Ryan, M. Cadek, V. Nicolosi, S. Walker, M. Ruether, A. Fonseca, J. B. Nagy, W. J. Blau, and J. N. Coleman, Synthetic Metals 156 (2006) 332.

[32]   K. P. Ryan, S. M. Lipson, A. Drury, M. Cadek, M. Ruether, S. M. O'Flaherty, V. Barron, B. McCarthy, H. J. Byrne, W. J. Blau, and J. N. Coleman, Chemical Physics Letters 391 (2004) 329.

[33]   R. Murphy, in Physics, Vol. Doctor of Philosophy, Trinity College Dublin, Ireland, 2006.

[34]   W. Ding, A. Eitan, F. T. Fisher, X. Chen, D. A. Dikin, R. Andrews, L. C. Brinson, L. S. Schadler, and R. S. Ruoff, Nano Letters 3 (2003) 1593.

[35]   S. V. Ahir and E. M. Terentjev, Nature Materials 4 (2005) 491.

CHAPTER 5

Dispersion Studies of $Mo_6S_3I_6$ Nanowires

5.1 Introduction

As discussed in chapter 2, the family of MoSI nanowires are an interesting new one-dimensional nanostructure with a range of potential applications [1-3]. Carbon nanotubes have been the main focus of research in this field for the last 10 years [4], but many inorganic nanowires [5, 6] have been produced which could be suitable alternatives. The physical properties of the MoSI nanowires are comparable to the properties of carbon nanotubes [7], but with several advantages such as a simple and scalable synthesis [8] and identical electronic properties within each stoichiometry [9]. Also, they have been shown to disperse easily in common solvents, a problem which is only now starting to be overcome for carbon nanotubes [10-12].

Previously, the dispersion properties for the $Mo_6S_{4.5}I_{4.5}$ nanowires in various solvents have been studied and the best solvent and maximum dispersability were determined [13]. That work demonstrated that these nanowires can be purified by allowing the impurities to sediment out of solution, leaving a stable dispersion of nanowires. Here, a similar study for the $Mo_6S_3I_6$ material is presented. Although these two materials are structurally quite similar, they have been shown to have very different dispersion properties due to differences in the arrangement of their surface atoms.

In the work presented in this chapter, dispersions of $Mo_6S_3I_6$ nanowires in various solvents were monitored by measuring their optical transmission as a function of time. As described in chapter 3, the transmission is related to the local concentration in the dispersions and allows the sedimentation of insoluble material to be observed. Transmission electron microscopy (TEM) was used to examine the sedimenting material and the stably dispersed material. From the sedimentation data, it was then possible to separate the different components and further analyses were performed on them, including UV-vis-IR spectroscopy, X-ray photoelectron spectroscopy (XPS) and scanning electron microscopy (SEM). From these measurements, the best solvents for dispersing the $Mo_6S_3I_6$ nanowires for further applications and the maximum amount of nanowires dispersible were determined. These results will be applied to the further composite work with the material in chapter 6.

5.2 Sedimentation Studies

5.2.1 *Sedimentation Results*

The dispersability of $Mo_6S_3I_6$ nanowires in various solvents - acetone, chloroform, N,N-dimethylformamide (DMF), dimethyl sulfoxide (DMSO), ethanol, isopropanol (IPA), 1-methyl-2-pyrrolidinone (NMP), and water – was measured to determine the best solvent for this material. This was done by measuring the transmission through the centre of 0.1 g L^{-1} $Mo_6S_3I_6$ dispersions in these solvents as a function of time for up to 750 hours. As described in chapter 3, the transmission could then be converted to the local effective concentration, C_{eff}, and this is plotted as a function of time in figure 5.1. For all solvents, the total effective concentration of the dispersions decreases with time, due to the sedimentation of insoluble material, until it reaches a constant value equal to the effective concentration of the stably dispersed material when sedimentation is complete.

From figure 5.1 it can be seen that the $Mo_6S_3I_6$ behaves differently in each solvent with the rate of sedimentation and the final effective concentration varying greatly between solvents. From this data, it is clear that DMF, acetone and ethanol have a significantly higher amount of stably dispersed material than chloroform, DMSO or water. Therefore, DMF, acetone and ethanol could be considered good solvents for the $Mo_6S_3I_6$ material, whereas chloroform, DMSO and water would be considered poor solvents.
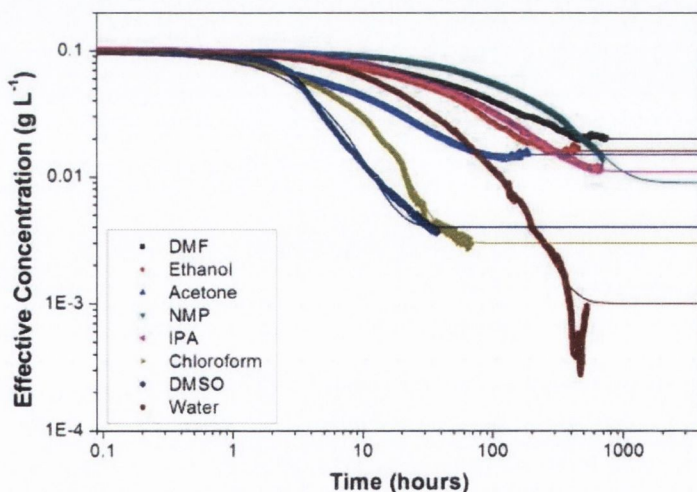
Figure 5.1 – Experimental sedimentation curves for 0.1 g L^{-1} dispersions of the washed $Mo_6S_3I_6$ material in common solvents with the bi-exponential fits shown as thin lines.

From sedimentation theory it is predicted that the concentration of any insoluble phase should decay exponentially with time. To test this, each sedimentation data set was fitted to equation 5.1, which describes the rate of change of concentration, C, for multiple sedimenting components, C_n, and one stable component, C_0.

$$C(t) = C_0 + \sum_n C_n e^{-t/\tau_n}$$

<div align="right">Equation 5.1</div>

For all solvents, except DMSO, the best fit was found to be a bi-exponential decay with a constant component. This implies that there are two insoluble components and one stably dispersed component in the $Mo_6S_3I_6$ material. For DMSO, the $Mo_6S_3I_6$ behaved quite differently to the other solvents by beginning to sediment out quite abruptly in the first few hours. The best fit possible to the DMSO data was a single exponential. The fits to all of the experimental data are shown in figure 5.1 as thin solid lines. From the fit, five parameters can be extracted (except for DMSO where there are only three parameters), the effective concentrations of each phase and the time constants: $C_{eff,0}$, $C_{eff,1}$, $C_{eff,2}$, τ_1, τ_2. The values calculated from the fits for each solvent, and the error as determined by the fit, are listed in table 5.1. As $C_{eff,0}$ represents the stably dispersed material, this data indicates that the best solvents for the $Mo_6S_3I_6$ nanowires stably disperse a $C_{eff,0}/C_{Total}$ of 20% for DMF, followed by a $C_{eff,0}/C_{Total}$ of 16% and 15% for acetone and ethanol, respectively. NMP and IPA have a reasonable amount of material stably dispersed also, but water, DMSO and chloroform all have $C_{eff,0}/C_{Total}$ less than 4%.

	$C_{eff,0}/C_{Total}$	$C_{eff,1}/C_{Total}$	τ_1 (hrs)	$C_{eff,2}/C_{Total}$	τ_2 (hrs)	NWs	Imps
DMF	0.20 ± 0.02	0.34 ± 0.03	13.6 ± 0.04	0.46 ± 0.05	122.1 ± 0.2	Y	N
Ethanol	0.16 ± 0.02	0.27 ± 0.03	5.3 ± 0.02	0.6 ± 0.06	59.9 ± 0.1	Y	Y
Acetone	0.15 ± 0.02	0.39 ± 0.04	2.1 ± 0.02	0.48 ± 0.05	18.7 ± 0.03	Y	N
NMP	0.09 ± 0.01	0.29 ± 0.03	41.5 ± 0.06	0.63 ± 0.06	287.7 ± 0.3	Y	Y
IPA	0.11 ± 0.01	0.41 ± 0.04	17.8 ± 0.02	0.47 ± 0.05	122.2 ± 0.1	Y	N
Chloroform	0.03 ± 0.00	0.18 ± 0.02	1.8 ± 0.03	0.8 ± 0.08	9.0 ± 0.02	Y	N
DMSO	0.04 ± 0.00	0.99 ± 0.10	4.3 ± 0.02	-	-	N	Y
Water	0.01 ± 0	0.63 ± 0	14.2 ± 0.02	0.36 ± 0	84.9 ± 0.1	N	N

Table 5.1 – Fit parameters from the exponential fits to the sedimentation data shown in figure 5.1 are shown in columns 1 – 5. In columns 6 & 7, the presence, or absence, of nanowires and impurities in each dispersion after sedimentation is indicated.

It should be pointed out that the $C_{eff,1}$ and $C_{eff,2}$ values represent the effective concentrations of phases 1 and 2 in each solvent. However, like $C_{eff,0}$, these quantities should only be taken as guidelines to the amount of each phase present. As discussed

previously they are effective quantities and cannot be translated into real concentrations unless the absorption coefficients of the individual phases are known.

5.2.2 *Transmission Electron Microscopy*

Before sedimentation, and immediately after sonication, a TEM grid was prepared from the dispersions of $Mo_6S_3I_6$. A second TEM grid was prepared from the $Mo_6S_3I_6$ dispersion immediately after sedimentation had completed and a third TEM grid was prepared with the sediment after sedimentation. This was done for each solvent in order to monitor the changes that occur during sedimentation. Examples of these TEM images, taken for the best solvent, DMF, are shown in figure 5.2.
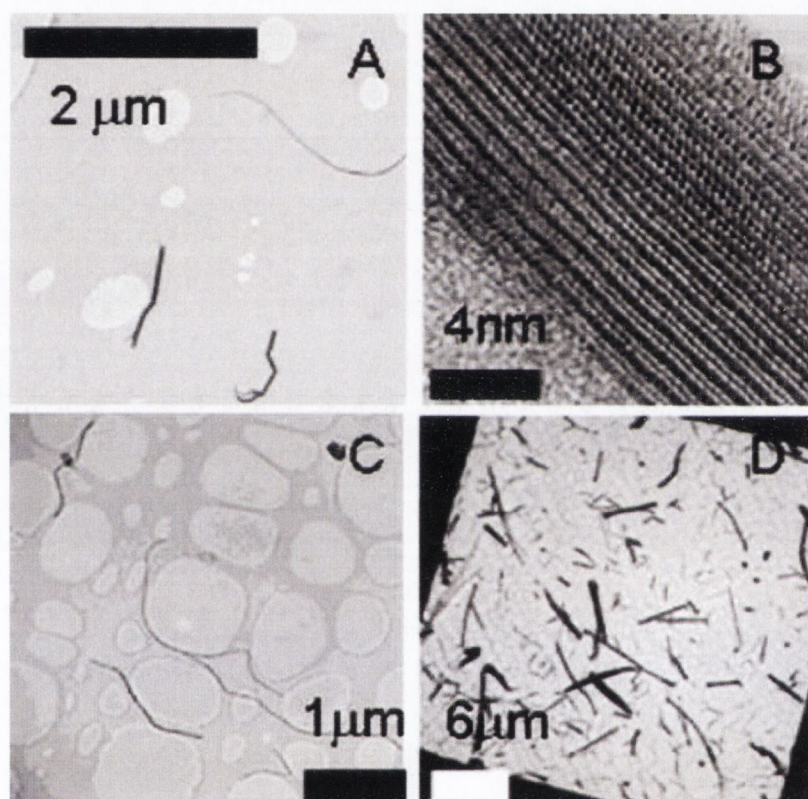
Figure 5.2– Transmission electron microscopy images of the $Mo_6S_3I_6$ nanowire dispersion in DMF immediately after sonication (top left), HRTEM image of a dispersed bundle (top right), the dispersion after sedimentation (bottom left), and the sediment after sedimentation (bottom right).

The material which remains dispersed in the DMF after sedimentation, i.e. the stably dispersed material, mainly consists of smaller diameter nanowire bundles as shown in figure 5.2(a). In figure 5.2(b), a high-resolution image of one of these bundles showing the individual nanowires is shown [14]. Before sedimentation the dispersion contains large diameter bundles and pseudo-spherical impurities as shown in figure 5.2(c). In contrast, the dispersions after sedimentation were free of impurity material as will be discussed below. The sediment consisted of very large diameter bundles and impurity material as shown in figure 5.2(d).

79

From the large number of TEMs taken, the dimensions of approximately 100 nanowire bundles in each of the best solvents (DMF, Ethanol, Acetone and NMP) before sedimentation began, and after sedimentation had completed, were measured and the averages are listed in table 5.2. These measurements clearly show that the material that remains dispersed after sedimentation consists of smaller diameter bundles relative to the original dispersion. This agrees with sedimentation theory, which predicts the diameter of the sedimenting bundles would be expected to be larger than the stably dispersed bundles. The bundles in the sediment are substantially larger than the bundles observed before sedimentation, and this is most likely due to aggregation of the nanowires after sedimentation.

	d_{before} (nm)		L_{before} (µm)		d_{after} (nm)		L_{after} (µm)	
	mean	*range*	*mean*	*range*	*mean*	*range*	*mean*	*range*
DMF	60	11 – 464	0.9	0.09 - 13	12	2 – 130	0.6	0.15 – 1.9
Ethanol	133	6 – 4233	1.2	0.02 – 8.4	33	7 – 100	0.7	0.08 – 2.5
Acetone	67	8 – 651	1.2	0.1 - 10	39	11 – 95	0.9	0.09 – 4.5
NMP	56	11 – 307	1.0	0.08 – 5.3	19	4 - 80	0.4	0.05 – 1.8

Table 5.2 – Average lengths and diameters of $Mo_6S_3I_6$ nanowire bundles, as measured from TEMs, for the best solvents before and after sedimentation. These measurements are used in the plots in figure 5.4.

The as-produced $Mo_6S_3I_6$ material has been shown to be in the form of needles with diameters ranging from 50 - 1000 nm, and up to 5 mm in length [8]. After sonication, pseudospherical impurities (similar to those seen in $Mo_6S_{4.5}I_{4.5}$ [13]) and a large number of nanowire bundles were observed in the TEM images all of the solvents. From the data in table 5.2, it can be seen that for the best solvents the average nanowire bundle diameters ranged from 56 nm for NMP, to 133 nm for ethanol. The average lengths varied from 0.9 µm for DMF, to 1.2 µm for acetone, demonstrating the effectiveness of the sonication in breaking up the large bundles in the synthesised material.

In the TEM images after sedimentation, the dimensions of the dispersed bundles had decreased to diameters of between 12 ± 14 nm and 39 ± 19 nm, and lengths of between 0.4 ± 0.3 µm and 0.9 ± 0.7 µm. This decrease in the average diameters and lengths indicates that the larger diameter bundles have sedimented out, with only the smaller bundles remaining. The nanowire bundles in DMF, which was shown to be the best solvent from the sedimentation results, had the smallest average diameters at 12 ± 14 nm, in

agreement with this observation. The presence, or absence, of nanowires and impurities in the dispersions after sedimentation was noted for each solvent. The results are shown in the right-hand columns of table 5.1, labelled "NWs" for nanowires and "Imps" for impurities. "Y" in the relevant column indicates the presence of nanowires/impurities, and "N" indicates none are present. These results show that sedimentation of the $Mo_6S_3I_6$ nanowires in DMF is effective at purifying the material. Acetone retains slightly less nanowires making it a second possibility for purification. The other two solvents that retain a significant amount of material, Ethanol and NMP, are not suitable for purification as they also retain measurable amounts of impurities. The rest of the solvents do not retain enough nanowires to make them a practical choice for purification, as was determined from the $C_{eff,0}/C_{Total}$ value and the amount of nanowires observed on the TEM grids prepared after sedimentation.

As mentioned previously, DMSO behaved differently to all of the other solvents. The best fit to the DMSO data was a single exponential, consistent with one sedimenting phase, whereas two distinct sedimenting phases were identified in all of the other solvents. No nanowires were observed in TEMs of the DMSO dispersion after sedimentation. DMSO appears unable to suspend significant amounts of the impurities or the nanowires for longer than 36 hours. Previously, it was shown that DMSO and chloroform were among the best solvents for dispersing $Mo_6S_{4.5}I_{4.5}$ nanowires [13], but these are amongst the worst solvents for dispersing the $Mo_6S_3I_6$ nanowires. Similarly, ethanol and acetone, which do not disperse $Mo_6S_{4.5}I_{4.5}$, do disperse $Mo_6S_3I_6$. Although, DMF disperses both nanowire stoichiometries, the results for the other solvents indicate dramatically different dispersion properties for the different MoSI nanowire stoichiometries. This clearly indicates the fact that the surface arrangement of atoms, i.e. those that interact with the solvent, must be different for $Mo_6S_{4.5}I_{4.5}$ and $Mo_6S_3I_6$ [15].

5.2.3 *Comparison with Sedimentation Theory*

For each solvent, except DMSO, the time constants for the two sedimenting phases, τ_1 and τ_2, were calculated from the fits to the experimental data using equation 5.1. These two time constants have been characterised as short, τ_{short}, and long, τ_{long}, with the short time constant representing the material that sediments first. As discussed above, the impurity material tends to sediment out of most solvents to a reasonable degree. This suggests that the short time constant represents the pseudo-spherical impurity material. This has been confirmed for $Mo_6S_{4.5}I_{4.5}$ nanowires [13, 16]. Thus, the short time constant

should be described by equation 5.2, which was previously derived in chapter 2, and is appropriate to spherical objects.

$$\tau_{spherical} = \frac{9\eta(\beta - p_f)}{2g^2(\rho_s - \rho_l)^2 a^2}$$

Therefore, the time constant should scale with $\eta/(\rho_s - \rho_l)^2$. In figure 5.3, the shorter time constant, which we will refer to as τ_{short}, is plotted against $\eta/(\rho_s - \rho_l)^2$ for all solvents (except DMSO). If we ignore NMP, the trend is approximately linear as is predicted by equation 5.2. The deviations from linearity are to be expected as equation 5.2 shows that τ_{short} also depends on the diameter of the sedimenting particles. These particles are thought to be aggregates of smaller impurity particles. Thus, the degree to which they break up on sonication and hence the dimensions of the sedimenting particles may vary between solvents.
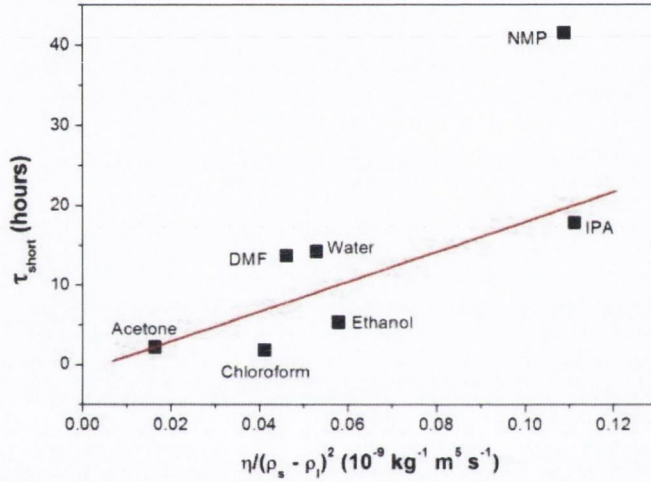
Figure 5.3 - τ_{short} for all solvents (except DMSO) plotted against parameters from equation 5.2.

In analogy with previous work on $Mo_6S_{4.5}I_{4.5}$ the longer time constant, τ_{long}, is expected to relate to nanowire bundles that are unstable in the solvents studied. Due to their high aspect ratio and small radius, these cylindrical objects tend to sediment slowly, as predicted by equation 5.3.

$$\tau_{cylindrical} = \frac{6K\eta(\beta - p_f)(3/4)^{1/3}}{g^2(\rho_s - \rho_l)^2(r^2l)^{2/3}}$$

In addition, cylinders have a higher drag coefficient, K, relative to spheres, further slowing sedimentation [17]. The nature of the sedimenting phases is investigated in section 5.3.
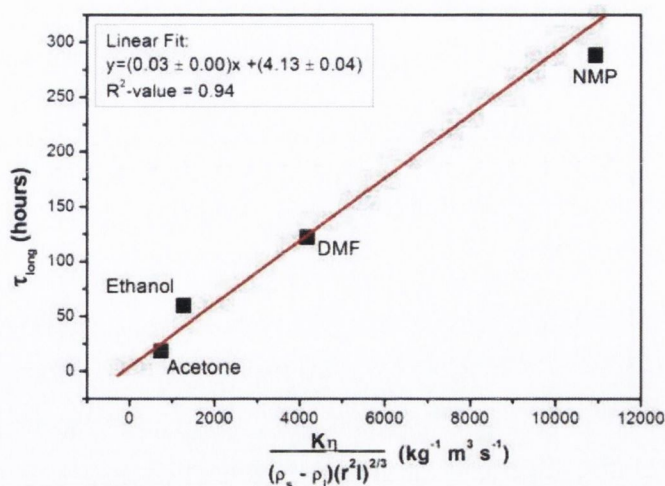
Figure 5.4 - τ_{long} for the best solvents plotted against the parameters for cylindrical particles as in equation 5.3, demonstrating agreement with sedimentation theory. The linear fit parameters to the data are included in the inset.

According to equation 5.3, τ_{long} depends on the solvent viscosity, η, the density difference between solvent and sedimenting object, $(\rho_s - \rho_l)$ and the dimensions of the sedimenting object, r and l, both directly and indirectly through the drag coefficient, K. In figure 5.4, τ_{long} is plotted for the four best solvents, as a function of $K\eta/(\rho_s - \rho_l)(r^2 l)^{2/3}$. The length and diameter used are approximated with the averages measured before sedimentation, as quoted in table 5.2, above. The drag coefficient, K, was also calculated using these bundle dimensions [17]. This results in an excellent linear fit encompassing all four solvents from which $(\beta - p_f)$ can be calculated to be ~1900 Pa. In the cuvette used for these experiments, the fluid pressure was always very close to atmospheric pressure. Therefore, the solid-fluid interaction parameter, β, is within 2% of atmospheric pressure, 10^5 Pa. No other numerical value for β was found in the literature for any system for comparison with the value calculated here.

From the equation 5.3, describing τ_{long}, it is clear that this time constant is expected to increase with increasing solvent viscosity. NMP is the most viscous and acetone the least viscous of these solvents, with viscosities of 1.8 and 0.304 mPa s^{-1}, in agreement with this, but ethanol is more viscous than the DMF, at 1.078 mPa s^{-1} compared to 0.796 mPa s^{-1}, demonstrating that viscosity is not the dominant parameter. As would be expected, the dimensions of the nanowires in each solvent are the most important factor for sedimentation and, as stated earlier, it is not clear what solvent properties determine the performance of the solvents in dispersing the nanowires. It is possible that the material is not stably dispersed, but is just sedimenting extremely slowly compared to the other phases. For the best solvent, DMF, the time constant for the stable phase can be calculated using equation 5.3 and the dimensions measured from the TEMs. This gives a time

83

constant of ~2300 hours, or 18 times longer than the time constant for phase 2. Therefore, it would take approximately 1 year for this phase to sediment from solution. Effectively this phase is stable over any time scale that the material would be used, as this time constant implies almost no material would have sedimented after 1 month which is as observed in the sedimentation experiments.

5.2.4 _Comparison between Washed and Unwashed $Mo_6S_3I_6$ material_

Initially, the sedimentation studies were begun on the as-received $Mo_6S_3I_6$ material before the effect of the leaching of iodine was realised. The as-received material was then washed and the study was then repeated. Both the washed and unwashed $Mo_6S_3I_6$ sedimentation data were analysed by fitting to equation 5.1 and the calculated values for both are listed in table 5.3. Comparison of the data for the washed material, iodine removed, and the unwashed material, iodine still present, indicates the effect of the removal of iodine on the material.

		$C_{eff,0}/C_{Total}$	$C_{eff,1}/C_{Total}$	τ_{short} (hrs)	$C_{eff,2}/C_{Total}$	τ_{long} (hrs)
DMF	washed	0.2	0.34	13.6	0.46	122.1
	unwashed	0.25	0.37	3.7	0.37	50
Ethanol	washed	0.16	0.27	5.3	0.6	59.9
	unwashed	0.14	0.34	2.3	0.51	42
Acetone	washed	0.15	0.39	2.1	0.48	18.7
	unwashed	0.16	0.35	6.4	0.49	50.3
NMP	washed	0.09	0.29	41.5	0.63	287.7
	unwashed	0.31	0.29	10.9	0.39	74
IPA	washed	0.11	0.41	17.8	0.47	122.2
	unwashed	0.17	0.32	6.2	0.5	86
Chloroform	washed	0.03	0.18	1.8	0.8	9.0
	unwashed	0	0.58	1	0.40	30.4
DMSO	washed	0.04	0.99	4.3	-	-
	unwashed	0.06	0.99	4.1		
Water	washed	0.01	0.63	14.2	0.36	84.9
	unwashed	0.16	0.35	6.4	0.49	50.2

Table 5.3 - Fit parameters from exponential fits to the sedimentation data for the washed $Mo_6S_3I_6$ material, as listed in table 5.1 and for the unwashed $Mo_6S_3I_6$ material. Highlighted in red are time constants for the unwashed material which are longer than for the washed material.

From the data in table 5.3, it can be seen that the effect of washing the $Mo_6S_3I_6$ material varies between solvents. For DMSO there was almost no change, whereas NMP has a large decrease in the calculated $C_{eff,0}/C_{Total}$ from 0.31 for the unwashed material to

0.09 for the washed material and significant increases in the time constants. As iodine solutions absorb in the visible region, the transmittance of the dispersions over time will be reduced by its presence in solution, leading to an exaggeration of the amount of stably dispersed material, $C_{eff,0}/C_{Total}$ and hence $C_{eff,1}/C_{Total}$ and $C_{eff,2}/C_{Total}$ will be distorted. This effect varies between solvents, as the iodine solubility and its interaction with the solvent both have a large effect on its absorption. Also, differences between the content of each batch prepared will lead to a variation in the concentrations of each phase. These effects make it difficult to interpret the observed changes in the effective concentration. It should be noted that despite these various influences, the calculated parameters for DMSO do not change significantly. The $Mo_6S_3I_6$ precipitates within hours from solution, whether it is washed or unwashed, demonstrating it is a non-solvent for the material.

The time constants for each phase are expected to remain constant between samples irrespective of the amount of each phase present, if the removal of the iodine does not affect the structure of the impurities and the bundles. As the rate of sedimentation is directly related to the dimensions of the sedimenting particles, any change due to the removal of iodine should be observed as a change in the time constants, τ_{short} and τ_{long}.

For all solvents, except DMSO and acetone, the time constants for the first phase of the washed material, τ_{short}, are significantly larger than for the unwashed material. This indicates that the impurity particles are sedimenting more slowly for the washed material relative to the unwashed material. If the iodine was binding impurity particles together, its removal would result in smaller diameter impurity particles which, as shown in equation 5.2, would sediment more slowly. This would explain the observed increase in time constants for phase 1. The decrease in both time constants is due to acetone being used in the washing process of the $Mo_6S_3I_6$ material. Small quantities of $Mo_6S_3I_6$ material were lost during this process, as not all material could be removed from solvent by centrifugation. The material lost would be the material which remains dispersed longest in the acetone and the material which sediments faster would be recovered more easily. Despite this, acetone is still able to stably disperse a large amount of the nanowire material, $C_{eff,0}/C_{Total} = 0.15$.

For the second phase, which is expected to be nanowires, the time constants, τ_{long}, are increased for all solvents except DMSO, chloroform and acetone. Similarly, the binding effect of the iodine on the nanowire bundles would lead to smaller bundles in the washed material which would sediment more slowly. The decrease observed for acetone can also be explained by the washing process. The reason for the substantial decrease in the longer time constant for washed $Mo_6S_3I_6$ in chloroform is not clear, but it is unable to

85

disperse a significant amount of washed or unwashed material. The repeated sonication involved in the washing procedure would be expected to break up the large particles and bundles also. This should not affect the time constants though, as they re-aggregate into large bundles when they sediment out after each washing step. This was observed in the TEM images after sedimentation where much larger bundles are visible.

5.3 Purification by Sedimentation

Equation 5.1 shows that the material will sediment exponentially and from this equation it can be calculated that greater than 99% of a sedimenting phase will have sedimented out after 5τ, where τ is the time constant for the sedimenting phase. Therefore, using the calculated time constants for the sedimenting phases of the washed $Mo_6S_3I_6$ material in DMF, τ_1 and τ_2, (τ_{short} and τ_{long}), it can be shown that phase 1 and phase 2 will have almost completely sedimented from solution after approximately 70 hours and 600 hours respectively. In figure 5.5, this is illustrated by showing the experimental data with the fit, and the theoretical sedimentation curves for each phase generated from the fit. Therefore, the two sediments and the solute can be separated by carefully decanting after 70 hours to give a sediment of mainly phase 1, and after 600 hours to give a sediment of mainly phase 2. The remaining solvent will contain the solute. It should be pointed out that perfect separation can never be achieved in this manner, only significant enrichment of a given phase.
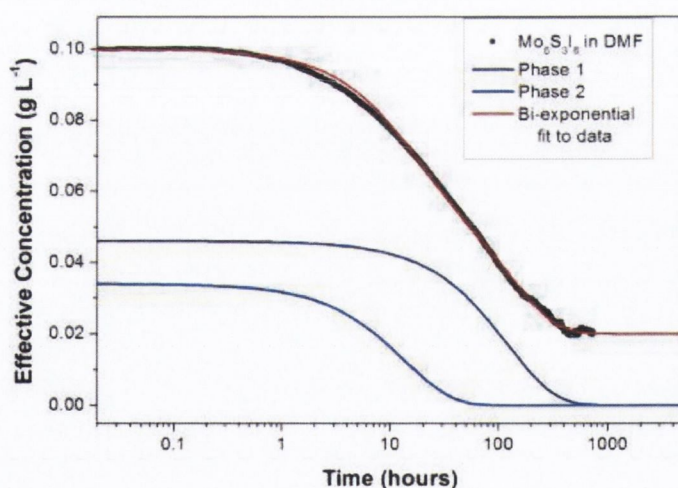
Figure 5.5 - Normalised effective concentration of $Mo_6S_3I_6$ in DMF (black data points), with the bi-exponential fit (red line) shown, and the decay curves as calculated for sedimenting phase 1 (light blue line) and sedimenting phase 2 (dark blue line).

For the separation performed here, a higher concentration, 1 g L^{-1}, dispersion of the $Mo_6S_3I_6$ material in DMF was prepared by sonication, so significant masses were attained in the two sediments, and in the solvent after the final decantation. This dispersion was

then allowed to sediment for 70 hours before being decanted. The dispersion was sonicated again and allowed to sediment for 600 hours before being decanted a second time. The remaining dispersion was dried in a vacuum oven with the two sediments to remove the DMF, which has a high boiling point of ~150 °C. These three dried powders were then weighed. Initially, 24.7 mg of washed $Mo_6S_3I_6$ material was dispersed in DMF. The masses of sediment 1, sediment 2, and the solute recovered were 19.7 mg (~87%), 1.5 mg (~7%) and 1.4 mg (~6%) respectively, with 2.1 mg unrecoverable. It must be emphasised that these values are proportional to the *true* concentrations of the three phases and should not scale with the fit values for the *effective* concentrations, $C_{eff,1}$, $C_{eff,2}$ and $C_{eff,0}$ measured for the DMF dispersions.

From the masses of the two sediments and the solute it is possible to calculate the *true* concentrations of the phases, C_1, C_2 and C_0, using equation 5.1. The amount of each phase present in the two sediments and in the solute can be calculated using this equation as the time constants are known. The compositions of the three separated components, the solute, sediment 1 and sediment 2, are given by:

$$m_{solute} = C_0 + C_1 e^{-5\tau_2/\tau_1} + C_2 e^{-5\tau_2/\tau_2}$$

$$m_{sediment1} = C_1\left(1 - e^{-5\tau_1/\tau_1}\right) + C_2\left(1 - e^{-5\tau_1/\tau_2}\right)$$

$$m_{sediment2} = C_1\left(1 - e^{-5\tau_2/\tau_1}\right) + C_2\left(1 - e^{-5\tau_2/\tau_2}\right)$$

By solving these equations, the *true* concentrations of the three phases can be calculated to be 1.38 mg for the stably dispersed phase, C_0, 18.9 mg for the short sedimenting phase, C_1, and 2.4 mg for the long sedimenting phase, C_2. Now the purities of the separated components can be calculated. 99% of the solute is the stably dispersed material, with a negligible amount of the short sedimenting phase and 1% of the long sedimenting phase present also. The short sedimenting phase makes up 95% of the first sediment and the long sedimenting phase is 91% of the second sediment. This shows that the two sediments are greater than 90% pure. Due to the overlap in the sedimenting time constants, it is not possible to achieve a purer separation, but this is sufficient for further analysis. The solute is extremely pure, with less than 1 % of the sedimenting phases retained.

These results also demonstrate that after 600 hours 6% of the total $Mo_6S_3I_6$ material was still dispersed in DMF, at a concentration of approximately 0.06 g L^{-1}. It is not clear whether this represents a solubility limit or perhaps the fact that the fraction of dispersible

material in the washed powder was low. Nevertheless it shows that it is possible to produce stable dispersions of $Mo_6S_3I_6$ with concentrations as high as 0.06 g L^{-1}. This compares reasonably well with the previously achieved concentrations of 0.34 g L^{-1} for $Mo_6S_{4.5}I_{4.5}$ in isopropanol [16] or indeed of 0.02 g L^{-1} for single-walled carbon nanotubes in NMP [10].

5.3.1 *UV-vis-NIR Spectroscopy*

Each of the three recovered powders, sediment 1, sediment 2, and the solute were re-dispersed in IPA. For comparison purposes, the $Mo_6S_3I_6$ soot was also dispersed in IPA. It should be pointed out that each phase was generally insoluble in IPA. However, measurements could be made before any significant sedimentation had occurred. UV-vis-NIR spectroscopy in the range from 0.5 eV to approximately 4 eV was performed on these solutions and the recorded spectra, as well as a reference IPA spectrum, are shown in figure 5.6. In all 4 spectra, and as observed in similar spectra for $Mo_6S_{4.5}I_{4.5}$ [13], there are broad peaks visible at approximately 2.7 eV and 1.75 eV in the visible region. The main differences are observed in the near-IR region (~0.6 - 0.8 eV) and this region of the spectra is shown in greater detail in the four lower panes of figure 5.6. In the range from approximately 0.7 eV to 0.75 eV, there is much noise due to the subtraction of the IPA peaks from the individual spectra so no peaks are visible. In sediment 2 and in the solute a distinct peak is observed at 0.64 eV with a smaller shoulder at 0.66 eV. This demonstrates the similarity between these two phases, which both mainly contain $Mo_6S_3I_6$ nanowires, as observed in the TEM and SEM images and as calculated above. Such a feature has also been observed for $Mo_6S_{4.5}I_{4.5}$ nanowires [13]. The position of this peak agrees well with predictions for the MoSI bandgap [18] suggesting that it may represent a transition involving the van Hove singularity associated with the band edge. All of these features are visible in the washed $Mo_6S_3I_6$ sample, which should be a combination of these three phases, as was expected, although the peak at 0.64 eV is quite weak due to the high intensity of the near infrared peaks in sediment 1. At 0.64 eV in the sediment 1 spectrum, no substantial peak is visible, as it mainly contains the short phase, which is expected to be impurities. There is a trace of the long phase, which is expected to be sedimenting nanowires, but the amount is so small that it would not be expected to be visible in the spectra.
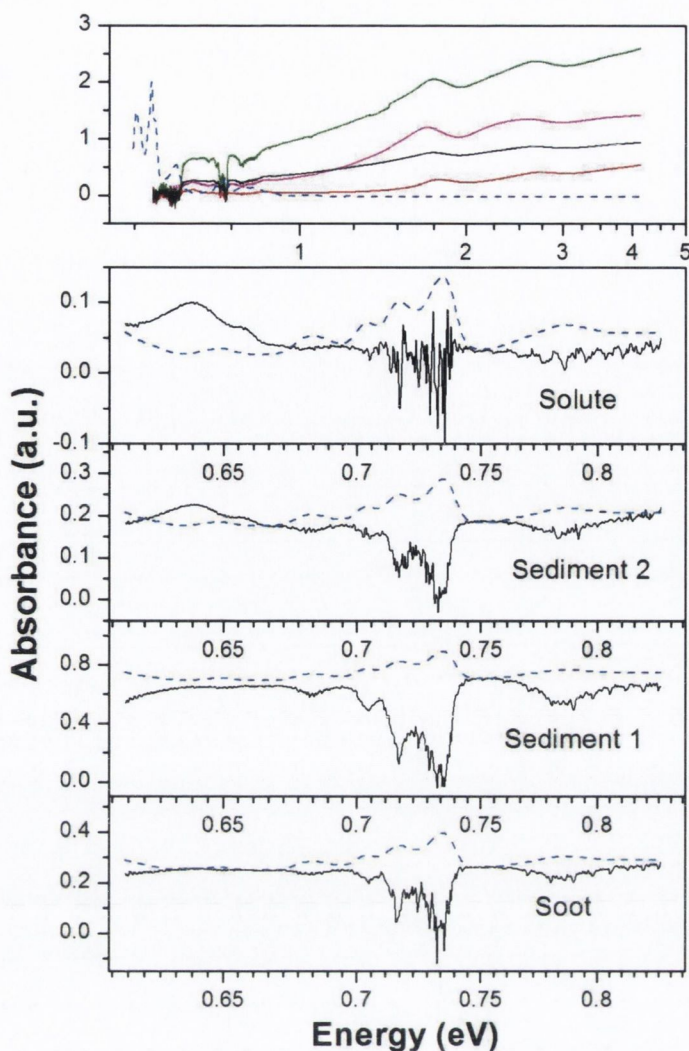
Figure 5.6 - UV-vis-IR absorption spectra of the washed $Mo_6S_3I_6$ powder (black line), the solute (red line), sediment 2 (magenta line) and sediment 1 (green line) dispersed in IPA are shown in the top graph. The near IR region for each material is shown in greater detail in the four spectra below. In all of the spectra, the IPA spectrum is shown as a blue dashed line.

5.3.2 X-ray Photoelectron Spectroscopy

As done previously for the $Mo_6S_{4.5}I_{4.5}$ nanowire material, the three phases, the as-produced (unwashed) and washed $Mo_6S_3I_6$ raw material, all dispersed in IPA, were sent to the University of Catania, Italy for X-ray photoelectron spectroscopy to be performed in order, to analyse the differences in the elemental components. The dispersions were deposited on silicon dioxide substrates and the spectra were analysed, ignoring the SiO_2 peaks, to determine the stoichiometries of the different samples. The peak fitting was performed using the Origin 7.5 peak fitting module by Valeria Nicolosi. The molybdenum, iodine, sulphur and oxygen spectra for the solute material are shown below in figure 5.7, and similar spectra were obtained and analysed for the other samples. The calculated stoichiometry for the as-produced material was $Mo_6S_{4.3}I_{11.8}$. However, after washing with acetone, the stoichiometry became $Mo_6S_{4.5}I_{8.6}$ showing the excess iodine content has been

89

substantially reduced, with approximately 27% less, by mass, present in the washed material.

For the two sediments, the calculated stoichiometries were $Mo_6S_{11}I_{0.8}$ for sediment 1 and $Mo_6S_{3.5}I_{7.9}$ for sediment 2. The stoichiometry of sediment 1 suggests it is mainly MoS_2 with traces of iodine present, which have been reported in the as-produced material [8] and in the $Mo_6S_{4.5}I_{4.5}$ material [13]. In addition, we cannot rule out the presence of some nanowires. Sediment 2 is consistent with being mainly $Mo_6S_3I_6$ nanowires, but it is clear there are still traces of MoS_2 and excess iodine present, as the determined stoichiometry has higher proportions of sulphur and iodine than the $Mo_6S_3I_6$ stoichiometry. These results concur with sedimentation theory that the pseudospherical MoS_2 impurities would sediment faster than the cylindrical nanowires, hence sediment 1 is observed to mainly contain MoS_2 and sediment 2 is observed to mainly contain $Mo_6S_3I_6$ nanowires. The stoichiometries calculated from the XPS can be compared with the stoichiometries which would be expected from the content of the sediments calculated above. Sediment 1 was determined to be 95% the short phase, which is expected to be the impurity MoS_2, and 5% the long phase, which is expected to be $Mo_6S_3I_6$ nanowires. This would correspond to a stoichiometry of $Mo_6S_{12.3}I_{1.8}$. 91% of sediment 2 was calculated to be the long phase, $Mo_6S_3I_6$ nanowires, with 9% of it being the short phase, MoS_2. This would correspond to a stoichiometry of $Mo_6S_{3.2}I_{5.9}$. There is close agreement between the stoichiometry calculated from the XPS results and the stoichiometry calculated from the sediment contents, further supporting the conclusion that the short phase is MoS_2 and the long phase is $Mo_6S_3I_6$ nanowires.

It is not clear why the nanowires contained in sediment 2 are insoluble while the nanowires contained in the solute can be dispersed. There are two possibilities. It may be that the solubility limit of these nanowires in each solvent governs the amount of stable nanowires. Alternatively, it is possible that the dispersed nanowires are chemically different to the ones that sediment, but it is not clear whether this difference is one of stoichiometry or of surface atomic arrangement.
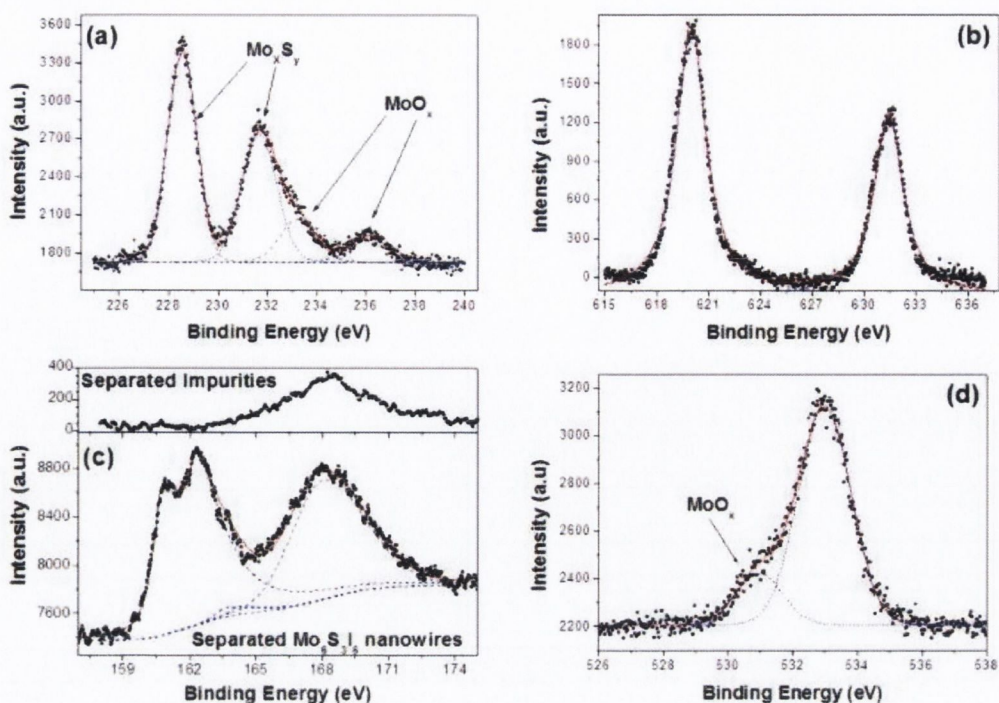
Figure 5.7 - X-ray photoelectron spectra of the stably dispersed material from the DMF separation. Molybdenum 3d spectrum (a), Iodine 3d spectrum (b), Sulphur 2p (c) (and the upper inset is the Sulphur 2p spectrum of the phase 1 material) and the Oxygen 1s spectrum (d). In all of the spectra, the experimental data are points, the experimental fits are shown as solid red lines, and the deconvoluted peaks are shown as dashed blue lines.

A more detailed analysis was performed on the solute XPS data, shown in figure 5.7, during which two pairs of doublets associated with MoS_x (228.6 & 231.7 eV) and MoO_y (233.35 & 236 eV) were identified. These doublets are both due to molybdenum $3d_{5/2}$ and $3d_{3/2}$ spin-orbit splitting. From the analysis of the oxygen spectrum, and after disregarding the peak due to the SiO_2 substrate (533 eV), a peak due to a MoO_y compound was observed leading to the stoichiometry of the compound being determined as $MoO_{3.7}$. This compound was also identified as being formed at between 300 and 500°C during the thermogravimetric analysis (TGA) of the raw material, as previously reported [8]. This compound can be formed by the "roasting" of MoS_2 at atmospheric pressure at temperatures around 315°C [19]. It is likely that this compound was formed as a by-product during the material synthesis or during sonication.

In the sulphur spectrum, several contributions were distinguished. A peak relating to sulphur oxides (168.2 eV), such as sulphates (SO_4^{2-}), sulphides (SO_3^{2-}), sulphur dioxide (SO_2), etc, was identified. A pair of $2p_{5/2}$ and $2p_{3/2}$ spin-orbit split peaks relating to the MoS_x species (160.9 eV & 162.3 eV) and a second pair of $2p_{5/2}$ and $2p_{3/2}$ spin-orbit split peaks relating to S-I species (163.4 & 164.6 eV) was also identified. The sulphur oxides peak corresponds with a peak observed in sediment 1 (inset) showing it was impossible to remove absolutely all impurities after separation. This is also true for the iodine, as the

91

full-width half-maximum of the iodine peaks shows multiple species of iodine are present in the solute, indicating not all of the excess iodine was removed. This is to be expected though, as the sulphur oxides, the iodine and the MoO_3 are all soluble in polar solvents, such as DMF, and therefore would not sediment out with the other impurities. Further washing of the solute material after the separation with a suitable polar solvent should remove these impurities also. Disregarding the SO_x peak at 168.2 eV, the stoichiometry of the solute was calculated to be $Mo_6S_{3.1}I_{7.4}$, which is very close to the predicted stoichiometry of $Mo_6S_3I_6$. Considering that the excess iodine is not accounted for in the previous calculation that 99% of the solute is $Mo_6S_3I_6$ nanowires, this final stoichiometry agrees very well with that prediction. These results show that, besides the iodine and SO_x, there are only trace impurities present in the solute and the purity has been greatly improved from the raw material whose stoichiometry is $Mo_6S_{4.3}I_{11.8}$.

5.3.3 *SEM*

To further analyse the different phases, SEM was performed on dried powders of phase 1 and 2, the solute and the washed raw material. Representative SEM images of each of these are shown in figure 5.8, and the images on the right are all at approximately the same magnification to allow direct comparison. The initial material contains large nanowire bundles, approximately 100 nm in diameter, and large pseudo-spherical impurities. These are also seen in sediment 1, with similar diameters to the nanowires observed in the initial material. Sediment 2 contains smaller nanowire bundles, with diameters of approximately 10 nm, and only few, small impurities. The solute only contains very small bundles relative to the sediments, with many with diameters of approximately 10 nm or smaller visible, and almost no impurities.

Therefore, sedimentation has been demonstrated as an effective method of purifying this material as the SEM images clearly show the impurities and larger diameter nanowire bundles sediment out of solution in a shorter time than the smaller diameter nanowire bundles. From the XPS results, it was shown that the solute contains purified $Mo_6S_3I_6$ nanowires. This simple technique can therefore easily produce stable dispersions of purified $Mo_6S_3I_6$ nanowires in DMF at concentrations of at least 0.06 g L^{-1}. Alternatively, by removing the solvent, the purified $Mo_6S_3I_6$ nanowires can be recovered as a powder and used in further applications, such as polymer composites.

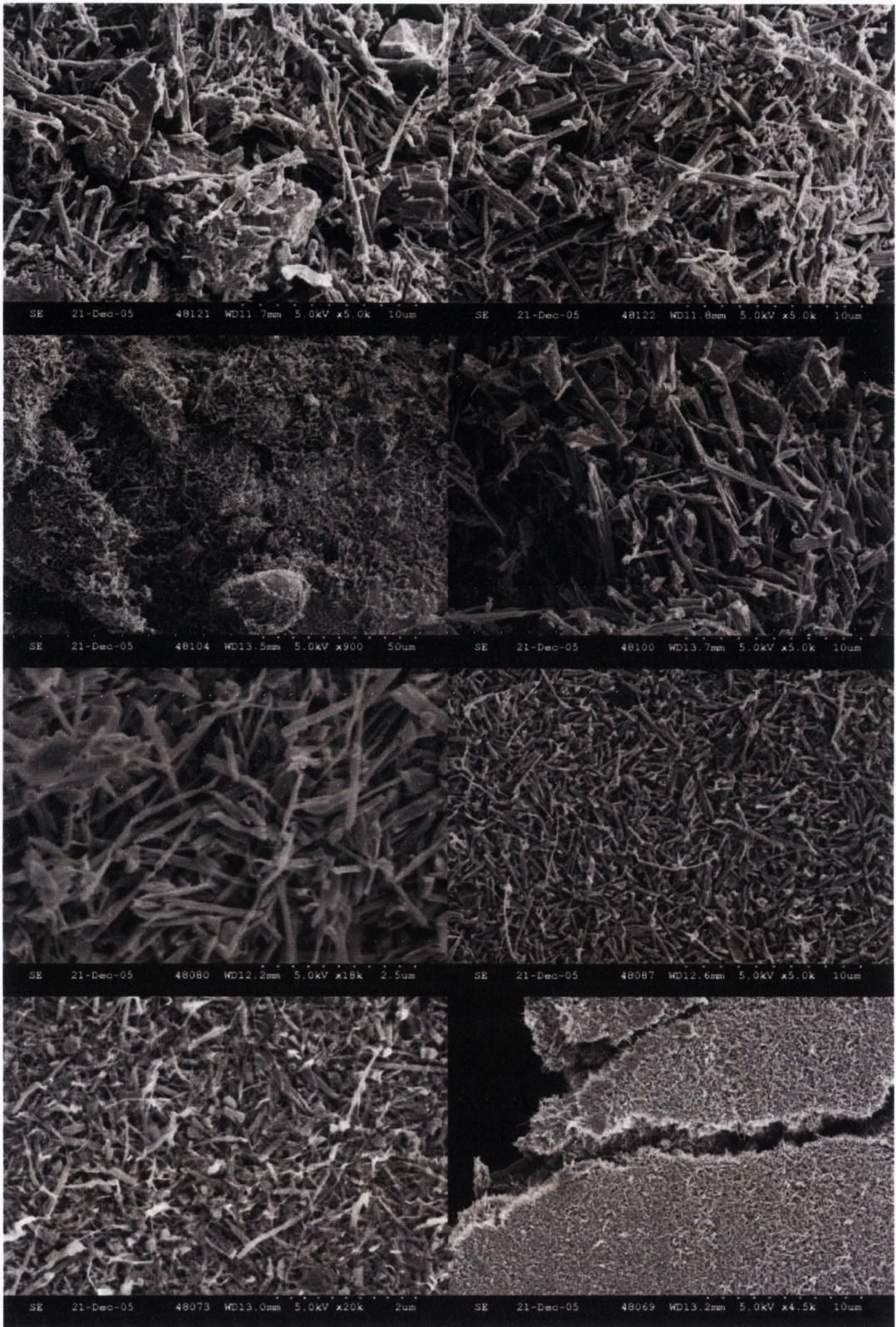Figure 5.8- Scanning electron microscopy images of the washed as-produced $Mo_6S_3I_6$ material (1st row), Sediment 1 (2nd row), Sediment 2 (3rd row) and the Solute (4th row).

5.3.4 *AFM Measurements*

For many applications of nanowires, and single-walled nanotubes (SWNTs), bundles are undesirable as they can reduce the advantageous properties of the material [20, 21]. Some research has suggested alternative methods to overcome this problem for bundles of nanotubes [22], but the main focus is on achieving single nanowires, or SWNTs, for use in applications. Although within each stoichiometry of MoSI nanowires the electronic properties are identical, the higher aspect ratio of the individual nanowires is desirable as it is predicted to lower their percolation threshold [23]. Also, the shear modulus of the MoSI nanowires is quite low [7], making it easy for individual nanowires within bundles to slide relative to each other. This has been observed to weaken SWNT bundles, reducing their Young's modulus to ~80 GPa, below the 100 – 1000 GPa expected [24].
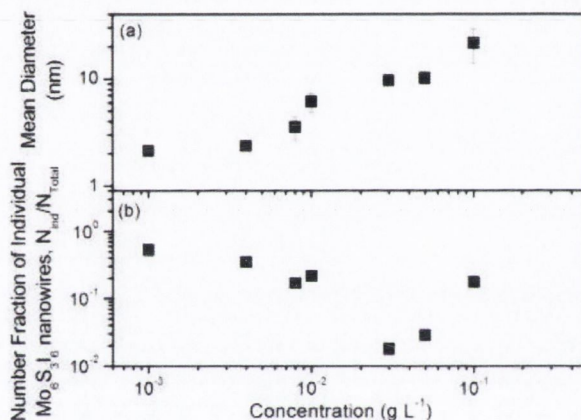
Figure 5.9 - (a) shows the mean diameter of nanowire bundles as a function of concentration as calculated from the diameter distributions measured by AFM. The error bars represent the standard deviation. In (b), the number fraction of individual $Mo_6S_3I_6$ nanowires as a function of concentration as calculated from the AFM measurements is shown.

Previously, the dimensions of the $Mo_6S_3I_6$ nanowires have been measured using TEM, but further measurements were necessary using AFM, as the resolution of the TEM was not sufficient to image individual nanowires. These AFM measurements were performed by Valeria Nicolosi. In performing these measurements, it is important to ensure the dimensions of the nanowires do not become distorted by the AFM measurement. For this reason, the AFM is used in tapping mode with small diameter silicon cantilevers (radius ~ 60 nm). Low force constants (~1 N m^{-1}) are necessary to prevent compression of the nanowires during measurements. Also, only height measurements were used to calculate the bundle diameters, as tip size effects can give excessively large diameters.

The bundle diameters for a range of concentrations of the purified $Mo_6S_3I_6$ solute, from 0.1 g L^{-1} to 0.001 g L^{-1} were measured [20]. The average diameter and standard

deviation as a function of concentration is shown in figure 5.9(a). This plot shows that as the concentration decreases, the average diameter also decreases, until at 0.001 g L^{-1} the average diameter of the nanowires is approximately 2 nm, corresponding to a bundle of two nanowires. From the AFM measurements, the number fraction of individual nanowires can be calculated, as this is the number of individual nanowires (bundles with diameter less than 1.4 nm) divided by the total number of nanowire bundles measured for each sample. This is plotted against concentration in figure 5.9(b), and shows that the number of individual nanowires present is proportional to the concentration. These results also show that individual $Mo_6S_3I_6$ nanowires are present at all concentrations and solutions of mainly individual nanowires are achievable by dilution

5.4 Aligned Nanowires

As shown in section 5.3.3, SEM was performed on dried powders of the different phases. In figure 5.10, four SEM images of a particle of the solute phase that has dried with aligned nanowires are shown. In figure 5.10(a), the particle is visibly different from the others as it is brighter. In figure 5.10(b), the surface appears to be stratified layers, but at higher magnification, it can be seen that this is actually a surface of nanowires aligned preferentially in the direction indicated by the arrow in figure 5.10(c). The mechanism causing this alignment is not known, although evaporation induced alignment of carbon nanotubes has been observed previously by Song et al. [25]. In their work, nematic liquid crystal behaviour was observed and above a critical nanotube concentration (~4.3%) the nematic nuclei joined to give large regions of alignment in the dispersion and in the dried material also. As this material was subjected to extensive sonication and allowed to stand for 600 hours, it is not possible for the dried aligned nanowires to be a remnant of the raw material and must have been formed during drying of the solute material. Similarly to the carbon nanotube system previously reported, it may be a localised alignment occurring at a nematic nuclei and larger scale alignment could be observed at higher concentrations. No other particles of aligned nanowires were observed, so it is not possible to determine the actual mechanism.

The particle is approximately 60 μm wide and 200 μm long and difference in brightness is due to preferential scattering of the electrons towards the detector by the aligned surface. This would indicate that the entire surface, and possibly the bulk, is highly aligned. To be able to achieve this degree of alignment with such large quantities of nanowires could lead to new and useful applications.
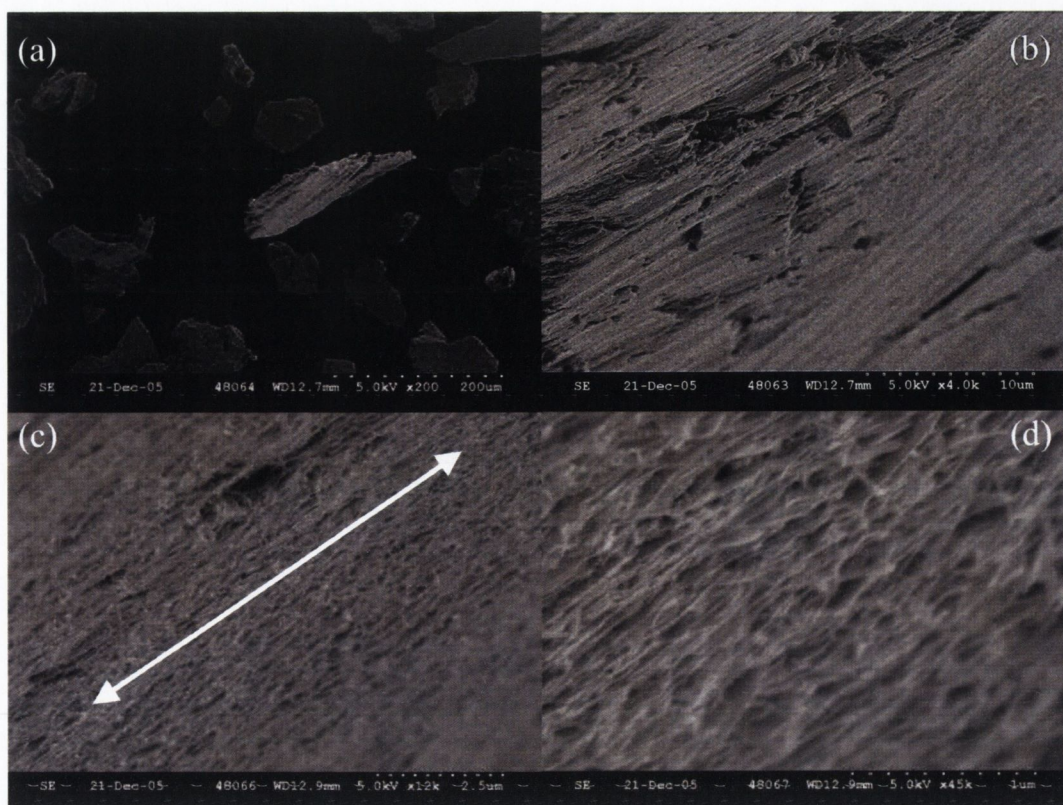
Figure 5.10 – Scanning electron microscopy images of aligned $Mo_6S_3I_6$ nanowires observed in the solute after drying. The direction of alignment is indicated in (c) by the white arrow.

5.5 Conclusions

The local effective concentration of dispersions of washed $Mo_6S_3I_6$ raw material was measured as a function of time in several common solvents during the sedimentation of insoluble material. By fitting this data to the theory, it was calculated that for all solvents, except DMSO, two sedimenting phases and one stable phase were identified in the $Mo_6S_3I_6$ material (for DMSO, the best fit was one sedimenting and one stable phase). From the fit parameters and the TEM images, DMF was determined to be the best solvent for the $Mo_6S_3I_6$ material, followed by acetone. These solvents stably disperse significantly larger amounts of the $Mo_6S_3I_6$ material than the other solvents and almost no impurities. Transmission electron microscopy was performed on these dispersions before sedimentation, after sedimentation and on the sediment after sedimentation. It was observed that the dispersions after sedimentation contained smaller diameter nanowire bundles than the dispersions before sedimentation. Stable dispersions of the nanowire material in DMF at concentrations of approximately 0.06 g L^{-1} were observed, making DMF an effective solvent and sedimentation an effective purification method.

The two sediment phases and the stably dispersed material were separated and analysed using UV-vis-IR spectroscopy, SEM, and XPS. From the SEM it was observed

that the washed raw $Mo_6S_3I_6$ material contained large diameter nanowire bundles and large amounts of impurities. Sediment 1 contained some nanowire bundles and large quantities of impurities. Sediment 2 contained smaller nanowire bundles and some impurities, and the soluble phase contained almost no impurities and very small nanowire bundles. This agrees very well with sedimentation theory predictions that high aspect ratio particles (nanowire bundles) will have a higher frictional coefficient than spherical particles (impurities). This would result in impurities sedimenting from solution faster than the nanowires, as is observed by the lack of impurities in sediment 2 and the soluble phase.

Although, there were no differences observed in the ultraviolet and visible regions of the UV-vis-IR spectra of the four samples, a peak was clearly observed at 0.64 eV in the near IR region for both the soluble phase and sediment 2, that was not observed in either sediment 1 or the washed raw material. As observed from SEM, the soluble phase and sediment 2 are mainly small diameter nanowire bundles, and are significantly different from the other two samples. This peak can therefore be associated with the purified nanowires, which further supports the predictions of sedimentation theory.

From the XPS of the different samples, the stoichiometries were calculated. The stoichiometry calculated for the three separated phases were $Mo_6S_{11}I_{0.8}$ for sediment 1, $Mo_6S_{3.5}I_{7.9}$ for sediment 2, and $Mo_6S_{3.1}I_{7.4}$ for the soluble phase. These results confirm the previous findings and agree well with the predictions from sedimentation theory, showing quite clearly that the first sediment is mainly the impurity material MoS_2, and the second sediment contains mainly $Mo_6S_3I_6$ nanowires and some traces of impurities. Although some traces of DMF soluble impurities, such as molybdenum trioxide and some sulphur oxides were identified, the soluble phase stoichiometry is consistent with being almost completely $Mo_6S_3I_6$ nanowires and approximately 12% by mass excess iodine. These impurities and the iodine could be removed by washing with an alternative solvent.

These results demonstrate the ease with which the $Mo_6S_3I_6$ nanowires can be stably dispersed in certain solvents and at relatively high concentrations. This, combined with their monodisperse electronic structure and high Young's modulus, makes them more attractive for applications than carbon nanotubes. The simple, one-step synthesis of these nanowires, which can easily be scaled up, also gives them a significant advantage. These properties of the $Mo_6S_3I_6$ nanowires suggest a wide range of future applications for this material.

5.6 References

[1]   L. Joly-Pottuz, F. Dassenoy, J. M. Martin, D. Vrbanic, A. Mrzel, D. Mihailovic, W. Vogel, and G. Montagnac, Tribology Letters 18 (2005) 385.

[2]   R. Murphy, V. Nicolosi, Y. Hernandez, D. McCarthy, D. Rickard, D. Vrbanic, A. Mrzel, D. Mihailovic, W. J. Blau, and J. N. Coleman, Scripta Materialia 54 (2006) 417.

[3]   M. Zumer, B. Zajec, N. Vincenc, Z. Bojan, R. Maja, P. Mihaela, V. Damjan, M. Ales, and M. Dragan, Nanotechnology 16 (2005) 1619.

[4]   R. H. Baughman, A. A. Zakhidov, and W. A. de Heer, Science 297 (2002) 787.

[5]   Y. Xia, P. Yang, Y. Sun, Y. Wu, B. Mayers, B. Gates, Y. Yin, F. Kim, and H. Yan, Advanced Materials 15 (2003) 353.

[6]   A. B. Greytak, L. J. Lauhon, M. S. Gudiksen, and C. M. Lieber, Applied Physics Letters 84 (2004) 4176.

[7]   Mo6 d.o.o., http://www.mo6.com (2007)

[8]   D. Vrbanic, M. Remskar, A. Jesih, A. Mrzel, P. Umek, M. Ponikvar, B. Jancar, A. Meden, B. Novosel, S. Pejovnik, P. Venturini, J. C. Coleman, and D. Mihailovic, Nanotechnology 15 (2004) 635.

[9]   A. Meden, A. Kodre, J. Padeznik Gomilsek, I. Arcon, I. Vilfan, D. Vrbanic, A. Mrzel, and D. Mihailovic, Nanotechnology 16 (2005) 1578.

[10]   S. Giordani, S. D. Bergin, V. Nicolosi, S. Lebedkin, M. M. Kappes, W. J. Blau, and J. N. Coleman, Journal of Physical Chemistry B 110 (2006) 15708.

[11]   C. A. Furtado, U. J. Kim, H. R. Gutierrez, L. Pan, E. C. Dickey, and P. C. Eklund, Journal of the American Chemical Society 126 (2004) 6095.

[12]   B. J. Landi, H. J. Ruf, J. J. Worman, and R. P. Raffaelle, Journal of Physical Chemistry B 108 (2004) 17089.

[13]   V. Nicolosi, D. Vrbanic, A. Mrzel, J. McCauley, S. O'Flaherty, C. McGuinness, G. Compagnini, D. Mihailovic, W. J. Blau, and J. N. Coleman, Journal of Physical Chemistry B 109 (2005) 7124.

[14]   V. Nicolosi Ph.D. Thesis, in the School of Physics, Trinity College Dublin, Ireland, 2006.

[15]   V. Nicolosi, P. Nellist, S. Sanvito, E. Cosgrave, S. Krishnamurthy, W. J. Blau, M. Green, J. Sloan, D. Vengust, D. Dvorsek, D. Mihailovic, G. Compagnini, V. Stolojan, D. J. Carey, and J. N. Coleman, Submitted to Advanced Materials (2006)

[16]   V. Nicolosi, D. Vrbanic, A. Mrzel, J. McCauley, S. O'Flaherty, D. Mihailovic, W. J. Blau, and J. N. Coleman, Chemical Physics Letters 401 (2005) 13.

[17]   P. W. Atkins, Physical Chemistry, 4th edition, Oxford University Press, 1992.

[18]   A. Meden, A. Kodre, J. Padeznik Gomilsek, I. Arcon, I. Vilfan, D. Vrbanic, A. Mrzel, and D. Mihailovic, Nanotechnology 16 (2005) 1578.

[19]   G. Leichtfried, Ullmans Encycopedia of Industrial Chemistry, Wiley, 1990.

[20]   V. Nicolosi, D. N. McCarthy, D. Vengust, D. Mihailovic, W. J. Blau, and J. N. Coleman, European Physical Journal - Applied Physics 37 (2007) 149.

[21]   J.-P. Salvetat, G. A. D. Briggs, J.-M. Bonard, R. R. Bacsa, A. J. Kulik, T. Stöckli, N. A. Burnham, and L. Forró, Physical Review Letters 82 (1999) 944.

[22]   A. Kis, G. Csanyi, J. P. Salvetat, T.-N. Lee, E. Couteau, A. J. Kulik, W. Benoit, J. Brugger, and L. Forro, Nature Materials 3 (2004) 153.

[23]   E. J. Garboczi, K. A. Snyder, J. F. Douglas, and M. F. Thorpe, Physical Review E 52 (1995) 819.

[24]   J. N. Coleman, U. Khan, W. J. Blau, and Y. K. Gun'ko, Carbon 44 (2006) 1624.

[25]   W. Song, I. A. Kinloch, and A. H. Windle, Science 302 (2003) 1363.

CHAPTER 6

Characterisation of MoSI Nanowire/Composites

6.1 Introduction

The use of carbon nanotubes as filler materials in polymers has mainly been focussed on electrical conductivity improvements and mechanical reinforcement, and to a lesser degree, thermal conductivity. As yet, very little research has been done on alternative one-dimensional filler materials, such as the MoSI nanowires, which have similar physical properties to carbon nanotubes [1], but have advantages such as simple synthesis and uniform electronic structure, amongst others.

In the previous chapter, the dispersion properties of the $Mo_6S_3I_6$ nanowire material were studied. These properties demonstrate it as an alternative to carbon nanotubes for many applications. After having identified the best solvent for the $Mo_6S_3I_6$ material as N,N-dimethylformamide (DMF) and developing a simple purification technique, this information can be applied to the preparation of composites based on $Mo_6S_3I_6$ nanowires. PMMA, a common thermoplastic used in a variety of applications, was chosen as a polymer compatible with DMF for the composite work.

In a previous study, composites had been prepared with PMMA and $Mo_6S_{4.5}I_{4.5}$ nanowires which had a remarkably low percolation threshold [2]. Here, a similar electrical study was performed to determine the suitability of $Mo_6S_3I_6$ for use in conductive composites and for comparison with the $Mo_6S_{4.5}I_{4.5}$ nanowires.

The mechanical properties of MoSI nanowire/PMMA composites are also investigated here to ascertain the effect of the fillers on the polymer matrix. A large amount of research has focussed on the reinforcement of polymers with carbon nanotubes [3-7] to produce strong, lightweight materials. Very little research has been reported for the reinforcement of polymers with inorganic nanowires, except for Vivekchand et al. [8] who claim to be the only publication so far on this subject and their work is also discussed here.

6.2 Electrical Measurements

6.2.1 *Annealed $Mo_6S_3I_6$ material*

Previously it was shown by Berčič et al. that annealing of the raw $Mo_6S_3I_6$ material to remove the excess iodine, as an alternative to washing with acetone, caused an increase in the conductivity of the nanowire material from 0.04 S m^{-1} to 0.2 S m^{-1} [9]. For this

study, $Mo_6S_3I_6$ was annealed at 800 °C prior to composite production, as the higher conductivity is expected to improve the performance of the composites. The conductivity of this annealed material was then measured for the powder and for a buckypaper prepared by vacuum filtration of a dispersion of $Mo_6S_3I_6$ in DMF. A sedimentation study of the annealed $Mo_6S_3I_6$ material in DMF was also performed and it is shown in figure 6.1. The results are compared with the washed $Mo_6S_3I_6$ and the unwashed $Mo_6S_3I_6$ material, as presented in greater detail in chapter 5.
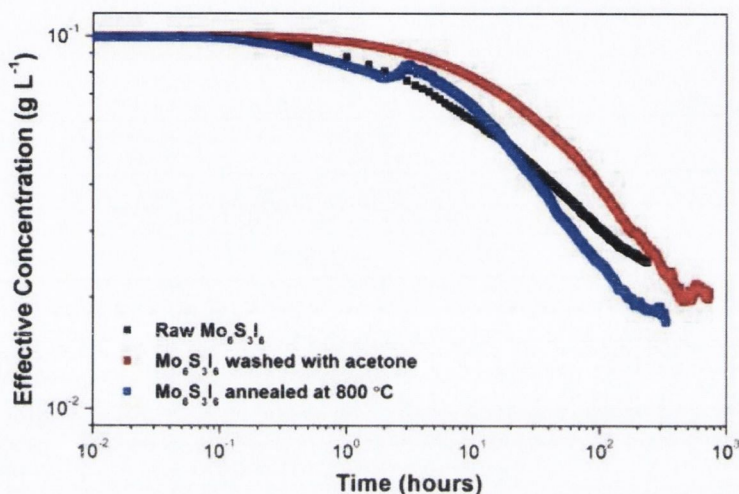
Figure 6.1 - Experimental sedimentation curves for 0.1 g L⁻¹ dispersions of the as-produced, the washed and the annealed $Mo_6S_3I_6$ nanowire bundles in DMF for comparison.

From these sedimentation curves, it is clear the three materials do behave differently. Overall the variation between them is small compared to the variation between different solvents for the washed $Mo_6S_3I_6$ material. The annealed DMF data was fitted with a bi-exponential decay, as done previously for the washed and unwashed data, and the parameters from all these fits are presented in table 6.1, allowing comparison of the different materials.

In previous sedimentation work with the unwashed $Mo_6S_3I_6$, the dispersions were observed to gradually become yellow, indicating that iodine was slowly leaching into the solvent from the nanowire material over the course of the sedimentation. For the washed and the annealed $Mo_6S_3I_6$ material, the solutions remained a transparent grey throughout the sedimentation study. Although the stoichiometry calculated from the XPS in chapter 5 does show that a small amount of iodine remains in the washed material. As observed for the acetone from the washing procedure, iodine solutions absorb in the visible region and therefore the amount of stably dispersed material, $C_{eff,0}$, is likely to be exaggerated. The effect would be strongest for the unwashed $Mo_6S_3I_6$ which has the most iodine present and this would suggest the differences between the amounts of material remaining stably

dispersed, $C_{eff,0}$, as listed in table 6.1, are probably negligible. The differences between the content of each batch prepared would also lead to variation in the effective concentrations.

Fit Parameter	Raw $Mo_6S_3I_6$	Washed $Mo_6S_3I_6$	Annealed $Mo_6S_3I_6$
$C_{eff,0}/C_{Total}$	0.25	0.20	0.18
$C_{eff,1}/C_{Total}$	0.37	0.34	0.43
τ_{short} (hours)	3.7	13.6	10.7
$C_{eff,2}/C_{Total}$	0.37	0.46	0.35
τ_{long} (hours)	51.9	122.2	58.3

Table 6.1 – Comparison of fit parameters for the sedimentation studies of as-produced, the washed and the annealed $Mo_6S_3I_6$ nanowire bundles in DMF.

As stated in chapter 5, the time constants for each phase are expected to remain constant between samples irrespective of the amount of each phase present, if the dimensions of the impurities and the bundles are not affected. The long time constant, τ_{long}, of the unwashed and the annealed material are quite similar, whereas the washed material's time constant is approximately twice these values. This could be due to the repeated sonication involved in the washing procedure which would break up the bundles allowing iodine trapped in them to be dissolved. For the annealed nanowires, it would be more difficult for the iodine trapped in the nanowire bundles to be removed. Therefore larger bundles bound together by iodine would exist in both the unwashed and the annealed material which would sediment faster from the solution and would explain the smaller time constants. The effectiveness of the annealing at removing iodine could also explain the short time constant for phase 1, τ_{short}, of the annealed material, as more iodine remains in the MoS_2 impurities also. From the time constants, the washing procedure is the most effective at removing the excess iodine from the nanowire bundles and the MoS_2 impurities. The annealing procedure is almost as effective at removing iodine from the MoS_2 impurity particles, but has little effect at removing the excess iodine from the nanowire bundles. The mechanism by which the annealing improves the conductivity could therefore be the reduction in size of the insulating MoS_2 impurities, allowing closer packing of the $Mo_6S_3I_6$ nanowires when they are compacted into a pellet and thus greater contact between them.

6.2.2 Conductivity of the Annealed Mo$_6$S$_3$I$_6$

Before the electrical analysis of the Mo$_6$S$_3$I$_6$ composites, the conductivity of the nanowire material was measured. Although previous reports had stated a conductivity of 0.2 S m^{-1}, this was measured for a compacted pellet of the material. A more suitable morphology for comparison with the situation in a composite would be a loose powder, as is measured here. A buckypaper was also prepared of the annealed Mo$_6$S$_3$I$_6$ material and the conductivity of this was measured.

For the powder conductivity measurement, the conductances of several different weighed masses of the annealed Mo$_6$S$_3$I$_6$ powder were measured. The powder was confined in a cavity of known area and the height of the powder in the cavity was measured, allowing an average conductivity of ~10^{-3} S m^{-1} to be calculated for the powder. The volume of the powder in the cavity could also be calculated and hence its density. The calculated densities of the powder, which range from 4244 kg m^{-3} to 1479 kg m^{-3}, compared to the theoretical density of the Mo$_6$S$_3$I$_6$ nanowires of 5100 kg m^{-3} [1], indicate that the majority of the cavity volume is free space due to the loose packing of the material. From the powder density, the volume fraction of nanowires in the cavity was determined and hence the average conductivity of the nanowires was calculated to be ~10^{-2} S m^{-1}.

For conductivity measurements of the buckypaper sample, a strip 1.0 cm long and 2.0 mm wide was cut from the teflon filter paper after vacuum. This is shown in figure 6.2. From the mass of the Mo$_6$S$_3$I$_6$ material used, its theoretical density and the area of the film, the thickness of the buckypaper film was calculated to be 12 μm. The resistance of this strip was measured to be approximately 80 MΩ, giving a conductivity for the nanowire material of ~5 × 10^{-3} S m^{-1}, agreeing with the results from the powder conductivity measurement.

1 cm
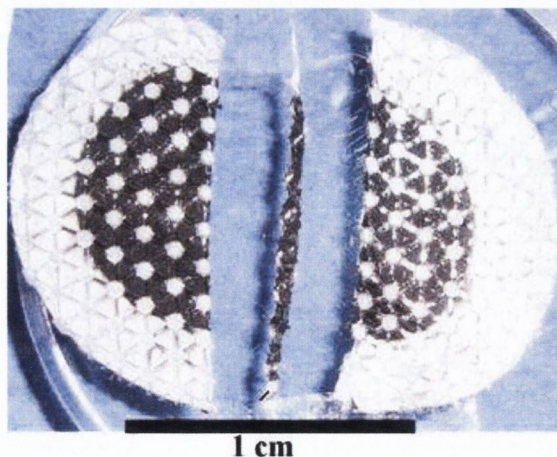
Figure 6.2 – The filter paper used to prepare the buckypaper of the annealed Mo$_6$S$_3$I$_6$. The black material visible is the Mo$_6$S$_3$I$_6$ material. The white holes are due to the pores in the filter paper. The strip in the centre was used for the conductivity measurement.

6.2.3 *Electrical Measurements of Composites*

As with the MWNT/First Contact composites, the first electrical measurement performed on the composites was impedance spectroscopy. Similar to the previous study for the $Mo_6S_{4.5}I_{4.5}$ nanowire material, a low percolation threshold is expected for the $Mo_6S_3I_6$/PMMA composites. From the raw material conductivity measurement, the conductivity of the composites would not be expected to be as high as the 4×10^{-3} S m^{-1} observed previously for the $Mo_6S_{4.5}I_{4.5}$ composites [2], as this is approximately equal to the $Mo_6S_3I_6$ nanowires alone.

The electric modulus, $|\sigma*(\omega)|$, plotted as a function of frequency, is shown in figure 6.3. From this graph, it can be seen that three of the electrodes behave as pure dielectrics as their slopes are unity. The other three only conduct at very low frequencies, below 1 kHz. Also, electrode 2 shows a maximum conductivity of $\sim 10^{-5}$ S m^{-1}, whereas the other electrodes all exhibit conductivities below 10^{-6} S m^{-1}. The D.C. I-V characteristics were also measured for this film and the calculated conductivities are in good agreement with the electric moduli at low frequency in figure 6.3. This gives an average D.C. conductivity, σ_{DC}, for the annealed $Mo_6S_3I_6$/PMMA film of 1.6×10^{-6} S m^{-1}. This is a surprisingly low result compared to the previous results for the $Mo_6S_{4.5}I_{4.5}$ nanowires, as the volume fraction of this film is approximately equal to the highest volume fraction in that study, 0.027, which had a conductivity of 4×10^{-3} S m^{-1}. The volume fraction of the film is also far above the percolation threshold, ϕ_c, measured there, of 1.3×10^{-5}, which would imply a higher conductivity.
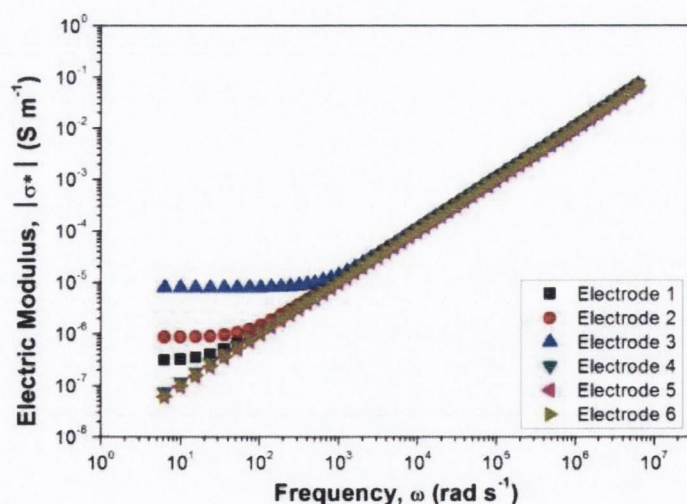
Figure 6.3 – Electric modulus, $|\sigma*(\omega)|$, plotted as function of frequency, ω, for the 6 electrodes on the $Mo_6S_3I_6$/PMMA film. All behave as dielectrics at high frequencies, but some show signs of conduction below 1 kHz.

It is not clear why the conductivity of these composite films is so low, especially when compared to the previous performance of the $Mo_6S_{4.5}I_{4.5}$/PMMA composites. It is

possible that polymer wrapping around the nanowires has insulated them from each other creating large conduction barriers. The $Mo_6S_3I_6$ nanowires clearly under-perform when compared to the $Mo_6S_{4.5}I_{4.5}$ nanowires, which is a surprising result.

6.3 Mechanical Measurements

Prior to the research on the $Mo_6S_3I_6$ nanowires presented in this thesis, a significant amount of work had already been done on the $Mo_6S_{4.5}I_{4.5}$ nanowire material [2, 10, 11], including an electrical study. Thin film (3 – 4 μm) composites of $Mo_6S_{4.5}I_{4.5}$ in PMMA were prepared that had conductivities as high as 4×10^{-3} S m^{-1} at a volume fraction of 0.027, sufficient for electrostatic dissipation and electrostatic painting [12], and with a very low percolation threshold of 1.3×10^{-5}. This demonstrates the potential of $Mo_6S_{4.5}I_{4.5}$ nanowire composites for electrical applications and demonstrates a significant advantage over the $Mo_6S_3I_6$ nanowires. The Young's moduli of the $Mo_6S_{4.5}I_{4.5}$ and $Mo_6S_3I_6$ nanowires are stated as ~400 GPa [1], suggesting them as filler materials for reinforcement of polymers. Due to the larger quantity of $Mo_6S_{4.5}I_{4.5}$ material available and because the $Mo_6S_{4.5}I_{4.5}$/PMMA composites have been demonstrated as suitable for electrical applications, the mechanical properties of $Mo_6S_{4.5}I_{4.5}$/PMMA composites will be measured here to ascertain the effect of their presence on the composite.

6.3.1 *Mechanical Results*

From the original masses used in the preparation, less the mass of the nanowire sediment after decantation, the volume fraction of the nanowires in the highest concentration composite film used for tensile testing was calculated to be 0.012. The other films were prepared by dilution of this composite solution with a PMMA stock solution (30 g L^{-1}), allowing the volume fractions of the other composites to be calculated. The range of volume fractions prepared is 3.6×10^{-4} to 1.2×10^{-2}.

For each of the $Mo_6S_{4.5}I_{4.5}$/PMMA volume fractions, four strips were tested at an extension rate of 1.5 mm/min. From the stress-strain curves, the Young's modulus, Y, tensile strength, σ_T, toughness and strain at break, ε_B were calculated and the average values for each volume fraction are plotted in figure 6.4 with the standard deviation shown as the error. The data shows that the introduction of the $Mo_6S_{4.5}I_{4.5}$ nanowires into the PMMA matrix has little effect on the tensile strength or the strain at break of the polymer. At low volume fractions, there is some variation in these values, but the general trend is that they stay approximately constant over all the volume fractions measured. For the toughness, there is a similar initial scatter in the data at low volume fractions, but above

105

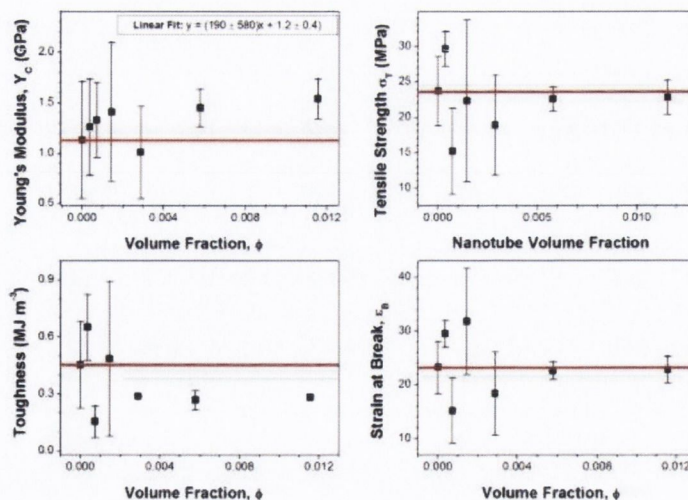1.4 $\times 10^{-3}$ the toughness of the composites has been reduced to approximately 60 % of the polymer value.

Figure 6.4 – The average Young's modulus, Y, tensile strength, σ_T, toughness and strain at break, ε_B, plotted as a function of volume fraction for the $Mo_6S_{4.5}I_{4.5}$ nanowire/PMMA composites. The red lines indicate the value measured for the pure polymer.

For the Young's modulus, as shown in figure 6.4, there is a continuous increase in the average Young's modulus of the composites as the volume fraction of $Mo_6S_{4.5}I_{4.5}$ nanowires increases from 1.1 GPa for the pure polymer, up to 1.4 GPa for a composite volume fraction of 1.4×10^{-3}. Above this volume fraction, the average Young's modulus remains approximately constant up to highest volume fraction tested, $\phi = 0.012$. The error in the Young's modulus of the lowest volume fractions is quite significant making these increases uncertain. It does appear that the presence of the nanowires does not cause any significant decrease in the measured mechanical properties except for the toughness.

The majority of reports of reinforcement involve carbon nanotubes as the filler material. The only report of nanowires being used as reinforcement, to the author's knowledge, is by Vivekchand et al., where they used SiC and Al_2O_3 nanowires in PVA and measured the mechanical propertied by tensile testing. There have also been several studies on the mechanical properties of carbon nanotube/PMMA composites.

In Vivekchand et al. [8], they describe the mechanical properties of PVA with two different inorganic nanowire materials. From the dynamic scanning calorimetry (DSC) measurements, a small increase in polymer crystallinity with increasing SiC nanowire content was observed, a maximum of ~1.1 % for a volume fraction of 0.008. For the Al_2O_3 nanowires an increase in crystallinity of 4.5 % was observed for the 0.004 volume fraction. This increase in crystallinity will have a significant effect on the enhancement of the mechanical properties. As PMMA is amorphous, this makes direct comparisons difficult, however the smaller increase for the SiC nanowires, as well as the larger amount of data

presented for them, does allow some comparison. Unlike the $Mo_6S_{4.5}I_{4.5}$ nanowires where no real change in strength was observed, the addition of SiC nanowires does result in an increase in the ultimate tensile strength of the composite from ~70 MPa for the polymer to a maximum of ~120 MPa for the 0.004 volume fraction composite. The presence of the Al_2O_3 nanowires resulted in a similar increase. Above this volume fraction, the strength approximately plateaued. The increase in Young's modulus with volume fraction, from 3.2 GPa for the polymer to 6.1 GPa for the 0.008 volume fraction composite, gives a reinforcement, $dY/d\phi$, of 360 GPa for the SiC nanowires. For the Al_2O_3 nanowires an increase to 5.1 GPa was observed for a volume fraction of 0.004, giving a reinforcement of 475 GPa, but with a 4.5 % increase in crystallinity compared to the 1.1 % for the SiC nanowires. These results are equal or better than the increase observed for the majority of MWNT/PVA composites as reported by Coleman et al. [4], except for low diameter MWNTs. This demonstrates that inorganic nanowires can perform as well, or better than the majority of carbon nanotubes for polymer reinforcement.

Although no increase in Young's modulus was observed for the $Mo_6S_{4.5}I_{4.5}$ nanowires in PMMA, the work by Vivekchand et al. does demonstrate that nanowires are a potential alternative for composite reinforcement. It is possible that with further work on the $Mo_6S_{4.5}I_{4.5}$ nanowires reinforcement could be achieved, as well as the previously observed increase in electrical conductivity.

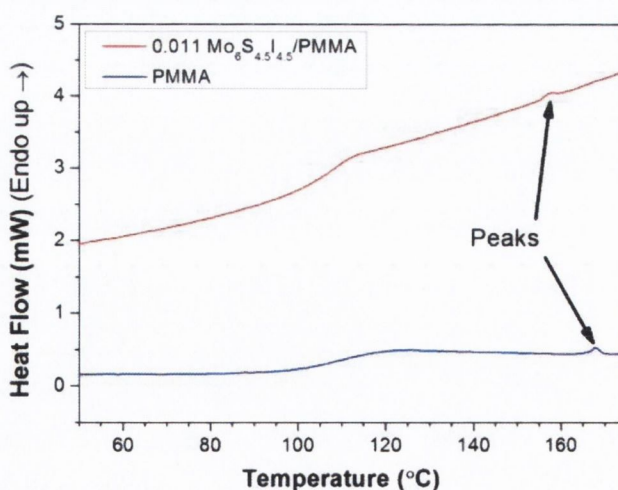Figure 6.5 –The 2nd heat DSC curves for the PMMA (blue) and the highest volume fraction $Mo_6S_{4.5}I_{4.5}$/PMMA composite (red). The T_g can be seen near 105 °C and a peak can be seen in both curves at 158 °C for composite and 168 °C for the PMMA.

107

6.3.2 Dynamic Scanning Calorimetry

Dynamic scanning calorimetry (DSC) was performed on the highest $Mo_6S_{4.5}I_{4.5}$ nanowire volume fraction composite and on the raw PMMA in the temperature range from -60 °C to 200 °C to determine the morphology of the composites. Only the relevant temperature range, ~50 °C to ~180 °C, where the glass transition and a melting peak are observed is shown below in figure 6.5. Outside of this range no thermal transitions were observed.

For the PMMA polymer the glass transition, T_g, appears at 110 °C and for the composite it appears at the slightly lower temperature of 105 °C. The T_g of PMMA is quoted as 104 °C [13], although several factors can cause it to vary. The glass transition measured here agrees very well with the quoted value, demonstrating the $Mo_6S_{4.5}I_{4.5}$ nanowires have little effect on the bulk polymer. In both curves a peak was observed at higher temperatures where a melting peak would be expected for semi-crystalline polymers, but PMMA is completely amorphous. For the polymer itself, the peak is at 168 °C and has an area of 0.33 J g^{-1}. For the composite, the peak is observed at 158°C and has an area of 0.12 J g^{-1}. The peaks are both quite small and possibly not too significant as no melting peak should be observed in the PMMA.

6.3.3 Scanning Electron Microscopy

Scanning electron microscopy was performed on strips used in tensile testing of the highest (0.011) and lowest (3.6×10^{-4}) volume fraction composites for comparison. The surfaces of the films far from the failure point and at the fracture surface were examined. Examples of the surface of the bulk of the film are shown in figure 6.6. The surface of the lowest volume fraction film is quite rough, whereas the surface of the highest volume fraction film appears quite smooth and this remains true at higher magnifications.
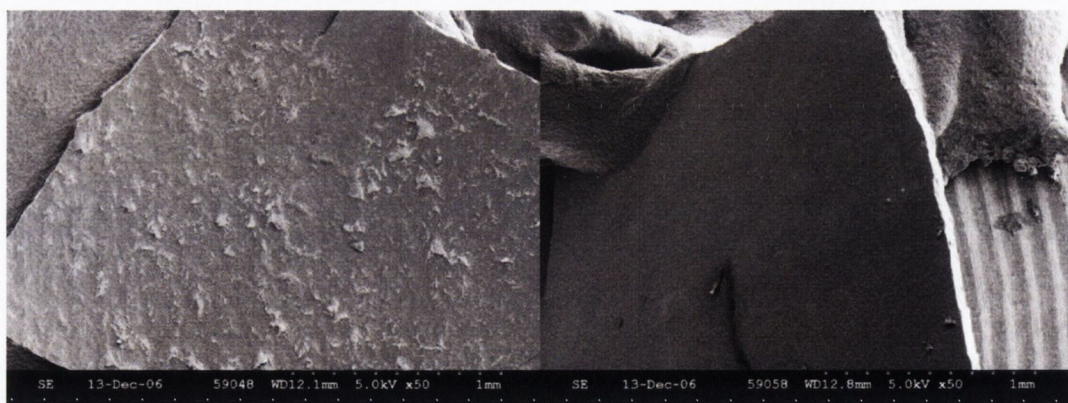

Figure 6.6 – SEM images of the film surfaces far from the failure point for the lowest, 3.6×10^{-4} volume fraction (left) and the highest, 0.011 volume fraction (right) $Mo_6S_{4.5}I_{4.5}$/PMMA composites.

The images of the fracture surfaces for both composites are shown in figure 6.7. They look quite similar in the lower magnification images (bottom row). At higher magnifications differences are more visible, with the roughness at the fracture surface appearing at a lower scale for the high volume fraction composite compared to the lowest volume fraction composite. For both composites, no nanowires were observed either on the surface of the bulk film or at the fracture surface. Generally, nanowires or nanotubes seen protruding from fracture surfaces are "pulled out" during the fracture process. The lack of nanowires observed here protruding from the surface could indicate weak bonding between the nanowires which would allow a much easier break at the polymer-nanowire interface before "pull-out" occurred. This weak bonding would explain why no significant increase in the Young's modulus of the composites was observed.
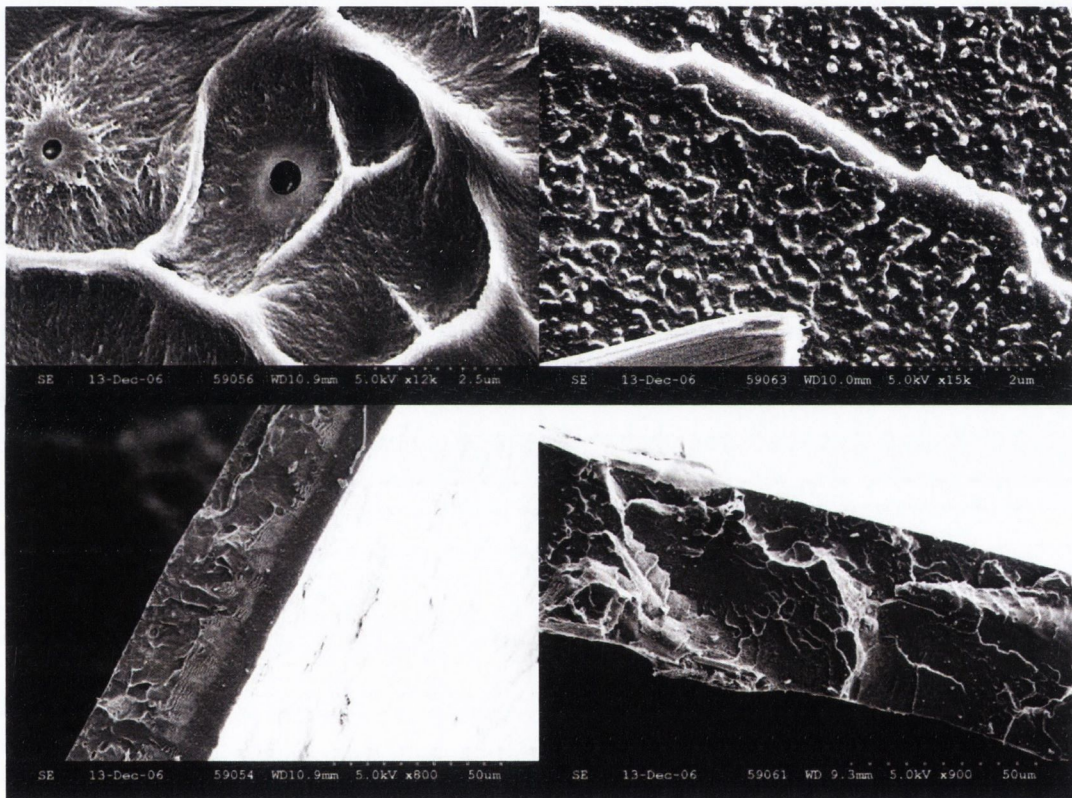
Figure 6.7 - SEM images of the fracture surfaces of the lowest, 3.6×10^{-4} volume fraction (left) and the highest, 0.011 volume fraction (right) $Mo_6S_{4.5}I_{4.5}$/PMMA composites. No nanowires were visible protruding from the surface after fracture.

Good dispersion of the nanowires within the matrix would make observation of nanowires difficult, as the average bundle sizes of well dispersed nanowires observed previously could be below 10 nm [10]. This is below the resolution of the SEM used for these measurements. The diameter of the individual nanowires is 0.94 nm [14], but it is unlikely that the majority of the nanowires are isolated as the maximum amount of nanowires observed as individuals previously is half of all the nanowires present, but this was at the low concentration of 4×10^{-3} g L^{-1} [15].

109

6.4 Conclusions

The electrical properties of $Mo_6S_3I_6$ nanowire/PMMA composites were measured at a relatively high volume fraction of 0.023. The addition of $Mo_6S_3I_6$ nanowires to the PMMA resulted in a limited improvement in the properties of the composite compared with the results previously for the $Mo_6S_{4.5}I_{4.5}$ nanowires. Increased conductivity was observed, from 10^{-11} S m^{-1} for the pure PMMA to the low value of ~10^{-6} S m^{-1} for the composite. This is below the limit for many applications [12]. The reason for the low conductivity could be due to the polymer wrapping around the nanowires, hindering contact between the individual nanowires or the bundles. Polymer wrapping around nanotubes has been observed [16] and theoretically modelled [17], and it is likely a similar mechanism could occur for the nanowires. This result is quite unexpected due to the previous study on the closely related $Mo_6S_{4.5}I_{4.5}$ nanowire species [2], which exhibited a low percolation threshold and a sufficiently high conductivity for electrostatic painting and electrostatic dissipation.

Further work was performed with the $Mo_6S_{4.5}I_{4.5}$ nanowire material in PMMA. The mechanical properties of the $Mo_6S_{4.5}I_{4.5}$/PMMA composites were measured, demonstrating that the presence of the nanowires had no significant effect on most of the polymer's properties. A decrease in the toughness to approximately 60% of the pure PMMA value was observed. The only other report of inorganic nanowires used to in composites [8] reported an increase in elastic modulus from 3.2 GPa for the polymer to a maximum of 6.1 GPa for a 0.008 volume fraction composite. That work demonstrates that nanowires are suitable for composite reinforcement.

Overall, the electrical performance of the $Mo_6S_3I_6$ nanowire composites is disappointing compared to the electrical results from the previous $Mo_6S_{4.5}I_{4.5}$ study. The results presented here do demonstrate that this family of nanowires has potential for the reinforcement of composites and it has been previously shown that they can be used to produce electrically conductive composites. Further work is needed on the electrical composites of $Mo_6S_3I_6$ nanowires, as the reasons for their poor performance are not established. It is possible different processing techniques could improve the properties of the $Mo_6S_3I_6$ composites. The $Mo_6S_{4.5}I_{4.5}$ nanowire/PMMA composites have been shown to have reasonably high conductivities, suitable for many applications, and to have a significantly improved Young's modulus at relatively low volume fractions. Therefore, the $Mo_6S_{4.5}I_{4.5}$ has been demonstrated as suitable for producing conductive and reinforced composites. These results, combined with the previously demonstrated simple synthesis

[18] and easy dispersability [10, 19] do demonstrate that the MoSI family of nanowires are a viable alternative to carbon nanotubes.

6.5 References

[1]   Mo6 d.o.o., http://www.mo6.com (2007)

[2]   R. Murphy, V. Nicolosi, Y. Hernandez, D. McCarthy, D. Rickard, D. Vrbanic, A. Mrzel, D. Mihailovic, W. J. Blau, and J. N. Coleman, Scripta Materialia 54 (2006) 417.

[3]   M. Cadek, J. N. Coleman, K. P. Ryan, V. Nicolosi, G. Bister, A. Fonseca, J. B. Nagy, K. Szostak, F. Beguin, and W. J. Blau, Nano Letters 4 (2004) 353.

[4]   J. N. Coleman, U. Khan, W. J. Blau, and Y. K. Gun'ko, Carbon 44 (2006) 1624.

[5]   G. L. Hwang, Y. T. Shieh, and K. C. Hwang, Advanced Functional Materials 14 (2004) 487.

[6]   E. Lahiff, R. Leahy, J. N. Coleman, and W. J. Blau, Carbon 44 (2006) 1525.

[7]   M. A. L. Manchado, L. Valentini, J. Biagiotti, and J. M. Kenny, Carbon 43 (2005) 1499.

[8]   S. R. C. Vivekchand, U. Ramamurty, and C. N. R. Rao, Nanotechnology 17 (2006) S344.

[9]   B. Bercic, U. Pirnat, P. Kusar, D. Dvorsek, D. Mihailovic, D. Vengust, and B. Podobnik, Applied Physics Letters 88 (2006) 173103.

[10]   V. Nicolosi, D. Vrbanic, A. Mrzel, J. McCauley, S. O'Flaherty, C. McGuinness, G. Compagnini, D. Mihailovic, W. J. Blau, and J. N. Coleman, Journal of Physical Chemistry B 109 (2005) 7124.

[11]   L. Joly-Pottuz, F. Dassenoy, J. M. Martin, D. Vrbanic, A. Mrzel, D. Mihailovic, W. Vogel, and G. Montagnac, Tribology Letters 18 (2005) 385.

[12]   R. Ramasubramaniam, J. Chen, and H. Liu, Applied Physics Letters 83 (2003) 2928.

[13]   J. Brandrup and E. H. Immergut, Polymer Handbook, 3rd Edition, Wiley, New York, 1989.

[14]   V. Nicolosi, D. Vrbanic, A. Mrzel, J. McCauley, S. O'Flaherty, D. Mihailovic, W. J. Blau, and J. N. Coleman, Chemical Physics Letters 401 (2005) 13.

[15]   V. Nicolosi, D. N. McCarthy, D. Vengust, D. Mihailovic, W. J. Blau, and J. N. Coleman, European Physical Journal - Applied Physics 37 (2007) 149.

[16]   B. McCarthy, J. N. Coleman, R. Czerw, A. B. Dalton, M. in het Panhuis, A. Maiti, A. Drury, P. Bernier, J. B. Nagy, B. Lahr, H. J. Byrne, D. L. Carroll, and W. J. Blau, Journal of Physical Chemistry B 106 (2002) 2210.

[17]   J. N. Coleman and M. S. Ferreira, Applied Physics Letters 84 (2004) 798.

[18] D. Vrbanic, M. Remskar, A. Jesih, A. Mrzel, P. Umek, M. Ponikvar, B. Jancar, A. Meden, B. Novosel, S. Pejovnik, P. Venturini, J. C. Coleman, and D. Mihailovic, Nanotechnology 15 (2004) 635.

[19] D. N. McCarthy, V. Nicolosi, D. Vengust, D. Mihailovic, G. Compagnini, W. J. Blau, and J. N. Coleman, Journal of Applied Physics 101 (2007) 014317.

CHAPTER 7

Conclusions & Further Work

7.1 Conclusions

For this thesis, composites based on two different one-dimensional nanostructures, multi-walled carbon nanotubes (MWNTs) and MoSI nanowires, were investigated. Research into carbon nanotubes and nanotube composites has been ongoing for a number of years, but major problems such as dispersion and large scale production of nanotubes are still hindering the applications of these composites. More recently, inorganic nanowires have also been investigated as they have many potential advantages over carbon nanotubes in these areas.

The initial work presented here studies thin MWNT composites using a novel polymer, First Contact. Sedimentation measurements of the nanotubes in solutions of the First Contact polymer demonstrated that this polymer is effective at dispersing nanotubes at relatively high concentrations, up to 2.05 g L^{-1}. Thin MWNT/First Contact composite films were then prepared and their mechanical and electrical properties were measured.

The mechanical properties of these composites were analysed by tensile testing. From the results, it was observed that the presence of the carbon nanotubes does somewhat degrade the toughness, the ultimate tensile strength and the breaking strength of the First Contact polymer. The Young's moduli showed no significant change due to the nanotubes. In general, significant reinforcement or degrading of the mechanical properties was not observed and is not desired, as the applications for elastomers rely on their soft, elastic nature. It was important to demonstrate that the MWNTs can be incorporated into the bulk polymer without any negative effects on the mechanical properties of the polymer.

The electrical properties of the MWNT/First Contact composites were also measured. The percolation threshold for the nanotubes was determined to be $(5.0 \pm 0.5) \times 10^{-6}$, with a conductivity prefactor, σ_0, of $(1.3 \pm 22) \times 10^{11}$ and a critical exponent of 2.97 ± 0.27. This percolation threshold is extremely low, less than half the lowest value previously reported of 1.3×10^{-5} for the $Mo_6S_{4.5}I_{4.5}$ nanowires in PMMA. At a volume fraction of 1.3×10^{-4}, still low enough for the composites to be transparent, a conductivity of 0.20 S m^{-1} was measured. Above a volume fraction of 5.2×10^{-3}, the conductivity had reached its maximum of ~1 S m^{-1}, sufficient for applications such as electrostatic painting and electrostatic dissipation. The low critical exponent measured indicates that the

114

conduction barriers in the composite system are relatively small, allowing a low percolation threshold and high conductivities at low volume fractions.

Similarly impressive results with the nanotubes are not easily achieved with most common polymers due to the problems stated previously. Alternative nanostructures have been developed to overcome these problems. All further work was done with one of these promising materials, MoSI nanowires. The sedimentation of the $Mo_6S_3I_6$ nanowire stoichiometry in a range of solvents was studied. By analysis of this sedimentation data, it was shown that there are two sedimenting phases and one stable phase in the $Mo_6S_3I_6$ raw material. It was also shown that DMF is the best solvent for the $Mo_6S_3I_6$ nanowires and that stable dispersions at concentrations as high as 0.06 g L^{-1} can be prepared in DMF.

From the parameters calculated from the sedimentation data it was determined that it would be possible to separate the three phases, two sedimenting and one stable. UV-vis-IR, XPS and SEM were performed on the three phases in order to determine the nature of the individual phases. The results of these techniques clearly showed that the first phase to sediment is mainly pseudospherical MoS_2, an impurity formed in the synthetic step. The second phase to sediment was shown to be mainly larger diameter $Mo_6S_3I_6$ nanowires, which are predicted to sediment more slowly than the impurities by sedimentation theory. Finally, the stable phase was shown to be mainly smaller diameter $Mo_6S_3I_6$ nanowires. From XPS, it was observed that some traces of soluble impurities, sulphur oxides, iodine and molybdenum trioxide, were also present in the stable phase. These impurities could be removed by further washing with an appropriate polar solvent. The dispersion properties and the simple purification method demonstrated for the $Mo_6S_3I_6$ nanowire material, combined with their one-step synthesis and excellent physical properties demonstrates that these nanowires are a better alternative to carbon nanotubes for many applications.

Dispersion in composites has already been described as one of the main problems for carbon nanotubes. The ease of dispersion of MoSI nanowires would make them a good filler material for composites. Composites of the washed $Mo_6S_3I_6$ material with the common polymer PMMA were prepared. At the relatively high volume fraction, $\phi = 0.023$, of $Mo_6S_3I_6$ in the polymer, the maximum conductivity measured for this composite was $\sim 10^{-5}$ S m^{-1}. This was only observed at one region in the sample, it was not a repeatable result. It is possible that the percolation threshold of the $Mo_6S_3I_6$ nanowires in PMMA is above $\phi = 0.023$. This is possibly due to polymer wrapping around the nanowire bundles separating them and preventing conduction through the nanowire network.

The mechanical properties of PMMA with MoSI nanowires was also investigated. As there were greater quantities of $Mo_6S_{4.5}I_{4.5}$ material available and this nanowire stoichiometry had previously been shown to greatly improve the electrical properties of PMMA, composites of $Mo_6S_{4.5}I_{4.5}$/PMMA were prepared for mechanical measurements. The presence of the nanowires in the composite did cause a decrease in toughness of the PMMA to ~60% of the pure polymer value, but the Young's modulus, tensile strength and strain at break were unaffected.

The high conductivity of the MWNT/First Contact composites at very low volume fractions suggest them for a range of applications. Conductive elastomers are used for seals in pipes carrying flammable gases and nanotube/elastomer composites have been shown to work as photo-actuators. The properties of the First Contact polymer - inert, non-toxic, prevents scratching and acts as a barrier to oxygen, sulphur and water vapour – already make it suitable for packaging. With conductivities of ~1 S m^{-1}, this composite material could also be used as anti-static packaging for electronics. Unfortunately, as First Contact is an elastomer the scope of the composites applications are restricted by its lack of mechanical robustness. It could be used as a coating on other plastics to improve their surface conductivities, which would expand its uses.

For applications where conductive, mechanically strong materials are required, alternatives are required to the MWNT/First Contact composites. Most electrically conductive nanotube composites either have low conductivities or require extremely high nanotube loadings. This involves a compromise between the mechanical and processing properties, which are generally poor for high nanotube loadings, or the low conductivities. The MoSI nanowires have been shown to have a percolation threshold almost as low as the MWNT/First Contact system and reasonably high conductivities of 4×10^{-3} S m^{-1} at a volume fraction of 0.023 in a common thermoplastic. The mechanical properties of the polymer used, and the measured electrical properties of the composites show this composite is suitable for use in many more common situations.

7.2 Further Work

The results presented here indicate the potential of nano-composites in general for reinforcement and electrical conductivity. A significant amount of research is focused on these applications using various nanoparticles and a wide range of polymers, but success has been limited so far due to the lack of understanding of the interactions between the polymer, solvent and the nanoparticles involved. This is slowly being overcome and the realisation of the potential of nano-composites is closer to being achieved.

The study on the MWNT/First Contact composites achieved very high conductivities at remarkably low volume fractions. This appears to be due to the nature of the polymer and its interaction with the nanotubes. Further work is needed to fully understand the nature of the polymer-nanotube interaction, which could then lead to similar results being replicated in other polymers allowing conductive composites to be used in a greater range of applications. Also, if this strong interaction could be achieved in semi-crystalline polymers, this could lead to improved reinforcement of the polymers due to the combination of the interaction and increased crystallinity.

Vivekchand et al. have shown that nanowires can be used successfully to reinforce composites. Although the $Mo_6S_{4.5}I_{4.5}$ nanowires did not demonstrate mechanical reinforcement in this work, it is possible that it could be achieved with the $Mo_6S_{4.5}I_{4.5}$ or the $Mo_6S_3I_6$ nanowires with further work. More importantly, further work is required on the $Mo_6S_3I_6$ composites to produce significantly conducting composites. There are several possibilities, such as using a different polymer, but the reason for the difficulties with the $Mo_6S_3I_6$ nanowires compared to the $Mo_6S_{4.5}I_{4.5}$ nanowires needs to be understood also, as this is important to gain a greater understanding these material's behaviour. Reasonably high conductivities should be possible with some further work. It is possible that taking the extra step of completely purifying the nanowires before preparing composites would lead to improvements. The conductivities of the annealed $Mo_6S_3I_6$ measured here could be improved for the purified material, which would also allow composites with the purified material attain higher conductivities.

Appendix A – Publication List

"High Conductivity Observed at Very Low Volume Fractions of Carbon Nanotubes
in First Contact Polymer",

Denis N. McCarthy, Yenny R. Hernandez, James P. Hamilton

and Jonathan N. Coleman,

To be submitted

"Toughening of Artificial Silk by Incorporation of Carbon Nanotubes"

David Blond, **Denis N. McCarthy**, Werner J. Blau, Jonathan N. Coleman,

Accepted by Biomacromolecules

"Exfoliation of $Mo_6S_xI_{9-x}$ nanowires in common solvents",

Valeria Nicolosi, **Denis N. McCarthy**, Damjan Vengust, Dragan Mihailovic, Werner

J. Blau and Jonathan N. Coleman,

The European Physical Journal - Applied Physics, Volume 37, January 2007, Pages 149-159

"Dispersion and purification of $Mo_6S_3I_6$ nanowires in organic solvents",

Denis N. McCarthy, Valeria Nicolosi, Damjan Vengust, Dragan Mihailovic,

Giuseppe Compagnini, Werner J Blau and Jonathan N. Coleman,

Journal of Applied Physics, Volume 101, January 2007, Pages 014317

"Optical Observation of extremely low percolation threshold in $Mo_6S_{4.5}I_{4.5}$

nanowire/polymer composites",

Robert Murphy, Valeria Nicolosi, Yenny Hernandez, **Denis N. McCarthy**, David

Rickard, Daniel Vrbanic, Ales Mrzel, Dragan Mihailovic, Werner J. Blau and Jonathan N.

Coleman,

Scripta Materialia, Volume 54, Issue 3, February 2006, Pages 417-420

"Biomolecules as selective dispersants for carbon nanotubes",

Simon E. Moulton, Andrew I. Minett, Robert Murphy, Kevin P. Ryan,

Denis McCarthy, Jonathan N. Coleman, Werner J. Blau and Gordon G. Wallace,

Carbon, Volume 43, Issue 9, August 2005, Pages 1879-1884